Progress toward precision measurements using polyatomic molecules

Thesis by
Yi Zeng

In Partial Fulfillment of the Requirements for the
Degree of
Doctor of Philosophy

CALIFORNIA INSTITUTE OF TECHNOLOGY
Pasadena, California

2024
Defended April 15, 2024

Yi Zeng
ORCID: 0000-0003-0549-6060

ACKNOWLEDGEMENTS

I would like to express my sincere gratitude towards my PhD advisor Nick Hutzler, for teaching me many things in and out of the lab and being consistently kind and supportive throughout my time at Caltech; my undergrad advisor David Weld, for introducing me to AMO experiments; labmate Arian Jadbabaie, for being a great friend and mentor; postdoc Chi Zhang, for giving me new ideas and perspectives; and all my colleagues and friends, for helping me in countless ways and having fun together with me. I would also like to thank my parents, Xiaoping Zeng and Xianxiao Guo, for their unwavering support throughout my life.

ABSTRACT

Symmetry is a useful tool for solving problems and is a guide helping us to formulate new theories to better understand the universe. The violation of expected symmetries indicates a lack of full understanding and may point towards promising directions of inquiries. The combined Charge Parity (CP) symmetry is one such expected symmetry, and it's violated by a very minute amount in both theory and observations. Within the Standard Model, we don't know why it's here and we don't know its exact amount, though it is not enough to explain the observed asymmetry between matter and antimatter. Hence, studying CP-violating (CPV) physics is a great way to not only complete the Standard Model but also to find out new physics beyond it. We aim to measure CPV phenomena in polyatomic molecules. Specifically, we are going to measure the electron electric dipole moment and the nuclear magnetic quadrupole moment at a precision higher than ever before. Here I report the progress and developments we made towards achieving both.

PUBLISHED CONTENT AND CONTRIBUTIONS

[1] A. Jadbabaie, Y. Takahashi, N. H. Pilgram, C. J. Conn, Y. Zeng, C. Zhang, and N. R. Hutzler, "Characterizing the fundamental bending vibration of a linear polyatomic molecule for symmetry violation searches", New Journal of Physics **25**, 073014 (2023) 10.1088/1367-2630/ace471,
Y. Z. participated in the conception of the project, constructed some parts of the experiments, participated in data taking, and provided feedback in the writing of the manuscript. Publisher, IOP Publishing, permits the use of material in the thesis.

[2] Y. Zeng and N. R. Hutzler, "Nonresonant cavity for multipass laser intensity buildup", Appl. Opt. **62**, 3574–3580 (2023) 10.1364/AO.487531,
Y. Z. participated in the conception of the project, constructed the experiments, did the data taking and analysis, developed models and performed fits, wrote the manuscript, and responded to editors. Most of the paper is adapted into Chapter 5. Publisher, Optica Publishing Group, permits the use of material in the thesis.

[3] Y. Zeng, A. Jadbabaie, A. N. Patel, P. Yu, T. C. Steimle, and N. R. Hutzler, "Optical cycling in polyatomic molecules with complex hyperfine structure", Phys. Rev. A **108**, 012813 (2023) 10.1103/PhysRevA.108.012813,
Y. Z. participated in the conception of the project, constructed a significant portion of the experiments, did the data taking and analysis, developed models and performed fits, wrote the manuscript, and responded to editors. Most of the paper is adapted into Chapter 4. Publisher, American Physical Society, permits the use of material in the thesis.

TABLE OF CONTENTS

LIST OF ILLUSTRATIONS

LIST OF TABLES

Chapter 1

INTRODUCTION

1.1 Motivation

In the pursuit of understanding the universe, humanity has gone far. From the early days of learning from experiences to the scientific method of abstract logic deduction and experimental verification, we now can explain the happenings around us in quite a convincing fashion. Even under the scrutiny of a curious child, who incessantly asks 'why?', we can confidently explain the deep layers of causation, though maybe with the help of some written records that enhance the human memory, e.g. Google or Wikipedia. However, when the child inevitably asked the 'why' after we explained how the Standard Model or general relativity explains their previous question, we got stumped.

We don't know why there are three generations of subatomic particles in the Standard Model. We don't know why the Higgs takes on the mass it does. We don't know how to make the Standard Model compatible with general relativity. These problems are among the deepest and hardest we have ever faced, after the explosion of discoveries and new understandings for the past few generations. Of course, it will always be the case that the problems coming after the solved ones will be deeper and harder. I prefer now over any period of time in the past, because we understand the universe better, and have more advanced technologies to help us dig further into the fundamental workings of the universe. We might fail to answer all of these hard questions within our lifetime, but they are pursuits worthy of a lifetime.

Because the problems we face are as such, we likely no longer have the luxury of tackling them with one or two elegant theories or small experiments. Instead, we will have to prod and probe from all sides, to see the crack in the established theories, and narrow down the parameter space of the new, one step at a time. One well-known approach is observing the interactions between fundamental particles at ever-increasing energy scales, which increases the likelihood of observing new particles and processes. The Large Hadron Collider is a famous example of such an approach.

Alternatively, one can try to measure matter and interactions at a normal energy scale, but with extreme precision. We know from quantum field theory that ordinary

particles are surrounded by the seething quantum fluctuations that contain all the particles and forces blinking in and out of existence. For these particles and forces, the higher their energy scale, the shorter they live and the smaller perturbation they can cause to the ordinary matter. Therefore, the closer we can look at an ordinary particle, the more exotic new particles and forces we can observe.

In this thesis, I will discuss our work following the latter approach. Specifically, we want to measure the tiny perturbations in ordinary electrons and nucleons caused by charge-parity symmetry violating (CPV) processes, which I will discuss further in the following sections. Within precision measurement, there are still countless avenues we can choose. The main reason we want to focus on CPV related phenomena is that many beyond Standard Model theories introduce extra CPV compared to the Standard Model prediction, and they have the potential to explain many unsolved mysteries including the baron asymmetry of the universe, dark matter, hierarchy problems, and fine-tuning problems. In addition, CPV is not well understood quantitatively or qualitatively within the Standard Model[6, 7], so our measurements can potentially help refine the Standard Model.

1.2 Fundamental symmetries and violations

Human has an innate drive towards symmetry, for good reasons. Symmetry helps solve problems. One of my early fond memories of learning physics is solving complicated classical mechanics problems simply with the conservation of energy and momentum. It feels almost like cheating or having a superpower when compared to the cumbersome method of drawing force arrows and balancing forces and torques, especially when some of them would have 5 pulleys, 6 angled ramps, and 7 frictionless spherical cows. Many of these handy conservation laws come from continuous symmetries, according to Noether's Theorem.

Symmetries can also be used as an intuitive way to construct our understanding of the universe. A main aspect of the Standard Model is the gauge theory. By imposing local gauge invariance, boson field, and their corresponding interactions automatically pop out. For example, the existence and interactions of electromagnetism appear when we try to modify the Schrodinger equation to be invariant under the local gauge transformation of the form[8]:

$$\Psi(\vec{x},t) \rightarrow \Psi'(\vec{x},t) = e^{-i\chi(\vec{x},t)}\Psi(\vec{x},t), \tag{1.1}$$

which is a generic transformation that adds a location-dependent phase to the wavefunction.

Regardless of the genericness, it still feels like quite an arbitrary thing to do, and for a long time, I had a mental block preventing me from fully comprehending it—that is, until I read Kane's particle physics book [8]. He talked about how we don't question where $F = ma$ comes from as students of physics but will get annoyed with many quantum physics formulations. Now, I understand that gauge symmetry is just something people tried and happened to work out, just like seemingly random auxiliary/helping lines we draw to help solve geometry problems. The reason we call them symmetries is that similar constructs can be made to understand the weak and strong forces, and combined with electromagnetic force, their underlying math is that of the symmetry groups of U(1), SU(2), and SU(3). Hence the success of the gauge theory not only lies with its ability to describe the physics but also in its use of universal and expandable concepts of symmetry.

Then there are the discrete symmetries of charge(C), parity(P), and time(T) inversions. These are symmetries that we intuitively relate to particle-antiparticle, left-right, and forward-backward mirroring. In more rigorous terms, symmetry is observed if all the physics remains constant under the corresponding transformation. The C transformation is changing all the particles to their corresponding anti-particles, changing the signs of all the charges. The P transformation changes the sign of all spatial coordinates. The T transformation changes the sign of the time coordinates. Naively, we would assume these to be natural symmetries of the universe, helpful for solving problems and building understanding, just like the previously mentioned continuous symmetries and gauge symmetries. In fact, we do use them quite often in dealing with atoms and molecules. Specifically, parity is very commonly used as a label for quantum states, and for identifying allowed transitions, as will be seen in later chapters.

However, starting in 1956, physicists realized and experimentally proved that none of these symmetries are exactly observed by the universe. It means, that our universe is different from the mirror universes where the spatial coordinates of everything are flipped, the signs of charges are all flipped, and the flow of time is flipped. These are very surprising to our intuitions, except maybe the last one. We learned early on in our physics education, that along the arrow of time, entropy always increases. However, that is a consequence of probability and statistics. Almost all the fundamental laws of physics will stay the same if the signs of time coordinates are flipped in the equations. For a more in-depth discussion, see the chapter on time-reversal symmetry in ref. [6].

As for parity and charge symmetry, we understand quite well why they are violated; in fact, in the Standard Model, weak force interactions are said to maximally violate C and P symmetry [8]. We expect the combined CP symmetry to hold, which intuitively makes the double-negatives-make-positive kind of sense, and, we can imagine that the mirror universe made out of antiparticles and inverted coordinates will have the same physics. However, that is not the case, CP symmetry is still not exactly observed. The violation of CP symmetry is very small, but we don't know why and we don't even know how much is it within the Standard Model.

For example, the most well-known part of the CPV in the Standard Model is the Cabibbo–Kobayashi–Maskawa, or CKM matrix describing quark mixing. It contains a CPV parameter in the form of a complex phase angle. We have measured it to be of order unity, with uncertainty on the level of 10%. That is a fairly large value. However, the CPV observable arose from it is very small. A lepton analog exists in the form of the PMNS matrix that describes neutrino mixing. Due to the weak interacting nature of neutrinos, the CPV parameter in the PMNS matrix is much less well-measured and less understood.

A more detailed discussion of this lack of understanding will be in the next chapter. What's perhaps more intriguing is that discrepancies in the amount of CPV between theory and observation point toward new physics beyond the Standard Model. One famous example is the baryon asymmetry of the universe or the matter-antimatter asymmetry problem. From cosmological observations, we know that our universe is made exclusively from matter instead of antimatter. Since matter and antimatter will annihilate each other to create photons, we measure the imbalance between matter-antimatter to be the ratio between matter and photons in the current universe. Based on observations such as the cosmic microwave background, the ratio is measured to be around 10^{-10}, which is much bigger than the expected value of 10^{-26}, calculated from the Standard Model[9, 10]. Hence, there is intense interest in studying CPV physics, not only to better understand the Standard Model but also to look for new physics beyond it.

Currently, the only symmetry out of C, P, and T, that holds exactly is the simultaneous inversion of all three CPT. That is, inverting all three of these, will result in a universe that works exactly like ours, according to the CPT theorem, and it must be true for the Standard Model to work, as we understand it. Therefore, another way of studying CP violation is to study the violation of time inversion symmetry. In this thesis, I will use CPV and T-symmetry-violation interchangeably. Technically, the quantities

we are trying to measure here violate T symmetry, though we tend to use CPV more, for simplicity, convention, and the deeper physics motivations.

1.3 Electron electric dipole moment

The first thing we want to measure is the electron electric dipole moment (eEDM). It is easy to see why the electron having permanent EDM would violate time symmetry. Let's assume that the eEDM is aligned with the intrinsic spin of the electron in our universe. Then in the universe with time flowing backward, the electron will spin in the opposite direction, while the EDM, which is related to static charge distributions, remains the same. As a result, the electron EDM and spin will be anti-aligned in that universe, clearly distinguished from our universe[11]. A more rigorous description is that the electric dipole is P-odd, T-even while the spin is P-even, T-odd. As a result, an EDM together with a spin violates both P and T.

Such an argument will work the same if we assume the opposite: electron EDM and spin being anti-aligned in our universe. We know that these two aligning and anti-aligning are the only valid assumptions to make because we will have to introduce an extra quantum number otherwise, which is not compatible with known physics and chemistry. Due to the Pauli exclusion principle, no electron can have the same quantum numbers; that's why in atoms each orbital can only accommodate two electrons—one spin up and one spin down. Introducing an extra quantum number will increase the number of electrons in each orbital, which is not observed in nature.

Based on our understanding of the Standard Model, even though somewhat incomplete, we know that the electron almost certainly has EDM, though it is predicted to be exceedingly small, far beyond our current capabilities to measure it. In terms of high-energy physics experiments, we will have to upgrade our existing colliders' energy scale by several orders of magnitude. As mentioned in the previous chapter, CPV is not well understood even within the Standard Model. As a result, during the course of my graduate study, the calculated eEDM [1] risen from the CPV physics in the Standard Model has been modified upwards and currently stands at $1.0 \times 10^{-35} e$ cm[7]. Compared to the previous calculation of $1.0 \times 10^{-38} e$ cm [12], that is a 3-orders-of-magnitude change in the prediction.

Such a dramatic change in prediction won't be as surprising if one takes into account that we understand very little about the CPV sources in the Standard Model. The

[1] Rigorously speaking, what's predicted is the effective eEDM, where CPV interactions between electrons and nucleons were taken into account.

main sources of CPV are the CKM matrix, the PMNS matrix, and the θ angle. The first two matrices come from the weak interactions, mixing quarks and neutrinos respectively. They can be parameterized to have one CP-violating phase each. While we don't quite know why they exist, we are able to measure them. In the case of the PMNS matrix, the most up-to-date measurement still leaves the CPV parameter with a $\sim 30\%$ uncertainty [13], because neutrinos who only interact via weak force are notoriously hard to measure. Similarly, the CKM matrix is also a result of the weak force, and its values are also not precisely known, though a bit better than the neutrino ones. The value of The $\bar{\theta}$ angle is a parameter of the CPV term in the strong force, which can take on any value between zero and 2π. However, current experiments like neutron EDM measurements have constrained its value to be extremely close to zero, $\bar{\theta} < 10^{-10}$ from neutron EDM measurement [14], leading to a fine-tuning problem called the strong CP problem.

It is easy to see why measuring EDMs is crucial in advancing our understanding of CPV physics, both in and beyond the Standard Model. There have been quite a large number of experiments trying to measure it at higher and higher precision. Just like the calculation of it, there have been multiple new developments throughout my graduate study. The first is the ACME collaboration setting a new limit on eEDM with ThO molecule beam measurement in 2018 [15]. The second is a measurement done with the trapped molecular ion of HfF+ at JILA in 2022 [16], which is, at the time of writing, the most precise measurement that places an upper bound of $4.1 \times 10^{-30} e$ cm on eEDM. Compared to the theory calculation, the gap is now "only" 5 orders of magnitude.

To put that into perspective, the eEDM measurements have been improved by 3 orders of magnitude in the past two decades, largely thanks to the innovative developments of new platforms like diatomic molecule beams and diatomic molecular ion traps. Taking into account the possibility of further refining Standard Model calculations, and larger eEDMs resulting from new physics, it won't be surprising if we are going to see non-zero measurements soon in the following few decades. Granted, further improving precision is going to be harder and harder. That is why we are excited about developing a new platform of trapped polyatomic molecules for eEDM measurements.

Another way of thinking about the current progress in eEDM measurements is how they put constraints on possible new physics. Many beyond Standard Model new physics would introduce CP-violating new forces or new particles, such as super-

symmetry models, baryogenesis theories, and two Higgs models. These new forces or particles would generically introduce a CP-violating phase when interacting with the electron on the one-loop level. The interaction Feynman diagram is analogous to that of the electron anomalous magnetic moment, and a simple estimation of the mass scale of the new physics can be done by comparing it to the one-loop calculation of electron anomalous magnetic moment [17]. Using such estimation, the current eEDM limit sets a constraint on the mass scale of the new physics to $M \gtrsim (g/\alpha^{1/2})40$ TeV, where g is the effective coupling strength of the new particle to the electron, and $\alpha \approx 1/137$ is the fine structure constant [16]. Under the assumption that the coupling is of the same order of magnitude $g/\alpha^{1/2} \sim 1$, and the CP phase factor of the coupling is of order unity, we can say that the current eEDM experiments are probing new physics on the mass scale of $\sim$ 10 TeV, which is an order of magnitude higher than that of the Large Hadron Collider.

1.4 Nuclear magnetic quadrupole moment

Another T-violating phenomenon we want to measure is the nuclear magnetic quadrupole moment (nMQM). Just like EDM, any elementary particle possessing an MQM will break T symmetry, but unlike EDM, electrons can't have MQM, because it's a tensor quantity and can only exist in angular momentum $J \geq 1$ systems, which requires working with nuclei having nuclear spin $I \geq 1$. The observable of nMQM in molecules can be expressed as $\propto S\hat{T}\hat{n}$, where S is the valence electron spin, $\hat{T}$ is the rank 2 tensor relating MQM shift to the nuclear spin orientation, and $\hat{n}$ is the internuclear axis direction [18]. The S is the only T-odd quantity, while all the others are T-even. As a result, the nMQM is T-odd.

Similar to EDM, we can have a simple picture to intuitively understand why it violates T symmetry. nMQM can be understood as an EDM orbiting the nuclear spin (see Figure 1.1). As we go into the T-reversed universe, the nuclear spin, just like the electron spin will reverse direction. The EDM will also reverse direction as we have argued in the previous chapter, being a T-odd quantity. However, the orbit of the EDM will also go in the other direction when the time is reversed. As a result of these two reversals canceling out each other, the MQM will stay in the same direction. Hence, in the T-reversed universe, the nuclear spin direction relative to the MQM direction is opposite to the relative direction in our universe, which means that the physics is different between the two universes, and T-symmetry is violated.

While both eEDM and nMQM violate T-symmetry, they largely arise out of different

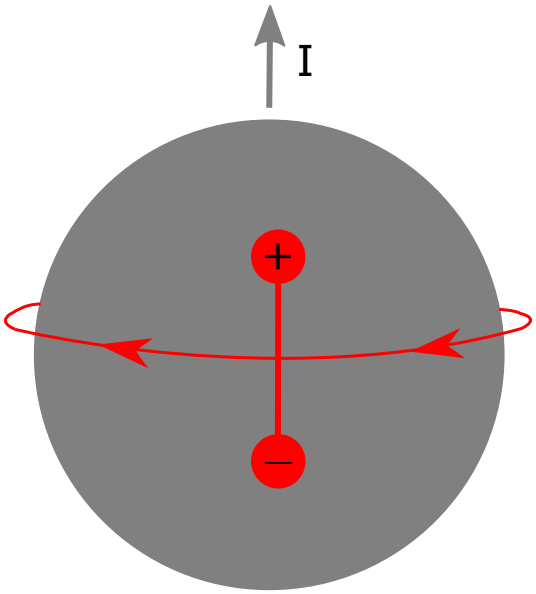

Figure 1.1: An intuitive picture of the nMQM, where I is the nuclear spin.

physics. The nMQM can be caused by orbiting nucleons having EDM, just like the intuitive picture in the previous paragraph. In a spherical nucleus, the valance electron is a main contributor; However, in a quadrupole-deformed nucleus more nucleons will be able to contribute, so deformed nuclei are much preferred for the purpose of measuring nMQM [19, 20]. Aside from the nucleon EDM, nMQM can also arise from P,T-odd internuclear forces and interactions. They come from various underlying CPV processes in the Standard Model, including the QCD CP-violation (the θ angle) and flavor-changing weak interactions described by the CKM matrix. Perhaps more exciting, are the contributions from beyond Standard Model CPV hadronic physics, which, depending on the models, can be orders of magnitudes larger than the contributions from the Standard Model nucleon EDM and P,T-odd nucleon-nucleon interactions [19].

While eEDM will also have some QCD contributions, largely due to the quarks and gluons in the quantum fluctuations surrounding the electron, the nMQM is a much more direct manifestation of hadronic CPV physics. In experiments using atoms and molecules, the nMQM will interact with the valence electron magnetically, resulting in induced eEDM. Fortunately, the magnitude of that will be proportional to the nuclear spin projection, so its effect can be distinguished from the actual eEDM. nMQM will be a great compliment search not only in terms of the underlying physics, but also in terms of the observable that is the same as eEDM, but easily differentiable[21].

In a CPV-sensitive molecule with a nuclear spin larger than 1/2, we are expected to see three T-odd observables: eEDM, nMQM, and nuclear Schiff moment (NSM). Without going into too much detail, the NSM is the unshielded component of the nucleon EDM. Any electronic moment of the nucleus will be naturally shielded by the electrons but NSM becomes observable due to the relativistic effect of the valence electron and the mismatch of the charge distribution and EDM distribution of the nucleus, an effect greatly enhanced in deformed nuclei [22, 23]. In general, it is harder to interpret than the nMQM, which is not shielded because of its magnetic nature [19]. All three observables have coupling parameters that describe the sensitivities of the molecule to them. These parameters are calculated using ab initio or semi-empirical methods. Therefore, it is crucial to test the reliability of these methods before we can reliably interpret any results [18].

Compared to the eEDM, the interest in nMQM is relatively new and there are not a lot of previous results. Currently, the limit is set by, interestingly, an eEDM experiment on Cs, in 1989 [24]. That limit is not often discussed as there are more modern and precise experiments to measure the nuclear Schiff moment, which arises from similar underlying physics sources as the nMQM [21]. Currently, the best constraint for new physics in the hadronic sector is set by the nuclear Schiff moment set by eEDM measurements done with Hg atoms [25]. Adapting modern molecular CPV search methods to MQM-sensitive molecules is a challenge, but will result in orders-of-magnitude improvements in sensitivity to hadronic CPV physics.

Chapter 2

MOLECULES

2.1 Why polyatomic molecules

As discussed in the previous chapter about eEDM, the recent decade of progress in eEDM measurements is dominated by new platforms of molecules. There is a simple explanation for why that's the case: molecules provide several orders of magnitude enhancement to the eEDM sensitivity via easy-to-align internal E-fields.

To elaborate, the experimental observable of eEDM is an energy shift proportional to the effective E field the electron experiences. Let d_e be the electron EDM, H_{EDM} be the Hamiltonian term or the energy shift of the eEDM, and E_{eff} be the effective E field. We have $H_{EDM} = -d_e \cdot E_{eff}$, by the definition of E_{eff}, which depends on the details of the electronic structure of the atom or molecule. It will require extra considerations if we are trying to measure it inside atoms or molecules. Intuitively, we expect the electrons in atoms to experience zero E-field on average. Even when a strong external E field is applied, we would expect the charge to redistribute and end up in an equilibrium where the electron experiences no net E field. That is similar to the nuclear Schiff moment mentioned in the previous chapter. According to Schiff's theorem, in non-relativistic quantum mechanics, there can be no first-order Stark shift proportional to the electric dipole moment of either the electron or the nucleon. However, as electrons travel through the nuclei, they experience relativistic speed; thus, we can evade the screening by noticing that, while the E field averages out to zero $\langle \vec{E} \rangle = 0$, the interaction $\langle \vec{d_e} \cdot \vec{E} \rangle \neq 0$, because the dipole moment experiences Lorentz contractions [26]. In fact, we now know that for atoms with heavy nuclei, the effect of eEDM is actually relativistically enhanced by a factor of $\sim Z^3$, and nMQM is enhanced by a factor of $\sim Z^2$ [27].

For atoms, because they can never be fully polarized in any realistic lab E fields, the effective E field E_{eff} is proportional to the applied lab E field E_{lab}, so $H_{EDM} \propto E_{lab}$ [25]. Typically, the polarization achievable in atoms, with a realistic maximum lab E field of $\sim$ 100 kV/cm, is on the level of $\approx 10^{-3}$, far away from the full polarization of 1 [11]. It is not the case for molecules, as some molecules can be easily fully polarized and provide the full strength of the internal E-field, which is much larger than the E_{eff} achievable in atoms. In other words, molecules can realize the full

relativistic enhancement of eEDM. Also, when molecules are fully polarized, they are effectively fully aligned with the applied E field, so fluctuations in E_{lab} won't directly translate to fluctuations in E_{eff} and thus the CPV observable H_{EDM}. In comparison, the uncertainty for eEDM measurements in atoms is $\Delta H_{EDM} \propto \Delta E_{lab}$, and the applied E field, especially a strong one, is extremely difficult to set up to be precise and stable. Thus molecule experiments suppress some of the strongest systematic uncertainties. It is not surprising that we have seen a full pivot of the CPV precision measurement field toward molecular platforms in the recent decade.

Currently, the leading edge experiments are the ACME ThO molecule beam experiment and the JILA HfF^+ trapped molecular ion experiment [15, 16]. Compared to atoms, molecules in general are considerably more complex in structure. One major challenge that we face in working with molecules is the inability to cycle photons, without significant additional efforts. Photon cycling is arguably the most crucial tool for manipulating atoms and molecules with lasers. A simple two-level system can continuously be excited by absorbing a photon and then drop back to the ground state by emitting a photon. Such photon cycling process is not only used in laser cooling, slowing, and trapping, but is also necessary for efficient detection, population pumping, and state preparation.

In molecules, there are additional vibrational and rotational states that can become potential dark states which will be further discussed in the next section. If a molecule falls into these dark states when it's cycling photons, it will no longer be addressed by the lasers. As an example, the ACME experiments used the ThO molecule for its high CPV enhancement and good polarizability. The electronic structure that enabled those things in ThO also makes cycling more than a few photons impractical.

Polyatomic molecules, on the other hand, open up the possibility of finding a species that offers similar enhancements and allows photon cycling. YbOH is one such promising molecule; it belongs to a class of molecules that has an unpaired valence electron, which we cycle photons on, localized away from chemical bonds such that the interactions with lasers will be less likely to perturb the vibration and rotation motion of the molecule [21].

Another significant feature for polyatomic molecules is the generic existence of parity doublets with energy splittings much smaller than any generic parity splittings, which are the rotational splittings in diatomic molecules. Parity doublets with small splitting are structures that enable polarization in small E fields. The existence of the E field breaks the parity symmetry of the free space and thus mixes the opposite

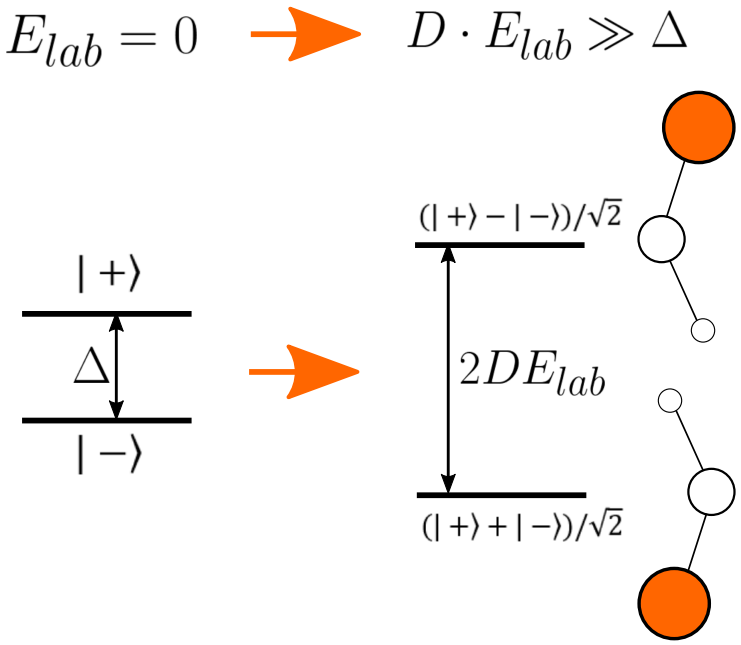

Figure 2.1: A simplified picture of polarization arising from parity doublets mixing in applied lab E field.

parity eigenstates. As shown in Figure 2.1, when fully polarized, the two mixed eigenstates become states that have definite dipole moments in the lab frame: one pointing along the E field and the other pointing opposite to the E field. In other words, when the molecule is in either of these states, it has a definite orientation in the lab frame, fixing the internal E field direction, which becomes the effective E field E_{eff} for our CPV observable H_{EDM}.

Polyatomic molecules will generically have structures providing parity doublets with small splittings, as a consequence of reduced symmetries. Specific to linear polyatomic molecules like YbOH, the generic feature that provides such doublets is the l doublets, which will discussed further in the next section. Fully polarized molecules not only give strong enhancement to CPV sensitivity but also give rise to a useful feature called internal co-magnetometer. With it, we can flip the sign of E_{eff} without needing to flip the sign of E_{lab}, which is a strong method of suppressing systematic errors related to the applied fields. Typically, an eEDM experiment will measure a quantity P that is the sum of two H_{EDM} with field-related systematic error E_F canceled:

$$P = H_{aligned} - H_{antialigned} = (H_{EDM} + E_F) - (-H_{EDM} + E_F) = 2H_{EDM}, \quad (2.1)$$

where $H_{aligned}$ and $H_{antialigned}$ are the energy shifts caused by eEDM being aligned

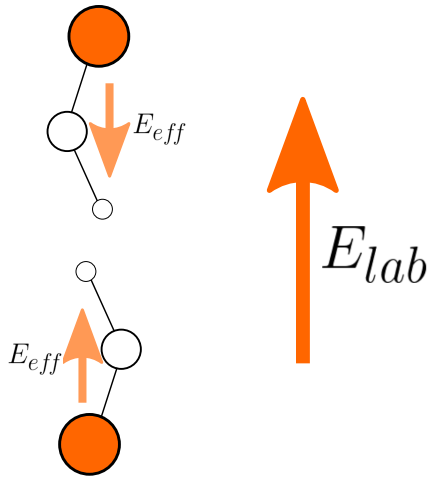

Figure 2.2: Continuing from Figure 2.1, the polarized states offer a way to change the effective E field without the need to change the applied lab field.

and antialigned with the internal E field of the molecule. It is effectively the same as flipping the external E field direction and measuring the energy shift difference, but it is practically impossible to precisely apply an E field of equal strength but of the opposite sign in the lab.

The fact that polyatomic molecules can have parity doublets even smaller than that of the diatomic molecules, and require a much smaller applied E field to be fully polarized, will further suppress systematic errors and simplify aspects of the measuring apparatus related to applying the fields. Of course, alongside the amazing advantages, polyatomic molecules also bring a higher degree of complexity, which will require extra effort to control, just like how the transition from atoms to diatomic molecules brought requirements of a higher degree of sophistication to the experiments. Fortunately, the field of manipulating molecules has progressed significantly in the past decade, and many technological advances have enabled the first demonstration of laser cooling and trapping of the first polyatomic molecule, CaOH [28]. I will discuss some of the challenges associated with polyatomic molecules, or molecules in general in the next section, and have more discussion, in the following chapter, about new developments that will enable precision measurements with polyatomic molecules in the near future.

2.2 Molecular structure

Figuring out molecule structure can be boiled down to doing many-body physics. We can't solve problems involving more than two interacting bodies exactly, so we

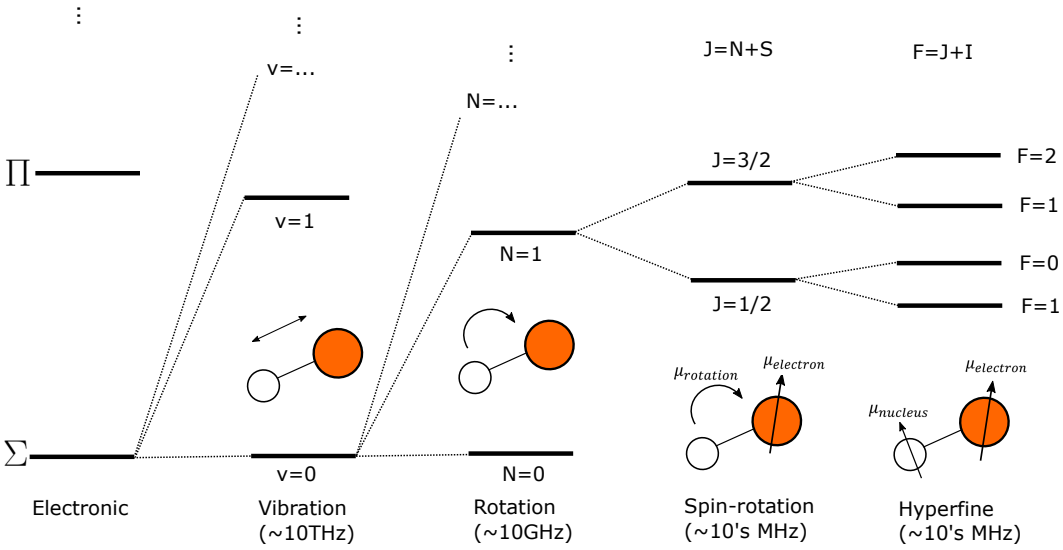

Figure 2.3: A basic molecule structure with Σ electronic ground state (no electron orbital angular momentum). Electronic states that aren't Σ will look very different.

have to come up with methods of approximation to both undertake calculations and form intuitive understandings. In order to understand molecules, we use angular momenta to describe the quantum states of the molecule and the coupling between these angular momenta helps us understand the interactions and selection rules. Also, we separate the molecule wavefunctions into separate ones corresponding to electronic structures, rotational structures, vibrational structures, etc, according to the Born-Oppenheimer approximation, and treat many interactions perturbatively. Here, I will mostly discuss features and results relevant to the following chapters, mostly in ways that I personally find intuitive to understand, instead of a full treatment of molecule structures with angular momentum algebra. For that, see [11, 29].

ELECTRONIC STRUCTURE: most of the concepts are familiar or exactly the same here as typical atomic physics. There are some slightly modified state labels to signify it's a molecule state and accommodate extra angular momentum quantum numbers. For example, we use s, p, d, etc to label the orbital angular momentum of the valance electron in atoms. In molecules, we instead use Σ, Π, Δ, etc for the projection of that momentum onto the internuclear axis. There are more physics related to chemical bonding and how atom electronic states are mapped before and after chemical bonding. These are beyond the scope of this thesis and will not be discussed in detail here. Ultimately, thanks to polyatomic molecules not relying on electronic parity doublets and the fact that molecules like YbOH have the valence electron localized around the metal nucleus, their electronic states can be largely

treated similarly as atoms' and we don't have to elaborate on the chemical bonding.

Here, we will mainly consider the electronic state label, typically in the form of

$$X\ ^{2S+1}\Lambda_{\Omega}^{(+/-)} \tag{2.2}$$

for most of the molecule electronic states we deal with in this thesis. The X symbolizes the fact that this is the ground electronic state. The excited states are labeled by A, B, C, etc. instead, usually determined by the time sequence of when these states are discovered. Sometimes $\tilde{X}$ is used instead of X, to symbolize the fact that it's a polyatomic molecule state. The Λ is the projected orbital angular momentum labeled with Σ, Π, Δ, etc for angular momenta of 0, 1, 2, etc. The S is the valence electron spin. The Ω is the total electron angular momentum projection onto the internuclear axis $\Omega = \Lambda + \Sigma$, with Σ being the electron spin projection, though Ω is commonly omitted in practice. The $+/-$ label is only used for states with $\Lambda = 0$, and they symbolize the parity of the lowest rotation level in that state.

Such a labeling scheme is generally suitable for most electronic states in linear molecules. The exception that is important for us is the label for molecules in states with bending mode angular momentum. We use such bending states for our precision measurements, and the scheme used for them is $^{2S+1}K_P^{(+/-)}$, with everything staying the same except $K = \Lambda + l$ and $P = \Lambda + \Sigma + l$. l is the bending mode angular momentum that will be further discussed in the vibration structure discussion.

VIBRATIONAL STRUCTURE: this is where polyatomic molecules introduce most of the new complexities compared to diatomic molecules. Just by adding one additional atom, we have to introduce three new quantum numbers to label the vibration state of the molecule. Previously with diatomic molecules, we only need one quantum number to denote the vibration mode of the two atoms stretching. The main thing of note for this stretch motion vibration mode is that, unlike rotational structures, there are no fundamental selection rules that can limit the transition dipole moments. As a result, a large amount of new dark states for molecules are states with higher vibration quantum numbers.

With linear triatomic molecules like YbOH, we conventionally use $(\nu_1 \nu_2^l \nu_3)$ to label the vibration modes, where ν_1 and ν_3 are the quantum numbers for the stretch modes between the two neighboring atoms, ν_2 denotes the quanta of bending motion, and l is the quantum number for the vibrational angular momentum that's projected onto the internuclear axis. See Figure 2.4. For $\nu_2 = 1$, the only possible value for l is 1,

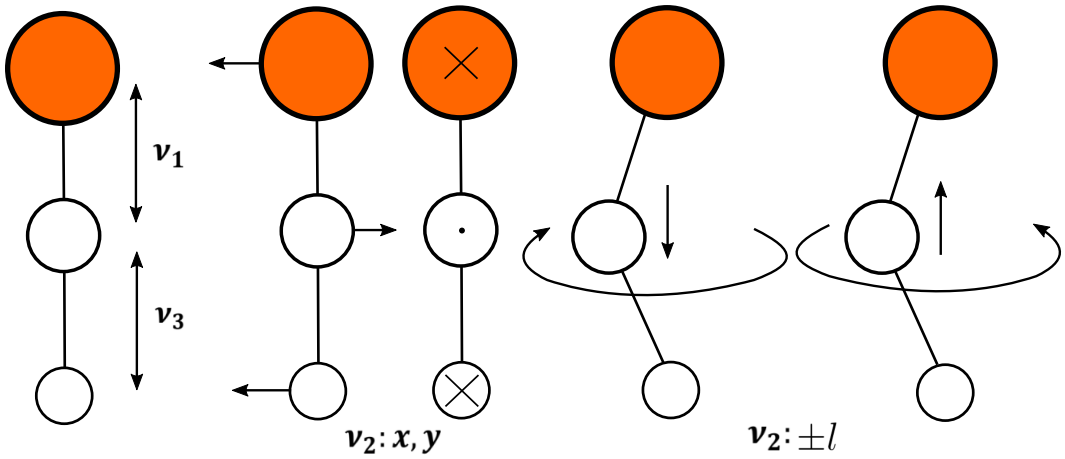

Figure 2.4: A schematic demonstrating how the vibration motion of a linear triatomic molecule is labeled. For the bending motion, there are two orthogonal components. They can be described as the orthogonal bending motions of left-right and in-out directions. Or in the case of v_2^l labeling, v_2 is the total bending vibration quanta and l is the bending rotation quanta.

so we often just omit it and use (0,1,0) to label the lowest excited state in bending mode.

While v_1 and v_3 are similar to the diatomic molecule stretch motion, it's the bending motion v_2^l that introduces a lot of new interactions as well as the all-important parity doublet with small splittings. In another way, bending motions can also be labeled by two quantum numbers for the two bending motional modes that are orthogonal to each other, which is probably more intuitive to imagine. Mathematically these two ways of labeling the bending modes can be transformed between each other. Intuitively, we can imagine the superposition of the two orthogonal bending motions can be re-imagined to be a bent linear molecule rotating around the internuclear axis, almost analogous to how linear and circular polarizations of light work. For the purpose of calculations and understanding interactions, we prefer using the v_2^l label since we care about the angular momentum l.

l is the source of the parity doublets with small splittings that linear polyatomic molecules generically have. We can see why the energy difference between a state with $+l$ and another with $-l$ would be much smaller, in terms of the moment of inertia. For example, compared to the end-to-end rotation, the rotation around the internuclear axis of a slightly bent linear molecule has a much smaller moment inertia, and thus the energy scale involved is much smaller.

As an angular momentum, l also introduces interactions with other angular momenta. Since we are going to use the bending mode of YbOH for measuring CPV physics, it is crucial to take these new interactions into account. For example, the interaction between electrons and the vibrational angular momentum will introduce extra energy shifts in the spin-orbit splitting, as well as cause extra vibronic coupling between states of different electronic and vibrational quantum numbers [30]. It can be handy since it couples some of the states that previously were forbidden transitions.

ROTATIONAL STRUCTURE: while polyatomic molecules can introduce more complexities, in the case of linear molecules like YbOH, we can treat their rotations exactly like diatomic molecules because of symmetry. We only consider the rotation around the axis that is perpendicular to the internuclear axis, the end-to-end rotation. The rotational structures are typically not too big of a problem for laser manipulation, aside from introducing a new angular momentum, since we can often prevent rotational dark states by using selection rules. We commonly use N as the label of the rotational quantum number of a state. However, in different labeling schemes called Hunds' cases, we sometimes only use the label J for the combined angular momentum of rotation and electron orbit. All these are just approximations, but we choose different Hund's cases for a more intuitive understanding of what's going on, and sometimes simplifying calculations. There are also cases where we use N to label the combined angular moment of the electron orbit, the end-to-end rotation, and the vibrational angular moment.

While angular momentum coupling is something we are familiar with in the atoms, usually in the form of spin-orbit coupling, it is far more prevalent and messy in molecules. Molecules introduce more angular momenta that will interact with each other and a natural reference axis in the form of an internuclear axis. Therefore, it is helpful to introduce schemes to facilitate calculations and intuitive understanding. That is where the Hund's cases come in. Depending on the relative strength of the various angular momentum couplings, different angular momenta and their projections are used as good quantum numbers, such that when using them as the basis for effective Hamiltonian matrix calculation, the matrix elements will largely stay diagonal, making it easier to calculate and interpret the resulting eigenstates. Such calculation will be further discussed in the next section.

One important case for us is the Hund's case (a). It is for the case where the spin-orbit coupling is stronger than that of the rotation and the angular momenta like orbital angular momentum and electron spin are strongly coupled to the internuclear

axis. As a result, the projection of these angular momenta on the internuclear axis are good quantum numbers. For example, Σ for the spin S Projection, Λ for the orbital L projection, and Ω for the sum of the two.

The other important case for us is case (b). It is for the case where projections to the internuclear axis are also important, but the spin-orbit interaction is weak or non-existent. An example is the Σ electronic states where the orbital angular momentum is zero, $\Lambda = 0$. In case (b), the rotation angular momentum N is a good quantum number, unlike case (a).

We exclusively use the Hund's case (a) coupling scheme for calculations, even for the states that are more appropriately described by case (b). Hund's cases are just schemes for organizing angular momentum couplings. Ultimately they don't change the underlying physics or calculations. By using a single case for calculating everything, we simplify the basis set and matrix elements preparations with the sacrifice being interpretation difficulty. However, in practice, the interpretation is not hard in our cases.

FINE AND HYPERFINE STRUCTURE: there are some new features still worth mentioning. Firstly, there's a new term for spin rotation interaction, which is analogous to the spin-orbit coupling commonly seen in atoms and molecules as well. Secondly, there are extra hyperfine terms concerning nuclear spins outside the atom where the valence electron is from, and they can interact, usually very weakly, with the valence electron's spin, orbit, or other angular momentum. As an example, for YbOH, both the Hydrogen nucleus and the Yb nucleus carry nuclear spins and can interact with the valance electron spin. As a result, we typically require multiple labels, like F and F_1 for YbOH, where F is the typical total angular momentum, and F_1 is the total angular momentum excluding the hydrogen nuclear spin. Fortunately, in the case of polar molecules like YbOH, the valance electron is localized almost exclusively at the metallic core, far away from the bonding region and thus far away from other nuclear spins. As a result, the hyperfine splitting caused by the other nuclear spin is typically very small and won't cause meaningful differences in most cases. for example, the hydrogen nuclear spin hyperfine is not resolved in high-resolution spectroscopy of the ^{171}YbOH and ^{173}YbOH [18]. They do contribute to the extra "degeneracies" of the systems, so while we can treat their energy level to be the same, we have to keep in mind the actual number of sublevels thanks to the hydrogen nuclear spin.

All these complex structures, ranging from unresolved hyperfine to the $\sim$ 10THz

level large splittings caused by vibrations, make new approaches possible but also make life difficult for the experimentalists. We try our best to use clever labelings and classical analogies to paint an intuitive picture of the molecule structures. At the end of the day, we sometimes also just have to "shut up and calculate!".

2.3 Calculations: effective Hamiltonian

Continuing the theme of approximation, the method of calculation we use is called effective Hamiltonian [31]. Every mathematical description of the world can be boiled down to equations with some amount of parameters that we can fit using measurements from experiments. Ideally, we would like to have a set of equations with only a small amount of parameters that are the fundamental constants of the universe, and we can conduct ab initio calculations to describe how a complex system like a molecule will behave. Unfortunately, that is not the case.

What we have currently, is a model where we need to have a handful of free parameters for each electronic state of each molecule, and depending on the level of approximation needed, more and more parameters are needed for a good fit. Nevertheless, the model we have is quite a clever one, with strong predictive power and a good ability to paint an intuitive picture of the underlying physics. However, it is important to keep in mind that while all the terms and parameters have specific and descriptive names, they are still approximations, good ones, but sweeping some details under the rug. That is why it's called the effective Hamiltonian.

The general procedure is we first come up with a basis set of states with all the relevant quantum numbers. Then, for each electronic state, we put together all the effective Hamiltonian terms describing all the needed coupling and splittings together in the form of matrix elements in the chosen basis. By diagonalizing the matrix for each electronic manifold, we will get the resulting eigenvalues as the energy levels, and the resulting eigenvectors as the eigenstates correspond to the energy levels. If we want to calculate the transition dipole moment and branching ratio between different eigenstates, we can then use the dipole operator to connect the derived eigenstates and calculate the amplitudes.

In theory, the basis set can be in any arbitrary orthonormal basis that covers the needed Hilbert space, but usually, we want to start out with something that already makes intuitive sense and can simplify the matrix diagonalization process. That's why it's convenient to use the Hund's cases. Different Hund's cases prescribe different sets of good quantum numbers, coming from different underlying schemes for

coupling angular momentums in sequences. While we can try to use the best Hund's cases for different electronic states and different molecules to improve calculation efficiency, we ultimately decided that it's simpler and easier to communicate within the lab, to always use Hund's case (a) for basis sets to start a calculation, which uses the quantum number $\Lambda, l, \Sigma, \Omega, J, F, M_F$, where J is the total angular moment excluding hyperfine, F is the total angular momentum, Λ, Σ are the electron orbital angular momentum and electron spin projected onto the internuclear axis, $\Omega = \Lambda + \Sigma$, and M_F is F projected onto the lab z-axis.

Once the basis is determined, one just has to build a basis set big enough that it contains all the constituents of the relevant eigenstates. Depending on how off-diagonal the interactions being considered can couple, typically, having the max J number (corresponding to the number of rotation states to include) of the basis set to be 2 or 3 larger than the eigenstates of interest will be enough. As an example to illustrate the process, we can consider the basis set for the A state of ^{174}YbOH, which has $S = 1/2, L = 1, I = 0$, ignoring the hydrogen hyperfine. The basis set for $J \leq 5/2$ in Hund's case (a) would have 6 basis vectors, if we don't include the total angular momentum projected onto the lab z-axis, M_J. Since we are not going to include any Hamiltonian terms involving external fields in the example, the quantum number M_J won't be used in any matrix elements. An intuitive reason for that is that, without an external field acting as a reference, angular momentum projection in the lab frame is not defined. In the form of $|n\rangle = |\Lambda, \Sigma, \Omega, J\rangle$, these basis vectors are:

$$|1\rangle = |-1, 1/2, -1/2, 1/2\rangle \tag{2.3}$$

$$|2\rangle = |-1, 1/2, -1/2, 3/2\rangle \tag{2.4}$$

$$|3\rangle = |-1, 1/2, -1/2, 5/2\rangle \tag{2.5}$$

$$|4\rangle = |1, -1/2, 1/2, 1/2\rangle \tag{2.6}$$

$$|5\rangle = |1, -1/2, 1/2, 3/2\rangle \tag{2.7}$$

$$|6\rangle = |1, -1/2, 1/2, 5/2\rangle \tag{2.8}$$

Then it's the difficult step of finding the right matrix elements for all the desired Hamiltonian terms and converting them to the Hund's case (a) basis when needed. For our molecule, the typical sets of Hamiltonian terms are rotation, spin-orbit, spin-rotation, Λ doubling, hyperfine terms, and the Zeeman effect. For more details on each term see ref. [29, 31]. For our simplified example of A state ^{174}YbOH with 6 vectors basis set, we will only include Hamiltonian terms for rotation, spin-orbit,

and Λ doubling:

$$H = H_{rotation} + H_{SO} + H_{\Lambda doubling} \tag{2.9}$$

Each of these terms consists of a parameter specific to the molecule and electronic state and some function of the quantum number in the basis vectors. For example,

$$\langle n| H_{SO} |n'\rangle = A(\Lambda \cdot \Sigma)\delta(n, n'), \tag{2.10}$$

where A is the spin-orbit parameter, Λ and Σ are the quantum numbers of the basis vector $|n\rangle$, and δ is a set of Kronecker Delta functions enforcing selection rules, which is simply $\delta(n, n') = 1$ only when $n = n'$ for H_{SO}.

The simplicity of this term is due to the fact that we have chosen a basis where spin-orbit is large compared to other terms, and our basis vectors are chosen to be eigenstates of spin-orbit. Typically, quantum numbers from both bra and ket vectors are involved, and the selection rules are more selective. Such as the Λ doubling term, which is of the form $\langle n| H_{\Lambda doubling} |n'\rangle \propto \delta_{\Lambda,\Lambda'\pm 2}$. $H_{rotation}$ is another diagonal matrix element with $\delta(n, n')$, and it can be derived from the operator form of $B(J - L - S)^2$, with B being the rotation parameter. All matrix element formulas can be derived from such operator forms using angular momentum algebra, but for practical scenarios, they can typically be looked up. For both the formulas and derivations, see ref. [29, 31, 32]

Now with all the ingredients of basis sets and matrix elements prepared, we can construct the full matrix for each electronic state, and leave the calculation of matrix diagonalization to the computer. We typically deal with modest-sized matrices, and the couplings are mostly linear in nature, so it's not very computationally intensive. The end result will be a set of eigenvalues and eigenvectors, which, as mentioned before, are the energy levels and eigenstates of the molecule. Based on the distribution of eigenstates in terms of their energy levels and the constituents of these eigenstates, we can find a Hund's case that's the best fit for the electronic state, and assign quantum numbers to these eigenstates accordingly.

In our example, the Hamiltonian expressed in our 6 vector basis is a 6x6 matrix $\langle\Psi| H |\Psi\rangle$. Diagonalizing it will give the following eigenstates, ordered by their

eigenvalue:

$$|a\rangle = \frac{1}{\sqrt{2}}|1\rangle - \frac{1}{\sqrt{2}}|4\rangle = |1/2, -\rangle \tag{2.11}$$

$$|b\rangle = \frac{1}{\sqrt{2}}|1\rangle + \frac{1}{\sqrt{2}}|4\rangle = |1/2, +\rangle \tag{2.12}$$

$$|c\rangle = \frac{1}{\sqrt{2}}|2\rangle - \frac{1}{\sqrt{2}}|5\rangle = |3/2, -\rangle \tag{2.13}$$

$$|d\rangle = \frac{1}{\sqrt{2}}|2\rangle + \frac{1}{\sqrt{2}}|5\rangle = |3/2, +\rangle \tag{2.14}$$

$$|e\rangle = \frac{1}{\sqrt{2}}|3\rangle - \frac{1}{\sqrt{2}}|6\rangle = |5/2, -\rangle \tag{2.15}$$

$$|f\rangle = \frac{1}{\sqrt{2}}|3\rangle + \frac{1}{\sqrt{2}}|6\rangle = |5/2, +\rangle \tag{2.16}$$

The kets after the second equal sign are their new state labels $|J, \text{parity}\rangle$. These are the physical observable states. The mixing is a result of the Λ doubling term. Basis vectors with equal and opposite Λ quantum numbers are mixed into parity doublets. These eigenstates and their new labels are pretty much exactly the same as the actual A states in 174 YbOH, or even ^{171,173}YbOH, just missing some extra quantum number labels like F for hyperfine. It just shows how good Hund's case (a) is in describing the A state YbOH, and how much it can simplify calculations.

Once we have the eigenstates, we can calculate the transition dipole moments between different states by inserting dipole operators, expressed in Hund's case (a), between the two state vectors $\langle\Psi_1|\,\vec{d}\,|\Psi_2\rangle$. This is too complex to write down in general, but one can use the methods of angular momentum algebra to find the expressions for the relevant eigenstates [31]. Together with the energy levels, we now have the crucial observables we can use to either guide future spectroscopy measurements or use existing measurements to fit unknown parameters. In ref. [18, 30], we used this effective Hamiltonian and spectroscopy experiments to calculate many important parameters for YbOH, which are crucial for future experiments. Chapter 4 will present how we used these parameters and similar effective Hamiltonian to calculate the branching ratios that guided us to find a scheme to cycle photons on ^{171}YbOH and ^{173}YbOH. It also presents more specific details about the Hamiltonian terms used.

Chapter 3

EXPERIMENTAL METHODS AND DEVELOPMENTS

3.1 1 Kelvin cryogenic buffer gas beam source

As discussed in previous chapters, molecules have vastly more complex structures than atoms. Hence, we want our molecules cold not only for reasons similar to that of the atoms, like lowered Doppler width but also for reasons unique to molecules, like having more population concentrated in the vibrational and rotational ground states. The complex structures of molecules also make laser cooling and slowing on them very difficult. Therefore, ideally, we want to produce our molecules cold, slow, and in large amounts to begin with. I built a large part of such a molecule source.

By the time of writing this thesis, the Cryogenic Buffer Gas Beam (CBGB) source is now the standard workhorse of molecule or even some atom labs [33]. The main mechanism for how it works is quite intuitive to understand. The target species of atoms or molecules are introduced to a cell cooled down to cryogenic temperature and filled with some inert gas, they will thermalize and exit out the cell through an aperture, after which they can be studied or further manipulated, like being laser cooled or trapped. Typically, when the target species leaves the cell, its forward velocity is that of the thermal velocity of the buffer gas at a temperature similar to that of the cell, which is about 150 m/s for 4 Kelvin and 80 m/s for 1.5 Kelvin, and many of the internal degrees of freedom also cooled down to mostly concentrate in ground and low excited levels [29, 33]. Obviously, such initial states are highly desirable, especially for species that are hard to laser cool and slow.

There are two main methods by which the target species can be introduced. First is the ablation of solid targets with high energy pulse lasers inside the cell. The second is introducing target species in gaseous form via a heated fill line into the cell. These two methods can be combined as well. For example, we can introduce Yb by ablating a Yb metal target, an excellent ablator, and we can introduce OH ligands by using a heated fill line to pipe in gaseous water vapor or alcohol vapor.

Typically, the advantage of solid target ablation is its versatility. Most species that stay in solid form under vacuum can be used as the target, sometimes with the help of binders like polyethylene glycol (PEG) and laser absorbers like fine-grain

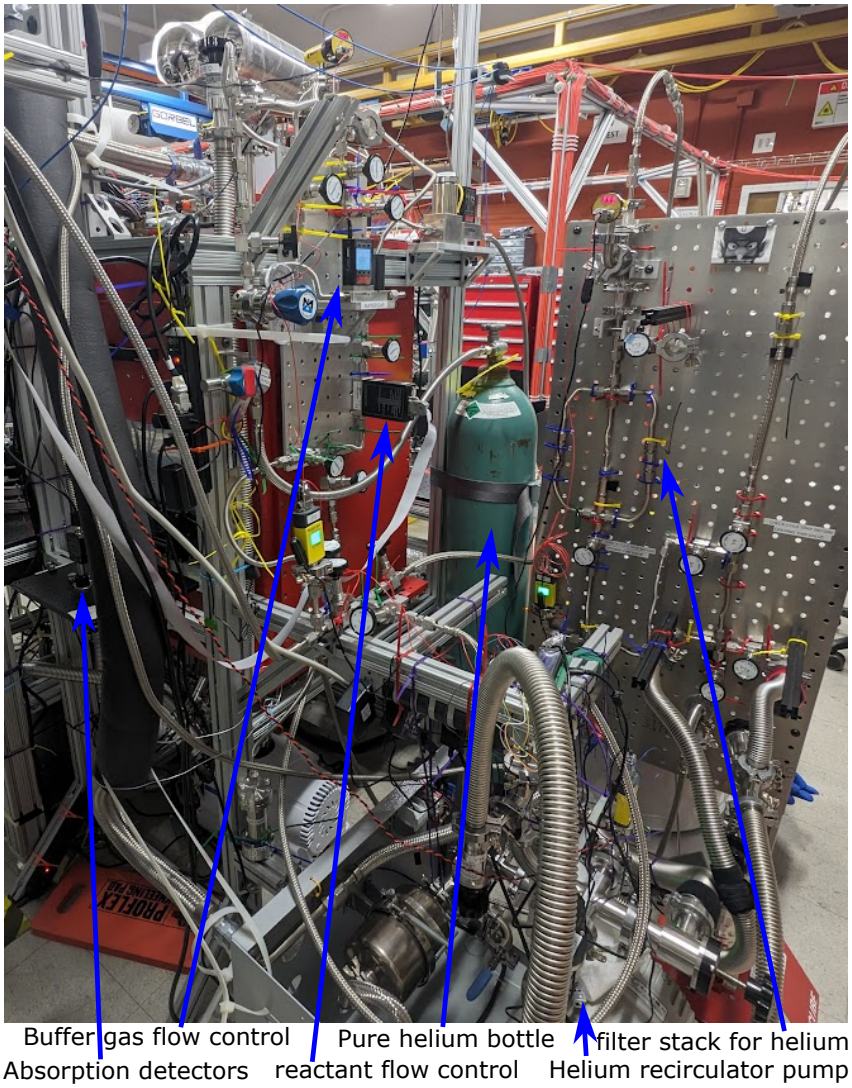

Figure 3.1: Photo of the back side of the 1 K CBGB source chamber. It shows most of the gas line structures for operating the CBGB source and the pumped helium 1 K system. A large vacuum chamber used as a dump volume for the 1 K system is under the table to the left and thus not in the photo. We use the helium from the pure helium bottle for both buffer gas and the 1 K system. The reactant flow control is currently not in use, and it used to be used for introducing methanol as reactant via a heated fill line to the cell.

Yb powder. When ablated by pulsed lasers, most components of the target will be released in the form of plasma, which will contain a veritable zoo of component species that will then form molecules and complexes.

The heated fill line is straightforward to understand, though tricky to implement, due to considerations like heat load and clogging. Most gas will freeze at our cryogenic temperatures, so we have to heat up the gas line leading up to the cell,

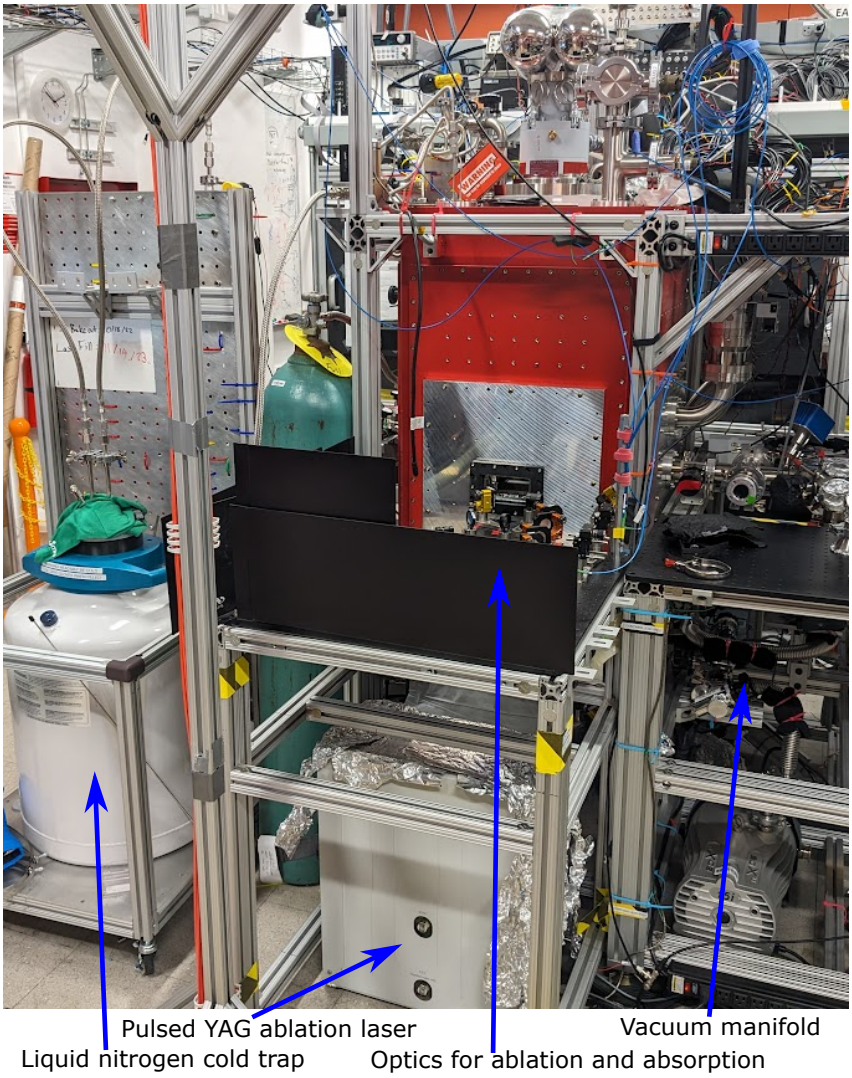

Figure 3.2: Photo of the front side of 1 K CBGB source chamber. The liquid nitrogen cold trap is used to freeze out contaminants in the 1 K system to prevent clogging. The pulsed YAG laser is used for ablating targets in the cell. The laser head is behind the control box underneath the optics table.

but too much heat will prevent the cell from cooling down to the target temperature. The interface between the heated fill line and the cell is especially tricky since it have to be somewhat leak-tight, but also thermally isolating. A common failure mode for the heated fill line is clogging due to gases freezing on the interface. In general, when correctly implemented, the advantage of the heated fill line is that it's more consistent compared to the target ablation method. Especially when the target species is not a great ablator, the yield difference between shot to shot can be quite large and hard to average out.

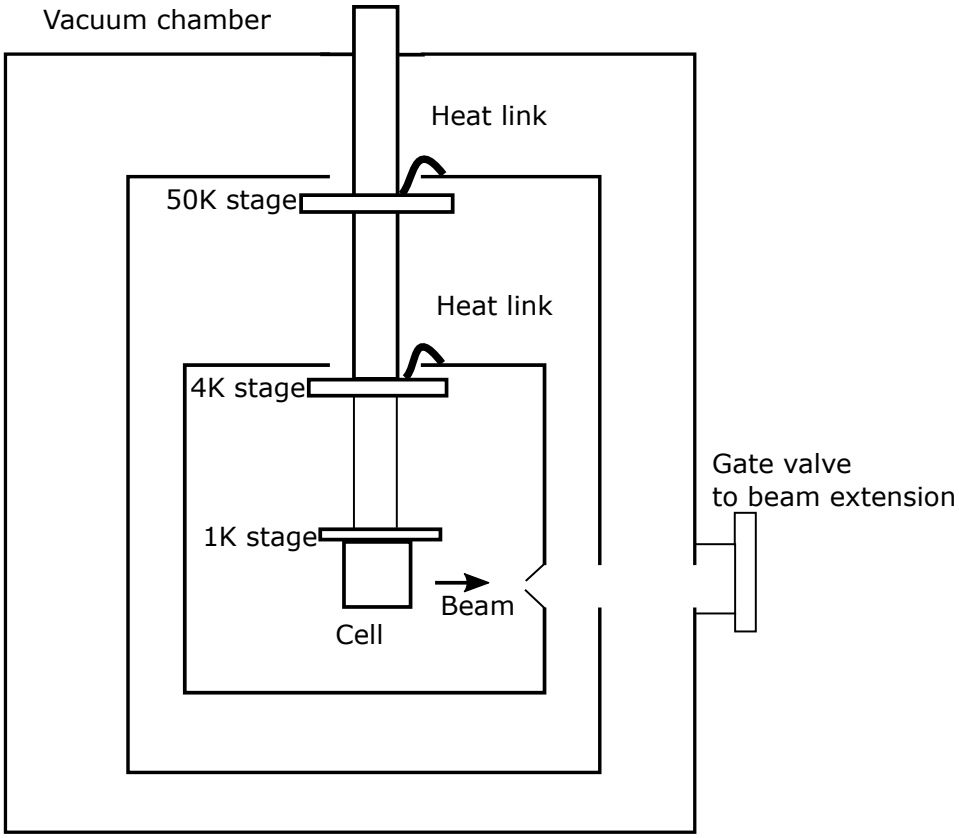

Figure 3.3: A simple schematic of the 1 K chamber.

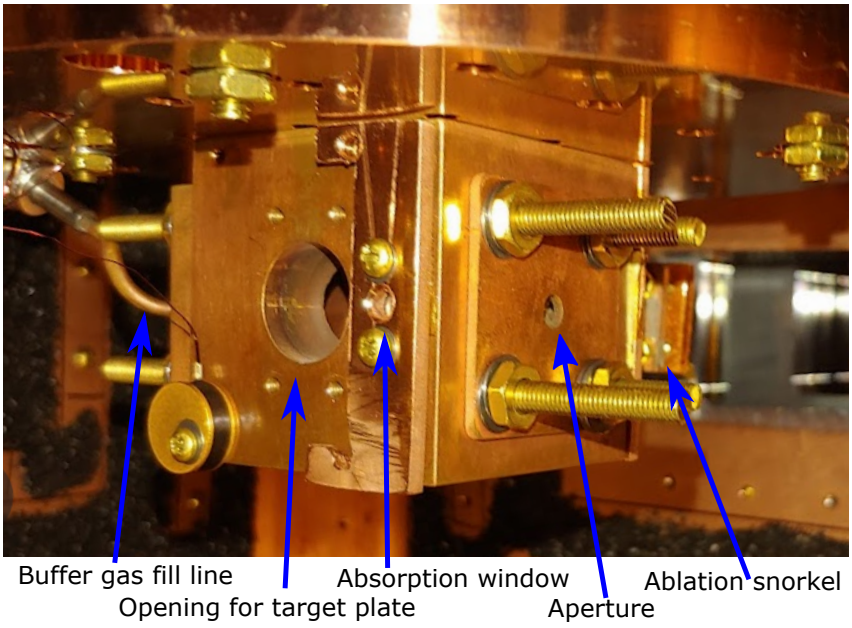

Figure 3.4: Photo of a typical CBGB cell, with important features labeled.

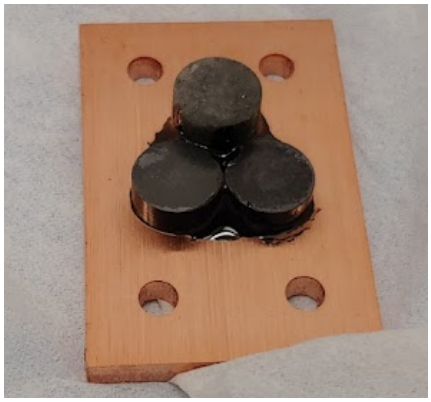

Figure 3.5: Example of a target plate with three fresh targets. These are targets with different ratios of $Yb(OH)_3$ and Yb Powders, glued on with Stycast. The black color of the target mostly came from the Yb Powder.

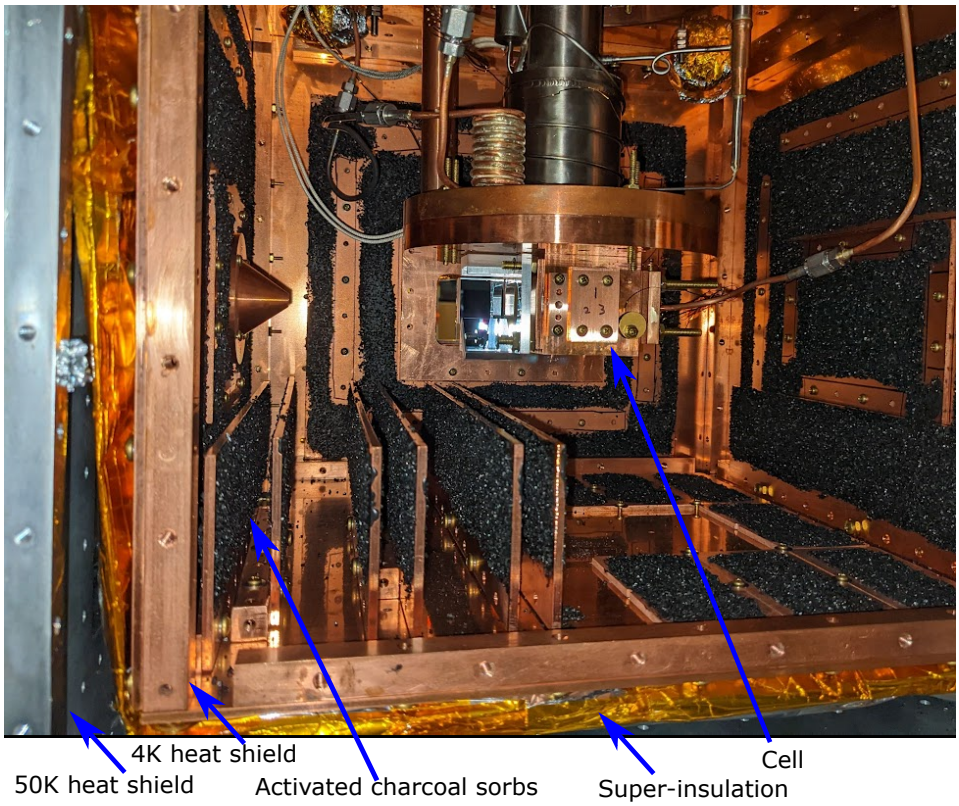

Figure 3.6: Photo of the surrounding structures around the cell. The super-insulation is multiple layers of thin aluminum-coated mylar, fastened together with Kapton tapes along the edges, hence the orange color on the edges instead of the shiny silver color.

The cell is designed to be modular, so it can be easily modified, tested, and optimized. Optimizing molecule production is an important part of our work, and is always

ongoing whenever there's an opportunity. After all, a small gain at the source could save much more effort downstream and improve many aspects of the experiments by increasing the number of molecules and slowing them down. All components are made from copper C101 for its superior thermal conductivity even at cryogenic temperatures (see Figure 3.4). The main body is a 2x2x2 inch cube with a main bore hole of 1.5 inches in diameter. One end of the borehole is where the buffer gas is introduced and the other end is covered with an aperture plate, where the molecule will exit.

There is a centered 1-inch diameter borehole orthogonal to the main borehole. One opening of that is used for a target plate, and the other opening is for a snorkel plate. The Snorkel plate is used for having the ablation window far away from the targets so that the dust plume from the target ablation will be less likely to reach it and make it opaque. There are smaller holes near the aperture, that are served as absorption windows, where absorption probe lasers and enhancement lasers can go through. All the different plates and windows are subject to change and optimization. We also can mount a smaller second-stage cell right after the aperture plate. It can slow the forward velocity of the molecules significantly, sacrificing the number density of the molecule in the resulting beam.

The surrounding structures around the cell have to provide two major functions. The first is heat load control, and the second is buffer gas pumping. A quick back-of-the-envelope calculation will show that the main thermal load will be black body radiation if the cell is directly exposed to the room-temperature vacuum chamber. The black body radiation from a 1 square meter surface at room temperature is about 400 W, while our fridge at the 4 K stage only have cooling power on the level of $\sim$ 1 W. We have to build multiple layers of heat shields to protect the cryogenic stage from thermal radiation, in concert with the pulse tube cooler which has multi-stage cold heads. For the 1 K system, there are three stages, 50 K, 4 K, and 1 K stage.

The higher temperature stages have higher cooling power, so we want to make sure there are heat shields staying at 50 K and 4 K to block the 300 K radiation. We have aluminum plates connected to the 50 K cold head that fully enclose the 4 K stage, and the outer surfaces are covered with multi-layer "super-insulation", which are thin aluminum-coated mylar sheets that reflect out most of the thermal radiation. We have highly thermal-conductive copper C101 plates fully cover the 1 K stage, with similar super-insulation covers. Both layers have small apertures for the molecule beam to exist, and glass windows that allow lasers to go through while blocking a

large part of the thermal radiation.

The 4 K thermal shields also provide an important function of cryo-pumping the buffer gas, which is helium in our source. With the complicated structures in the CBGB, normal vacuum pumps attached outside the chamber won't be able to efficiently remove the buffer gas after it leaves the cell. The build-up of buffer gas can cause thermal performance to degrade, as they conduct heat from the outer layers to the inside. Also, for experiments utilizing the molecule beam coming out of the cell aperture, buffer gas buildup in the beam line can significantly attenuate the number of target species in the beam. Therefore, we have a layer of activated charcoal stycasted on the inside surfaces of the 4 K thermal shields.

Activated charcoal has a large surface area due to its porous structures, and can accommodate a huge amount of gas particles, so it acts as a pump that can continuously remove the buffer gas. Of course, they eventually saturate once a large portion of the surface has buffer gas adsorbed onto them. Hence we typically will run a quick de-sorb procedure at the end of the day by running a heater to increase the temperature of the 4 K heat shields above 10 K, and once every few weeks, we would run a de-ice procedure by increasing the temperature further to about 70 K to remove the build-up of contaminant gas particles.

While we briefly attempted running with a heated fill line in our lab, we mostly used mixed powder target ablation to produce our molecules. By the time of writing, we are satisfied with our YbOH production through these targets. While it is still a bit of alchemy, we have arrived at the current level of optimization mostly just through trial and error. For YbOH targets, we know three important factors that almost certainly increase the yield and consistency of the target. 1. All the components should be fine-grained. We use a grain size of 200 mesh, which is 200 openings across 1 inch of screen. 2. Binder is important. We add 4% of PEG in the target mix by weight. 3. Yb powder works wonders.

While different OH sources don't seem to make too big of a difference, having Yb powders in the target increases yield significantly. In fact, with our sources, Yb atoms seem to naturally have the highest density of any atoms produced by ablation. Specifically for the YbOH target, our standard mixture is now a 3:2 Yb and $Yb(OH)_3$ stoichiometric mix plus 4% PEG, where stoichiometric means that there's an equal number of Yb and OH in the mix. Based on my testing, the ratio doesn't matter much in the target. I've tried ratios of 1:3 and 3:1 between Yb and OH in the target, and there's no statistically significant difference in yield and consistency when all

other conditions are held equal.

Here is the typical procedure we use for making targets: first we grind down any powder that is not as fine as 200 mesh using a powered ball grinder; then, the powders are weighed and thoroughly mixed to the desired ratio; a portion of that mixture is weighed out for a single target, typically around 0.8 g, and is put in a cylindrical press die; the die is placed under 10 MPa of pressure with a hydraulic press. Optionally we would add some water in the forms of droplets or Epsom salt to the mixed powder and heat up the die above 100 degrees Celsius. Such a process is typically called "cold sintering" and is aimed to promote even distribution and tight binding for the targets. We have some evidence showing cold sintering helps improve the performance and consistency of the targets [29].

There are many parameters of the CBGB we tried to optimize. Among them, the when and how to shoot in the enhancement laser light is worth noting. One of the first things our lab showed is that we can significantly improve molecule production by resonantly exciting the Yb atoms into a metastable excited state, in a process we called chemical enhancement [34]. The enhancement laser is the high power (>300 mW) Continuous Wave (cw) laser we used to excite Yb atoms for chemical enhancement. The geometry of the enhancement light is quite tolerant, for example, we can illuminate the region right before the cell aperture, and we can observe a similar enhancement effect when we position the laser around the ablation region, as long as the laser power is high enough to saturate.

Typically, we shutter the enhancement to only allow light in for a few tens of ms starting with the ablation. This way, the high power cw enhancement light introduces minimal heat load to the cell. For the 1 K source, however, we find it beneficial to start that time window around 50 ms before the ablation. We call it preheating. It on average increases the molecule signal by a factor of ~ 3, as shown in Figure 3.7. Our theory is that the extra heat releases superfluid Helium in the cell for ablation, which increases the extraction of the target species from the cell. Higher buffer gas flow usually means better extraction for CBGB; however, above a certain point, the flow rate overwhelms the cryo-pumping ability of the charcoal inside the chamber, and the number of target species will drop in the beamline as a result. Hence, there's often a sweet spot for the Helium flow rate. However, the extra puff of buffer gas released by preheating doesn't contribute to extra helium flow over time, so it doesn't cause buffer gas buildup.

Finally, a new aspect of the 1 K source compared to our 4 K source is the closed

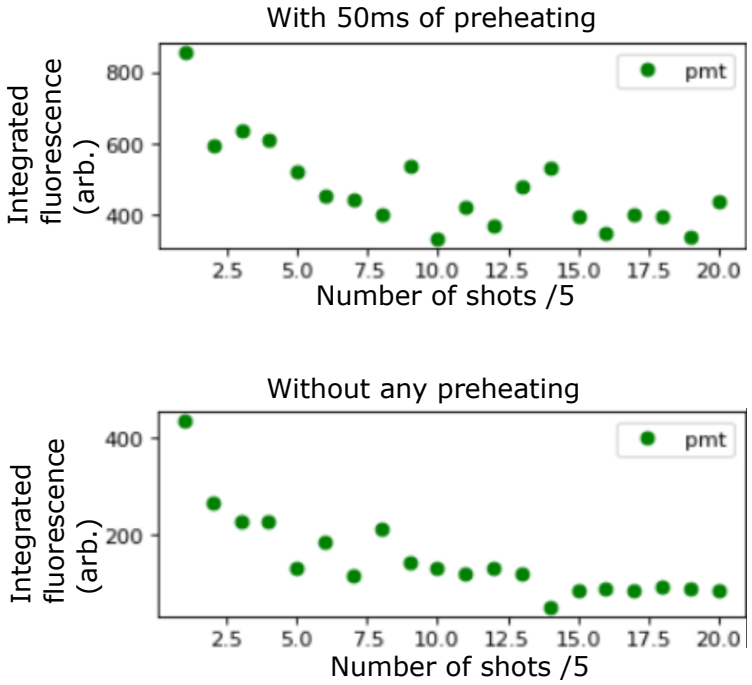

Figure 3.7: Data showing the effect of preheating on the molecule fluorescence signal in the beam extension. It is proportional to the number of molecules extracted from the cell. As with most signals from continuous ablation of a mixed target, there's a decay in molecule production with shot after shot. The preheating increases the molecule extraction by a factor of ~ 3 to 4 at the steady state.

cycle pumped helium system that brings the final stage coldhead from 4 K to about 1.4 K. While it is an integrated commercial system from Cryomech, we had to do extensive work to debug and upgrade it to make it work reliably. The work is mainly done by Phelan Yu and Ashay Patel, with designs and ideas from the Doyle lab at Harvard. The main issue with the original system is that, compared to the pulse tube part of the cryocooler, the pumped helium stage is not a true closed system. There is a recirculating scroll pump that collects the gas phase helium back into the loop, and we have to introduce helium from a gas bottle to initialize the cycle. Both the recirculating scroll pump and external helium source introduce contaminants into the system. As a result, the 1 K helium line is constantly clogged, and can easily cause overpressure by a liquid helium boil-off process. Therefore, we have to add extra filters, a liquid nitrogen cold trap, and a big dump volume to solve these problems. While the system now works reliably, after almost a year of work, it still is not a turn-key system, since we have to top off the liquid nitrogen cold trap from time to time in order to prevent clogs.

There are many more considerations for running a CBGB source. For more information, see ref. [29, 33, 35]. There is a lot more work to be done to improve the 1 K CBGB source, to produce molecule beams with higher density, lower temperature, lower velocity, and in a more consistent manner. Even in the short term, we have planned upgrades like a shortened heated fill line, a laser fiber access port to the cell, a second-stage cell, and separate pulse lasers for preheating.

3.2 Absorption and fluorescence

The main experimental methods for most AMO labs are laser absorption and laser-induced fluorescence. One measures how much laser light is absorbed by the atoms or molecules. The other measures how much light the atoms or molecules emit after being hit by laser light. In many cases, we can use these interchangeably, since both can measure if the laser is on resonance with a transition, how strong the transition is, how many atoms or molecules are illuminated, etc. Typically, absorption is more tolerant to noise, and fluorescence is more sensitive to small signals. There are specialized techniques like FM absorption spectroscopy that can make absorption much more sensitive to small signals [30], and off-diagonal fluorescence collection that can significantly improve the ability to block out noise. There are also geometry considerations when choosing the two methods.

For example, when measuring molecule production inside the cell, we use a pair of windows near the aperture of the cell to send laser light through (see Figure3.4). The laser is launched on one side of the chamber and monitored on the other side with a photodiode, both with a rigid mechanical connection to the chamber, making any vibration common mode. The ablation of the target and the introduction of the enhancement laser create a lot of light of various frequencies that can linger for a few milliseconds. By doing absorption through a small window and using bandpass light filters, we can easily extract the pure molecule absorption signal.

We can use such signals to calculate the amount of molecules produced with a simple optical depth calculation [18]. We can also do similar absorption right in front of the aperture, to monitor the number of molecules extracted out of the cell, which can be used for normalizing other signals downstream of the molecule beam, canceling out the differences caused by shot-to-shot fluctuations of the molecules production. Since the shot-to-shot fluctuations of the ablation are typically the main source of systematic errors in most of the studies of the molecule beam, it is crucial to have a reliable in-front-of-the-cell absorption setup to provide normalization.

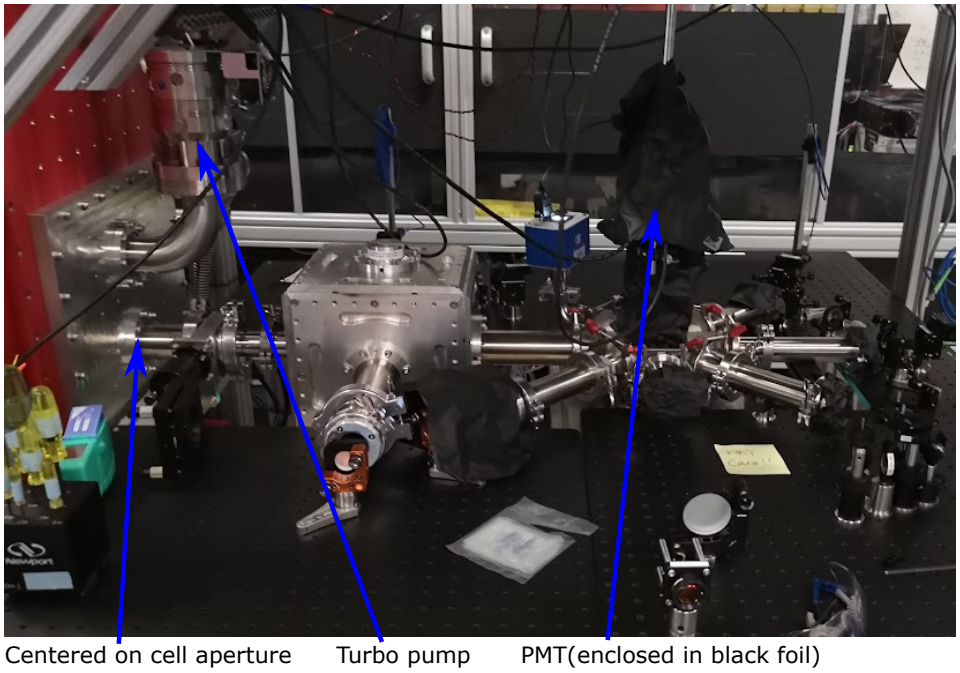

Figure 3.8: Photo of a typical beam extension setup. The PMT is enclosed in multiple layers of black foil to block room light. There are two more turbo pumps under the table, pumping on the beam extension.

For most of the experiments, like spectroscopy, we use laser induced fluorescence of the molecule beam in the beam extension part of the apparatus. With a small sacrifice of molecule density, we have much more flexible optical access and better optical noise blocking, like reduced light scattering with blackened chambers and better windows. Typically, we have multiple laser accesses on the horizontal plane, and the fluorescence is monitored with vertical access via a light pipe into a photomultiplier tube (PMT).

Fluorescence model for transitions with dark states

In the absence of dark states, we understand intuitively that as we increase the laser power addressing a transition, the fluorescence signal initially would increase linearly, until a saturation power is reached, and then the fluorescence signal would only change by a very small amount. In most experiments, saturation is desired, since the signal would be less sensitive to fluctuations of laser power. For transitions with dark states, as is almost always the case with molecules, the saturation mechanism is different. As one can intuitively imagine, once the particle drops into a dark state, it will no longer contribute to the fluorescence. Hence, saturation is reached when the photon cycling rate matches the traveling time of the particle through the region

illuminated by the laser, such that on average, the particle would drop into a dark state before leaving the laser beam.

As a result, molecule transitions are typically easier to saturate in fluorescence. One might think it would also make the saturated lineshape almost like a top hat when scanning a laser frequency with power much higher than the saturation parameter. The reason is that unlike the normal saturation mechanism, where the photon cycling rate will still increase very slowly as detuning decreases on a highly saturated laser, saturation caused by dark states won't increase at all. As a result, the expected line shape of the fluorescence over frequency would look like the blue line in Figure 3.9(A), and the fluorescence over laser power above saturation would look like the blue line in Figure 3.9(B), qualitatively different from the normal saturated lineshape of Lorentzian that's the orange lines in the same figures.

However, in practice, we almost exclusively see the lineshape of the blue line in Figure 3.9(C) instead, even when operating in a high saturation regime. In an effort to better understand how molecule saturation works. I did some simulation and model building to figure out why the lineshapes of our spectroscopy still have harp peaks when the laser is operating in a highly saturated regime. The conclusion is that the sharp peak is caused by the fact that our laser beam is smaller than and thus doesn't fully cover the molecule beam. When the condition is flipped and the laser beam is much bigger than the molecule beam, then the lineshape becomes the expected Lorentzian with a chopped flat top.

I developed my own model to calculate the lineshape of the case where the molecule beam is bigger than the laser beam. Though it fits with the data and simulations quite well, it is cumbersome and therefore discussed in more detail as an appendix. The main takeaway is that in order to have an expected spectroscopic lineshape it is important to run the experiment such that the laser beam fully covers the beam of species under study.

3.3 Spectroscopy: molecule features and common techniques

A lot of the work after the CBGBs were built, was spectroscopy. While there is some prior spectroscopy in the literature [36], considerably more is needed in order to fully know how to manipulate YbOH and use it for precision measurements. As mentioned in the previous chapter, we use effective Hamiltonians to model and describe molecules. Spectroscopy helps us to determine the coefficients and parameters for the coupling/interaction terms. It is often important to directly

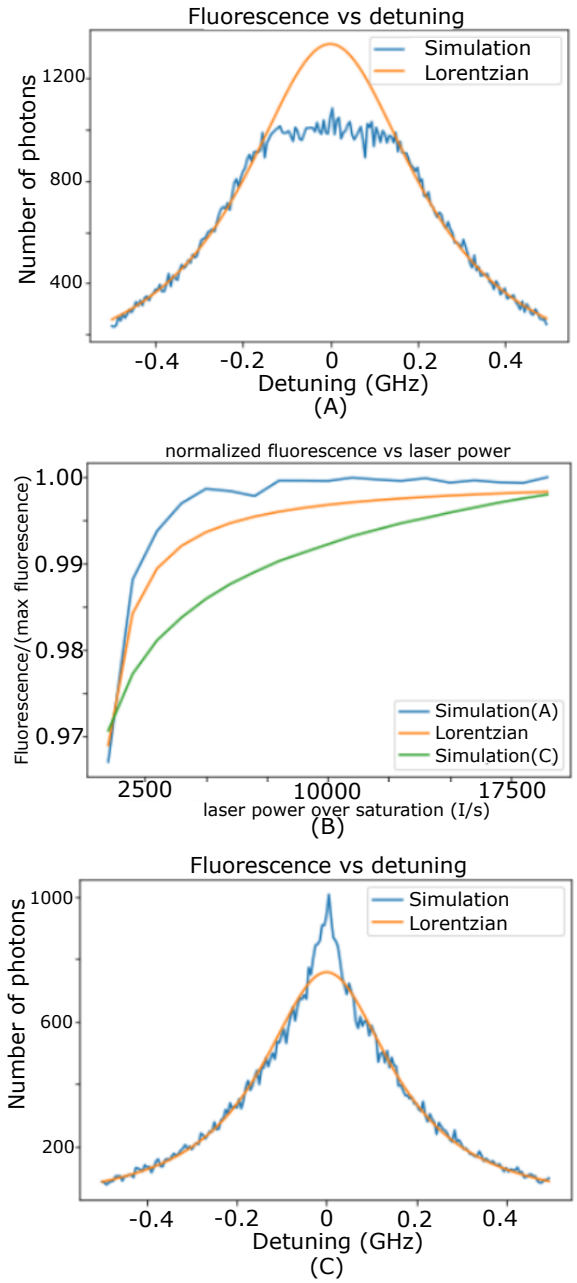

Figure 3.9: Figures for the study of saturation caused by dark states. (A) Simulated lineshape of saturation caused by dark state in blue. The molecule beam is much smaller than the laser beam in the simulation. Lorentzian lineshape of normal saturation under similar conditions in orange. (B) Normalized fluorescence amplitude vs laser power in saturation parameter. Blue is the simulation in (A), Orange is from the typical Lorentzian calculation, and Green is the simulation in (C). (C) Similar to (A), except the blue line is from a simulation where the molecule beam is much wider than the laser beam.

measure important transitions as well. For example, when trying to cycle photons on ^{174}YbOH, we do pump-probe spectroscopy to find the dark states so that we can use repump lasers to address them, without the need to fully characterize all molecular parameters.

For day-to-day experiments, it's often the case that we perform quick spectroscopy measurements, just to confirm that we are addressing the correct lines and that experimental parameters are nominal. We would mainly use two probe lasers: one right in front of the cell aperture, taking absorption measurements on a very well-known transition for normalization as previously mentioned. The other is the fluorescence laser typically downstream of the molecule beam, in the beam extension setup, where the probe laser is typically transverse to the molecule beam, and a PMT will monitor the fluorescence at the cross point. We scan the fluorescence laser frequencies across the interested range and record the fluorescence signal normalized by dividing it by the normalization absorption signal.

We have also performed two major systematic spectroscopic studies on YbOH. The first one is the spectroscopy to figure out the fine and hyperfine structures of the odd isotopologues ^{171}YbOH and ^{173}YbOH, which have Yb nuclear spin of 1/2 and 5/2. The results and details are published in [18]. The measured spectroscopy data provides detailed information about the molecular structures that are crucial for later experiments. Also, as mentioned at the end of Chapter 1, the CPV sensitivity parameters are calculated using ab initio or semi-empirical methods. Our high resolution hyperfine spectroscopy provides important reference and verification for these methods.

Here I discuss two techniques used in the spectroscopy experiments. The first is the use of chemical enhancement to disentangle the spectral lines from different isotopes. There are 6 naturally abundant and stable isotopes of Yb. As a result, a typical spectrum of YbOH includes contributions from all these naturally abundant isotopologues, since the isotope shift is comparable to many relevant splittings in the molecule structure. There can be a few tens of lines coming from different isotopologues in potentially different rotation and spin-rotation states within a ~GHz frequency window. We can clean up these overlapping messes by comparing the spectrum taken with and without enhancement laser enhancing the production of one specific isotopologue. This process is described in detail in [18], and was critical to understanding the very complex ^{171}YbOH and ^{173}YbOH spectra.

Another technique commonly used is the "combination difference". Often we

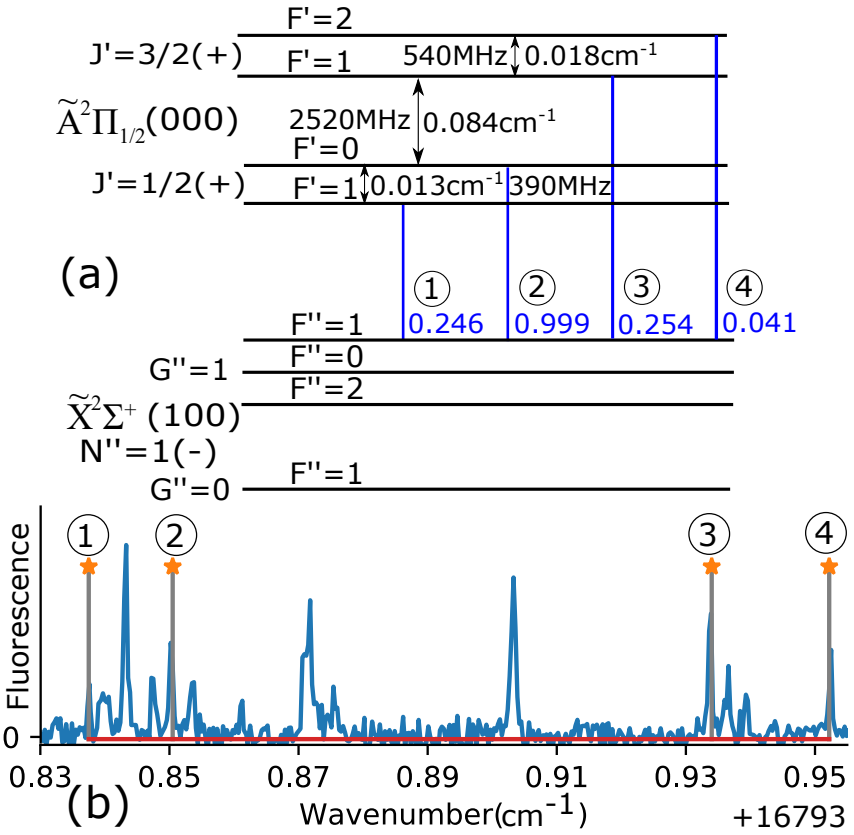

Figure 3.10: Example of $v'' = 1$ spectroscopy for ^{171}YbOH. Transitions are identified by matching spectral splittings to known excited state splittings [18]. It will be further discussed in chapter 4, which is adapted from [37]. (a) is the level diagram of the involved ground and excited states, with calculated branching ratios for the target transitions. (b) is the measured fluorescence spectrum with the same four transitions marked in (a). Some of the unmarked peaks nearby are transitions from $F'' = 0, 2$ ground hyperfine levels to the same excited states, identifiable via the common splittings.

already know what the ground state or the excited state looks like, and we are trying to figure out the other. Say we know the excited state structure and are trying to study the unknown ground state. After performing a spectroscopy scan of the transitions between the ground and excited states, we can search for transitions that are spaced apart in the same pattern as the known splittings in the excited state, and use these transitions to identify a single level in the ground state manifold, typically with the help of selection rules.

Figure 4.5 shows an example of state identification using the known splittings in the excited states. That is much easier than when we don't have anything exactly known about both the ground and excited states, other than the guidance of effective

Hamiltonian estimations. After all, spectroscopy is to figure out the exact parameters for the effective Hamiltonian. Before that, we have to use ab initio calculations or guess by scaling the parameters of similar molecules, which may provide a good starting point but is never sufficiently accurate. However, sometimes we do not even have these estimates, for example, if we are examining a state of unknown origin. In that case, we will still use the method of combination difference, trying to find some combinations of lines with common splittings repeating in multiple places.

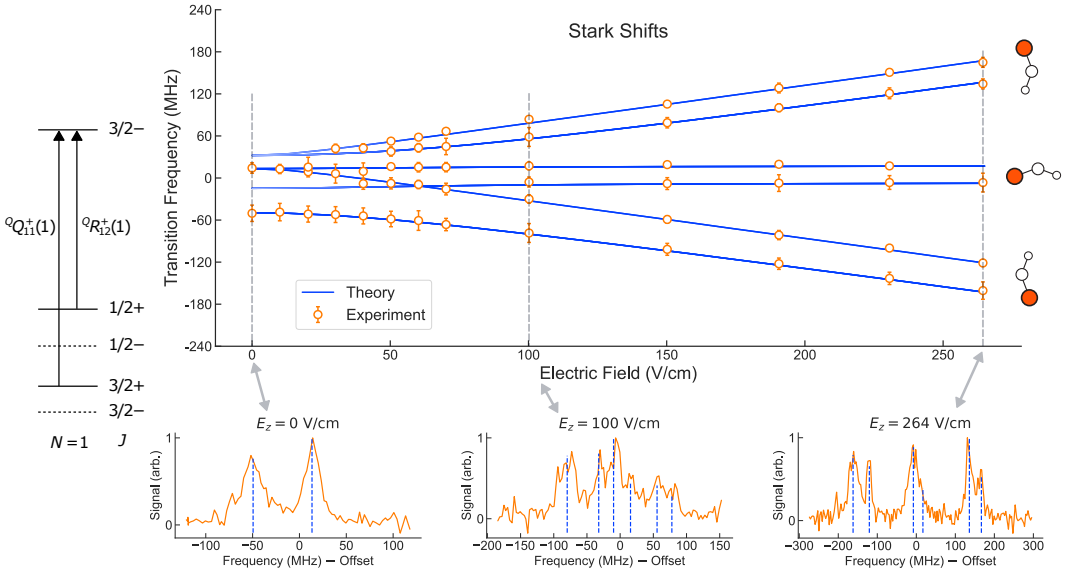

Figure 3.11: Stark spectroscopy of ^{174}YbOH in a bending mode, taking from [30]. It demonstrates how easy it is to fully polarize the molecule using a moderate electric field. For a detailed discussion, see [30].

The second spectroscopic study is of the bending mode of ^{174}YbOH. The bending mode is what provides the crucial parity doublets with small splitting. Future CPV precision measurement experiments will be done on states in the bending mode. We call these the "science states". Therefore, it is crucial that we know these states well, and unlike other typical studies where we just need to know where the lines are, we also need to figure out how these science states will behave under different electric field and magnetic field conditions. The results and discussions of this spectroscopy study are in [30]. Here I'd like to discuss the result related to molecule polarization, or spatial alignment, and the spectroscopy technique of pump-probe.

Figure 3.11 shows the result of Stark spectroscopy on states in the bending mode. By tracking the changes of transitions to the common excited state under different electric fields, we track how the ground states, which are in the bending vibration

mode, shift under the applied electric field. Such study is crucial for future precision measurement experiments because it not only provides important parameter fits in the effective Hamiltonian but also helps identify the internal co-magnetometer states, where the internal effective E field is flipped while everything else stays constant. We also showed that in order to fully polarize the molecule in the bending mode we only need to apply an E field of $\sim$ 100 V/cm, a much smaller number than most atoms and diatomic molecules thanks to the parity doublets with much smaller splittings.

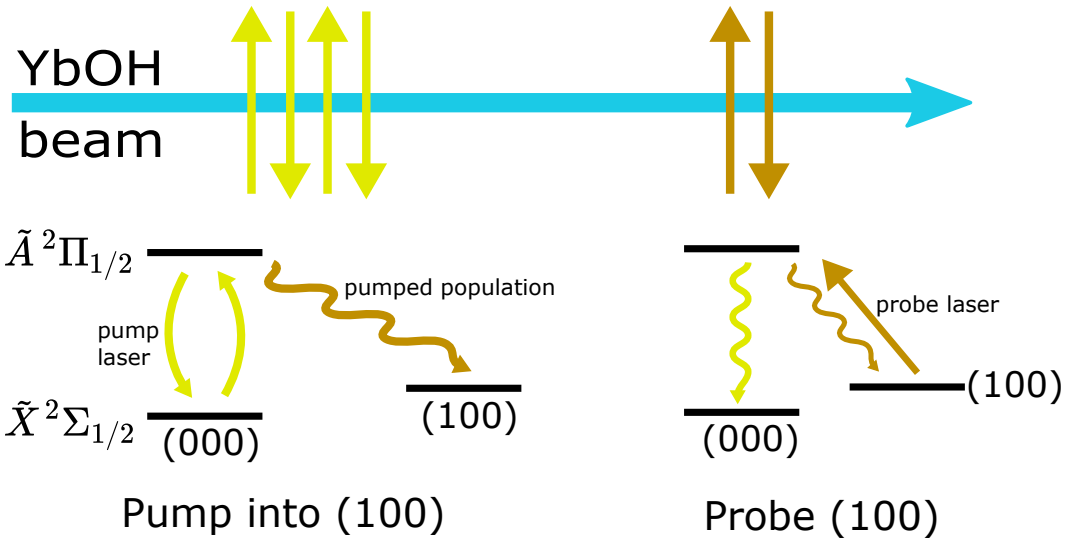

Figure 3.12: Schematic for a pump-probe measurement, adapted from Figure 4.3 in Chapter 4. By measuring the population transfer into the hyperfine levels of the first excited vibration state (1,0,0), we can confirm the state assignments of the hyperfine levels.

Finally, the technique of pump-probe is used in the bending mode spectroscopy and is commonly used in many spectroscopy experiments, typically with the goal of confirming state assignments. This method is shown in Figure 3.12, and works by using one laser to transfer the population and another laser to confirm the population changes. It is a form of double-checking. For example, we can increase the population of some specific hyperfine levels in an excited vibration mode by optically pumping the population out of those same hyperfine levels in a ground vibration mode, so if we see a signal increase of some transitions after that pumping, then we can be sure that these transitions originated from those hyperfine levels. We can also deplete the population in a specific ground state by driving transitions to some excited states. If later we detect a loss of signal for certain transitions we are studying, then we can be sure that these transitions originated from the same

depleted ground state. These can be used as a quick way to double-check after we assign state labels using techniques like combination difference as mentioned before.

3.4 External cavity diode lasers

As a molecule lab, we need many lasers of different frequencies that can address all the different structures of the molecules. Especially since we are working on novel species of molecules and performing many spectroscopic studies as mentioned in the previous section, we use many external cavity diode lasers (ECDL), which are tunable, stable, and have the ability to swap laser diodes to change output frequencies. To accomplish the work described here, I have designed and built 6 home-made ECDLs adapted from a Kang-Kuen Ni lab's design, and I've set up and maintained almost a dozen ECDLs from multiple commercial vendors like Moglab, Toptica, and Vexlum (theirs are technically VECSELs).

In order to turn a laser diode into a single-frequency tunable laser, we need a way to select and stabilize the output frequency. As the name suggests, ECDLs select the output frequency using an external cavity, which is formed typically between a reflecting surface in the diode and another reflecting surface outside the laser diode. However, these external cavities typically have free spectral ranges on the level of $\sim$ GHz, while the gain profile of the diode is typically a few to a few tens of nm wide, which translates to $\sim$ 10 THz. As a result, the output frequency will be randomly chosen among the vast range of possibilities, and it will jump around uncontrollably and frequently if there are no other ways to preferentially select out a smaller range of frequencies. There are two common ways to do that. One is putting an interference filter in the external cavity [38], which is a relatively new method with the potential benefits of easier finding the right filter and better performance. The other is using a reflective grating in a Littrow configuration [39], where the grating serves as both the frequency-selective element and the reflecting surface forming the external cavity.

The homemade ECDLs I made in our lab are mostly the type using grating in Littrow configuration. We also made some ECDLs using filters, mostly with fiber-coupled gain modules from Innolume. They were used for YbOH detection very early on and for metastable Helium spectroscopy in an undergrad research project. The grating ECDLs, on the other hand, use the standard 5.6mm or 9mm TO Can laser diodes, which are very widely available across the wavelength range and can be as cheap

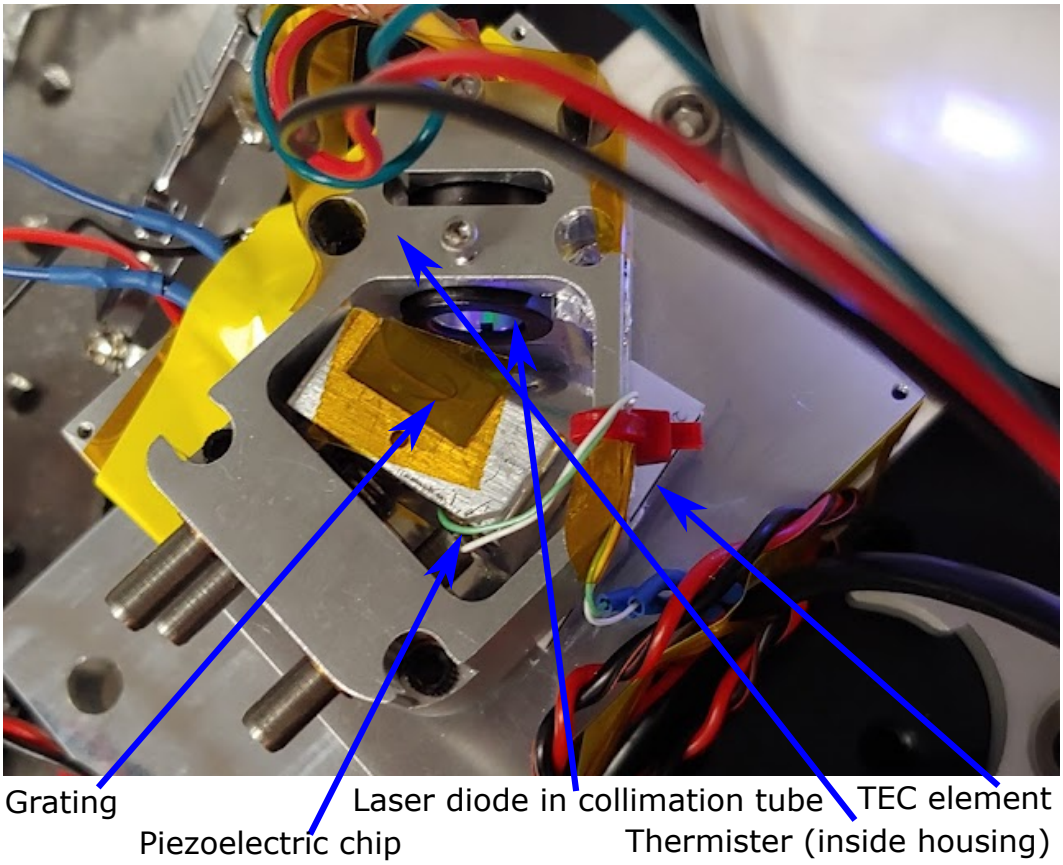

Figure 3.13: Photo of a homemade ECDL in a prototyping process.

as a few dollars a pop. We use standard Thorlabs collimation tubes to house and collimate these diodes.

Figure 3.13 shows how these grating ECDLs typically work. The main optical components are just the laser diode, the collimating lens, and the grating. The other important components are the thermister right near the collimation tube, the TEC element for stabilizing the temperature based on feedback from the thermister, and the piezoelectric chip for fine tuning the cavity length of the cavity. Once all the electrical hookups are done, the procedure for setting up new laser diodes is quite straightforward.

First, put in and secure the laser diode inside the collimation tube. Then adjust the collimating lens position so that the laser light coming out of the collimation tube is as well collimated as possible. Finally position the collimation tube inside the laser housing, such that the output beam spot's long axis is horizontal. The grating will be positioned such that the groves are vertical, so that the laser spot, typically elliptical, will have its long axis cut across as many grooves as possible. Then the

grating should be angled for a Littrow configuration where the first order diffraction beam comes back to the laser diode. When all these are set up and aligned, it is expected that the lasing threshold of the laser diode will be lowered, showing that there is some feedback into the diode.

There are various considerations to achieve good feedback from the grating. One very important feature is the grating efficiency. Often the grating that has the best efficiency for the target frequency also has a bad diffraction angle, such that the output beam, typically the zeroth order diffraction beam, and the input beam form an angle much sharper than the convenient 45 degrees (see Figure 3.13). Because such sharp angles can cause output beam clipping with the laser housing, design modifications are needed to accommodate these high-efficiency but bad-angle gratings. However, the improvement of stability and tuning range of the laser resulting from the better grating efficiency is worth the geometry constraints. The other important factor that might impact feedback is the collimation, which is often surprisingly tolerant. That is really helpful for our laser design since we can no longer adjust the focus once the collimation tube is installed inside the laser housing.

Once good feedback is established, usually after fine tuning the angle of the grating, the laser should output a relatively stable single-frequency light. The frequency of the output light can be tuned coarsely by adjusting the horizontal grating angle and the temperature of the laser, and be fine-tuned by adjusting the voltage on the piezoelectric chip. The stability depends on a few factors that the design tries to control. The first is the mechanical vibration isolation. By having the laser housing compact and machined from a single block of aluminum, any mechanical perturbation would be common-mode to all the optical elements of the laser, thus having minimal impact on the frequency stability. Another is the temperature and pressure fluctuation, which is again helped by the compactness of the unibody design. Also, outside the main laser body, we have a small housing that encloses everything, with an anti-reflection coated window on the aperture, and rubber-covered holes for electrical wires. All the seals are designed to be good enough that we can deep cool the laser.

I made one such deep cooled ECDL. Using water cooling blocks on the hot side of the TEC element, we can pull the temperature of the laser down below 0 C°. The reason to do that is to further extend the tuning range of the laser into the blue. For example, if a diode is specified to lase in a frequency range of 400-410 nm, with a normal operating temperature of 20-100 C°. By cooling it down to -10 C°, the

bottom end of the lasing range can be pushed down to around 397 nm. Typically, every 10 degrees Celsius of cooling corresponds to 1 nm of wavelength to the blue.

We used our deep-cooled ECDL to address the Yb transition from the ground state to the $^3P_2$ metastable excited state, which is 507 nm in wavelength. There are quite a few options for commonly available laser diodes around the 520 nm wavelength, but the lowest possible diodes only go down to 510 nm. Laser diodes are manufactured with significant discrepancies in their natural wavelength range. Usually, for diodes of scientific lasers, there are post-production selection processes that pick out diodes that fit the spec sheet, and they are typically labeled as tested. Untested ones are typically much cheaper and can have their natural lasing wavelength near one extreme of the range. Hence, we bought a dozen of these untested 510 nm diodes. We quickly tested all of them and picked the one that naturally lased with the lowest wavelength. We were then able to pull the wavelength down to the required 507 nm using deep cooling. The laser was able to run stably over a long period of time without any condensation observed, and we were able to observe the metastable transition as expected.

3.5 State-preparation and spin-precession tests

After the bending mode experiment, we now have a good grasp of the structures of the science state of ^{174}YbOH which we will use for CPV precision measurements. Because of the complicated structure, the schemes for spin-precession measurement are novel and untested, so before building the science chamber, the apparatus for measuring nMQM with high degrees of control over electric and magnetic fields, we have to validate the novel schemes for preparing the initial quantum states and reading out the final states after the precision. This is a project led by Arian Jadbabaie, and there is more detailed information on all aspects of the tests in his thesis [29]. Here I will discuss the details of the part that I contributed, as well as some big-picture physics that are important for future experiments.

Spin-precession is a crucial process for many quantum physics experiments, usually depicted on a Bloch sphere. Typically the pictures would show a state prep step of rotating a vector around the x-axis pointing the state vector to the equator of the sphere, a precession step of the vector rotating around the z-axis as time evolves tracing around the equator, and a readout step of rotating the vector around the x-axis again resulting in the vector landing back to upper or lower hemisphere depending on where it was on the equator. Such a picture is a classic because

the spin-precession procedure is widely used as a way to measure small energy differences, by converting the energy ΔE into a phase $e^{i\Delta Et}$ which is then measured by a projective measurement. Many methods and techniques have been developed around this concept, and they will come in handy since we are dealing with systems far more complex than the simple two-level system depicted by the Bloch sphere.

The main difficulty for us arises from the hyperfine splittings caused by the hydrogen nuclear spin. While it was something we could ignore in the spectroscopy discussion, because the splittings are too small to resolve, they become relevant when trying to realize quantum control.

Hence we decided to study the hyperfine structure involved, using two-photon detuned Raman spectroscopy. The two-level system we were interested in was a pair of spin-rotation states in the bending mode ground state $\tilde{X}$(0,1,0) N=1 J=1/2 and $\tilde{X}$(0,1,0) N=1 J=3/2, both with parity +. We can drive transitions between them by connecting both of them with an intermediate state of parity −. We typically use the bending mode excited state $\tilde{A}$(0,1,0) J=3/2. By having a large detuning ($\sim$ 1 GHz) away from this intermediate state, we can have an almost pure two-photon transition between the two ground-state spin-rotation levels with a linewidth of $\sim$ 100 kHz, which is much narrower than the typical linewidth of $\sim$ 10 MHz for normal transitions in our other spectroscopic studies. Also, because of the far detuning, there's almost no population transfer into the excited state, so there's almost no loss to the dark states in the two-photon process.

The two ground spin-rotation states J=1/2 and J=3/2 are separated by about 60MHz. The two-photon lights are generated using a single laser, an 1154 nm ECDL amplified with a Raman fiber amplifier, and then doubled with second-harmonic generation. The resulting 577 nm light is then sent into an Acousto-optic modulator (AOM) setup to create the two legs of the two-photon process. We used two AOMs that have a central frequency of 100 MHz and a bandwidth of 25 MHz. In order to achieve the 60 MHz splitting and have the capability of scanning the splitting, we sent one part of the laser light into an AOM, which shifts the wavelength by about 120 MHz, and we sent the rest of the laser light into the other AOM in a double pass setup, which shifts the wavelength by about $90 \times 2 = 180$ MHz in the same direction as the single-pass AOM. As a result, the wavelength difference between the two beams is 60 MHz, matching that of the spin-rotating splitting.

An important advantage of using a double-pass AOM setup is that it allows for a much bigger range of frequency tuning [40]. Typically with our setup the single-

Figure 3.14: AOM setup used for generating the two-photon light, illustration made by Arian Jadbabaie. AOM 2 is in a double-pass setup. Labels: HWP, half-waveplate; QWP, quarter-waveplate; PBS and BS, polarizing and non-polarizing (50/50) beam-splitter; H and V, horizontal and vertical polarization; L and R, left- and right-handed circular polarization [29].

pass AOM frequency can be tuned by $\sim$ 1 MHz without losing significant power at the output fiber-couple. The double-pass AOM can be tuned by $\sim$ 10 MHz, which can be further increased by using a more optimized setup, for example, by using a curved retro-reflector instead of the plane mirror.

The full AOM setup is shown in Figure 3.14. It creates two coherent laser beams with frequencies separated by an amount tunable around 60 MHz and recombines them into a single fiber. It will significantly simplify the two-photon measurements at the CBGB source since the two components will always be perfectly overlapped. We were able to map out the four hyperfine states from the two spin-rotation components, by doing two-photon detuned Raman spectroscopy with the output of the AOM setup. These four states are J=1/2 F=0, J=1/2 F=1, J=3/2 F=1, and J=3/2 F=2, cleanly resolved when scanning the AOM frequency. Now we are ready to test the spin-precession scheme using them.

Before talking about the Ramsey interferometry using the detuned two-photon transition, with light generated by the AOM setup, it's worth mentioning the discussion

we had about whether we should use detuned two-photon transition or coherent population trapping (CPT), and whether we should use AOMs or electro-optic modulators (EOMs) to create the laser frequency splittings. Of course, we now know what worked in the end, but it's worth sharing what we learned from our discussions and tests.

We had EOMs already set up with the 577 nm laser, from the photon cycling experiments for odd isotope YbOH. We initially tried to use them to generate sidebands as the two legs of the two-photon transition, to be described in Chapter 4. The advantages of using EOMs are that they have a much bigger scanning range (20 GHz), and have already been set up. The disadvantages are that the two legs of the two-photon can't have different polarizations and the destructive interference between the sidebands of the EOMs. The latter point is elaborated in [29, 41].

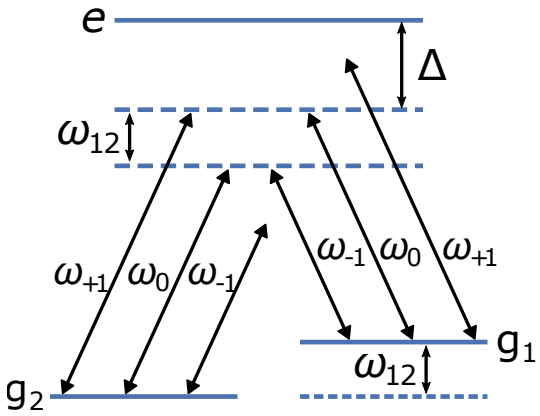

Figure 3.15: At least two sets of frequencies will match the two-photon resonance of ω_{12}, when using symmetric EOM-generated sidebands. Due to the opposite phase of the sidebands, these two sets will always perfectly cancel each other in destructive interference. Figure adapted from Ref. [29].

Basically, there are multiple sets of resonant two-photon linkage when the laser light coming out of a symmetrically (normal sinusoidal) driven EOM is used, and they always almost perfectly destructively interfere with each other, as shown in Figure 3.15. No matter which combination of sidebands and carrier frequencies are used, it can be mathematically shown that destructive interference will always show up. We did attempt to use some asymmetrical drives and successfully had some small two-photon signals from them. However, due to instrument limitations, the signal is poor and unstable.

Using CPT for the spin-precision test was an even more tempting idea. After all, the eEDM measurements with ThO at the ACME experiments used the CPT method for

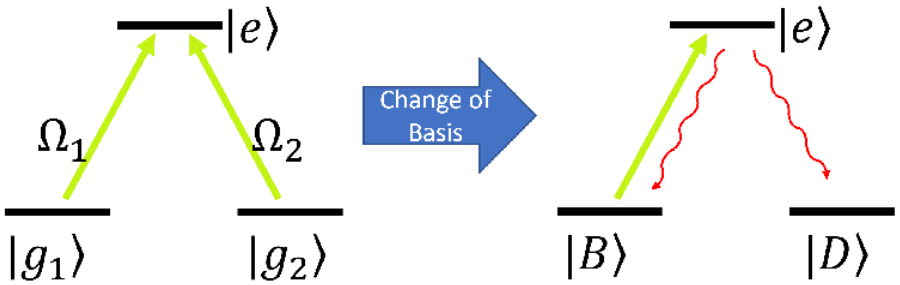

Figure 3.16: Schematic of coherent population trapping. When addressing transitions from two ground states g_1 and g_2 to a common excited state e, a dark state D will form from the superposition of the two ground states. As a result, the population will be pumped out of the bright state B and accumulate into the dark state. Figure adapted from Ref. [29].

state prep [15]. A simple picture of CPT is that when two different ground states are resonantly driven to a common excited state with coherent laser light, two sets of superpositions of the two ground states appear, with one of them being connected to the excited state by the laser, and the other being dark to the laser light due to opposite phase. See Figure 3.16. As a result, the population in the bright superposition is pumped out, leaving only the dark superposition population untouched. After that, depending on the time and precession rate, the dark superposition will precess into the bright superposition by some degree. We can then use the same CPT laser, preserving the relative phase between the two legs, to detect how much of the population has precessed back to the bright superposition, which gives information about the precession rate.

There are many advantages to doing spin-precession with CPT, including strong suppression of systematic uncertainties related to the CPT laser, since we are using the same laser beam for both state prep and readout, and the fact that the CPT process uses complete population transfer instead of relying on π pulse or similarly timed pulses. Unfortunately, it has a fatal flaw, specifically in our case. Since it uses resonant drives, the linewidth is the typical $\sim$ 10 MHz, making all the hydrogen nuclear spin hyperfine structures unresolved and on resonance. These unresolved states can cause two problems. If there are same number of excited states as the ground states, no dark state can be formed. Then, even when taking into account the ground state splittings introducing more ground states, all the transitions can destructively interfere with each other, significantly limiting the rate at which the population is transferred into the dark superposition. We attempted to

use polarization and selection rules to solve these problems. Again, we had some small successes but pivoted to the detuned two-photon transition instead due to SNR and E/B field considerations.

We were able to achieve all the necessary proof-of-principle tests for the Ramsey interferometry procedure that can be one day adapted to conduct nMQM beam experiments, using the detuned two-photon transition with light generated from the AOM setup. The specific states used were J=1/2 F=1 M_F=1 and J=3/2 F=2 M_F=2 in the $\tilde{X}$(0,1,0) ground state, and the excited $\tilde{A}$(0,1,0) J=3/2 F=2 state as the far detuned intermediate state. The Zeeman sublevels are lifted from degeneracy using a modest B field using a pair of Helmholtz coils. First, the initial population of one of the ground states is depleted by optical pumping. The two-photon laser beam coming from the AOM setup is first used for state prep, driving the transition to form a superposition between the two ground states. It is then retroreflected using a prism to read out the precession result by projecting the superposition back to the initially depleted state, only about 2 mm downstream. The final population of the state is then probed using fluorescence much further downstream where the light isolation is much better. We can plot the final fluorescence against both the RF frequency separating the two-photon, and the precession time, by adjusting the retroreflecting prism which controls the spatial separation of the state prep beam and readout beam. As expected, the former gives the classic Ramsey fringes and the latter gives the Ramsey oscillations. For the quantitative results, and a lot more other details, see Arian Jadbabaie's thesis [29].

3.6 Initial tests of sympathetic slowing/cooling with Rydberg Yb

Finally, I'd like to talk about the early tests we did for a fresh new idea brought by our new postdoc Chi Zhang, published in [42]. Since we produce a large amount of Yb atoms alongside YbOH molecules, if we can find a way to effectively thermalize the atoms and molecules after we have slowed or cooled the atoms, which is straightforward via laser cooling, then we are sympathetically slowing or cooling the molecules. Without using any tricks, it will require an extremely high density for the atoms to see any thermalization. In fact, that is something I confirmed with a quick test. However, Chi performed some calculations and modeling to show that exciting the atoms into a Rydberg state can significantly increase the collision cross-section between atoms and polar molecules, which is expected to be mostly elastic with high interaction energy.

I led the effort in performing some initial tests using the 1 K CBGB source, and existing instruments and components. The main challenges are producing Yb clouds with high enough density and excite enough of them to Rydberg states. Both of these challenges can be boiled down to having enough lasers and laser power. I thought there was a possibility that I could build enough ECDLs using existing laser diodes and components, and they would have enough performance, to create a cloud of Rydberg Yb atoms dense enough, that it would produce an observable effect on the molecule beam.

I was able to make a 396 nm ECDL, which produces a peak power of about 50 mW, a linewidth of about 5 MHz, and a wide tuning range of about 2 nm. Combining with an existing ECDL that drives the main Yb ground to $^1P_1$ transition, they can drive a two-photon transition to a wide range of Rydberg S states from n=20 to n=70, as shown in Figure 3.17 but only a very small amount, due to the low power and relatively wide linewidth. Fortunately, by the time of carrying out these initial tests, we have some existing non-resonant cavities that can build laser power by about 30 times, for multiple lasers of different wavelengths, at the location. More about this cavity is in Chapter 5.

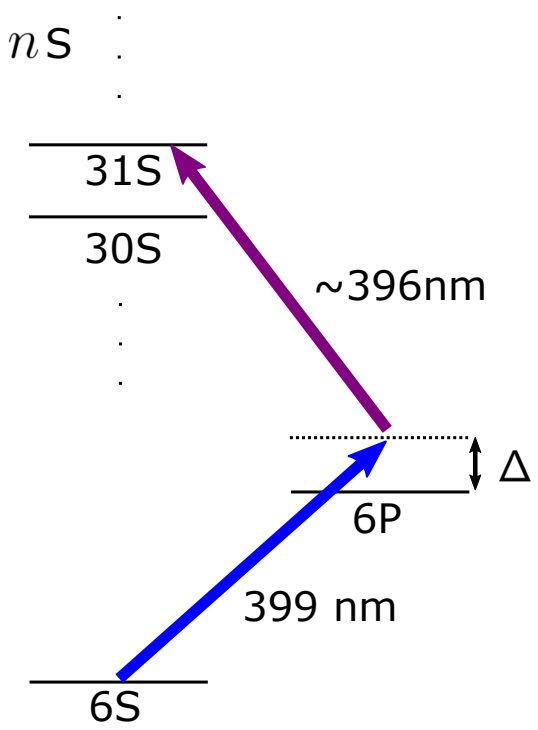

Figure 3.17: Energy level diagram of Yb, and the two-photon excitation scheme, with the Δ being the detuning from the intermediate $^1P_1$ state.

By sending the two Rydberg laser lights into the power buildup cavity, we were able to observe some ground state population loss with a Yb absorption probe about 10 mm downstream from the Rydberg lasers. The maximum loss observed is about 10%, as shown in Figure 3.18, which is mostly caused by Rydberg excitation. We are shuttering only the 396 nm laser, which addresses the upper leg of the two-photon transition, from 6P to 52S. Though most likely it's not 10% population being in the 52S state, since the Rydberg laser intersection region with the atom beam is quite big, around 10 mm in interaction length, so probably a significant portion of the population already cascaded down to the lower Rydberg states before the atom even leaves the Rydberg lasers.

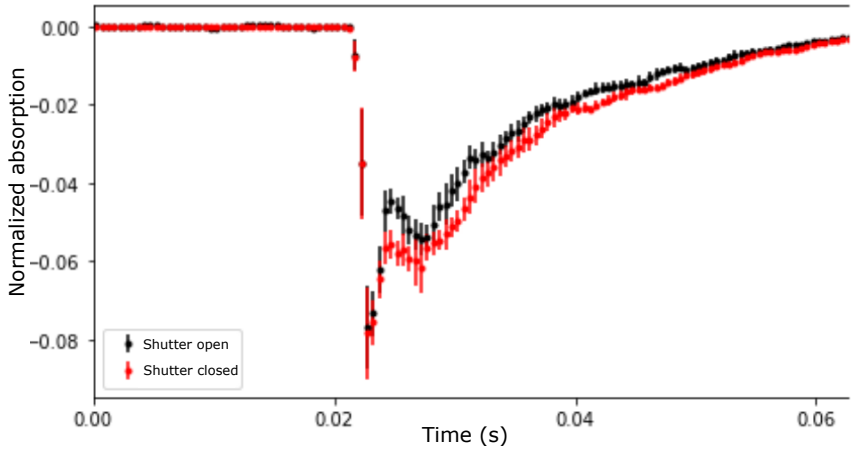

Figure 3.18: Yb absorption signals about 10 mm downstream of the Rydberg lasers. The shutter is on the 396 nm laser tuned to excite the transition from 6P to 52S. The absorption signal is normalized such that -1 means all laser light is absorbed. The loss of absorption when the shutter opens is mostly contributed by the loss of ground state population due to Rydberg excitation.

From the absorption signal, we also estimated the Yb atom density to be around $\sim 10^8$ cm^{-3}, which, according to Chi's estimation, is on the borderline of being dense enough if all of them are excited to n=52 Rydberg states. However, if the estimated collision interaction strength of $\sim$ 50 GHz is true, our Yb density might be still high enough to produce some observable effect on a small portion of the molecules. We then conducted a few experiments with cooling, slowing, and pushing the atoms, hoping to see any effect on the molecule beam. For these tests, another two 399 nm ECDLs were made. All the lasers were frequency stabilized using a wavemeter and fiber-switch combination.

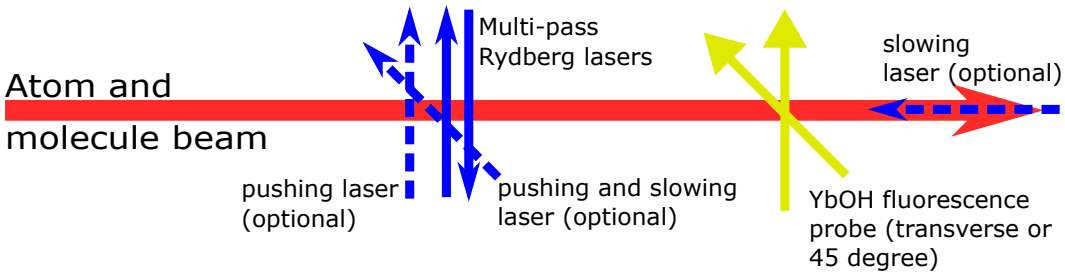

Figure 3.19: Scheme for some of the sympathetic cooling, slowing, and pushing tests. The blue arrows represent the Yb lasers and the green arrows represent the YbOH lasers. We used a transverse or 45-degree fluorescence probe to perform Doppler scans to measure the molecule beam velocity spread. Similar Doppler scans for Yb at the same location as the YbOH probe can be performed, not shown here.

See Figure 3.19 for the positioning of the lasers in the tests. The first test is a 1-D cooling test, using the multi-pass Rydberg lasers for both 1-D cooling of the transverse velocity spread of the Yb atoms and two-photon Rydberg excitation. The 6S to 6P transition for Yb is very strong, and we can cycle photons on this transition very fast, even with significant detuning. As a result, by red-detuning from the 1P intermediate state, the multi-pass Rydberg two-photon lasers can very effectively reduce the velocity spread of Yb in the transverse direction. We then performed transverse Doppler scans with YbOH fluorescence downstream, trying to see if there's any cooling effect on the molecules from collisions with the atoms. Unfortunately, we didn't see any effect significant enough to draw any conclusive conclusion.

We also conducted tests with pushing the atoms either transversely or at 45 degrees right before the Rydberg lasers. Again, none have resulted in any strong indication of sympathetic pushing of the molecules. Finally, we thought perhaps slowing would give us the best chance, since preferentially slowing the atoms with high forward velocity can effectively compress the pulse of the atom beam, increasing the atom density. Again, due to the strong Yb transition, we can slow Yb atoms by more than 100 m/s with a single 399 nm laser.

Typically, the atom and molecule beam has a forward velocity centered around 150 m/s and a spread of about 200 m/s. By shooting a 399 nm Yb laser upstream of the atom beam, tuned to be resonant with the 200m/s population, we can slow the atoms down to have a central forward velocity of about 50 m/s while almost completely eliminating atoms with velocity from 100 m/s to 250 m/s. The tricky part is to

slow the atoms at the right time. If we slowed the atoms too early, it could cause the density peaks of the atoms and molecules to separate, reducing the amount of possible collisions. To solve that, we have the slowing laser behind a shutter and timed it such that, based on time of flight measurements, most of the slowing happened right before the Rydberg excitation.

Unfortunately, none of the attempts yielded anything conclusive. We tried a wide range of parameters, including different amounts of velocity differential between atoms and molecules, different Rydberg n levels, and different initial velocities. While had some promising glimpses from time to time, they were all excluded due to systematic effect or low SNR. Fundamentally, we are limited by the initial density and laser power. With our 1 K CBGB source, we can try ablating our target with higher energy laser pulses, which will produce higher atom densities at the cost of initial velocities, and vice versa.

We have even tried to implement a simple 2-D cooling of Yb right after the CBGB cell aperture, which can, in theory, bring the density downstream to a high enough level, that Chi predicted we could see a significant effect. However, we just don't have enough 399 nm laser power for that. We tried using three retro-reflecting mirrors to perform the 2-D cooling with a single 399 nm ECDL, but the laser was completely absorbed on the first pass through the atom beam. The situation is similar for the 396 nm laser—having a higher power and narrow Rydberg laser would bring up the Rydberg atom density much higher.

Hence, the conclusion of our initial tests of this exciting idea is that we need a higher density of Rydberg atoms to see a significant effect on the molecules. For the next step, we will use lasers with higher performance to 2-D cool the atoms and excite them to Rydberg states, achieving at least 2 orders of magnitude improvement in Rydberg atom density, which in theory will be sufficient for seeing significant effects on the molecules.

Chapter 4

OPTICAL CYCLING IN POLYATOMIC MOLECULES WITH COMPLEX HYPERFINE STRUCTURE

Most of this chapter is adapted from a paper I authored and published in Physical Review A [37].
Y. Zeng, A. Jadbabaie, A. N. Patel, P. Yu, T. C. Steimle, and N. R. Hutzler, "Optical cycling in polyatomic molecules with complex hyperfine structure", Phys. Rev. A108, 012813 (2023) 10.1103/PhysRevA.108.012813

4.1 Introduction

One of the first requirements for controlling molecules with lasers is photon cycling. After all, a single photon only carries so much momentum or information. For laser cooling and trapping, typically more than 10000 photons are required. That is still a faraway target for ^{173}YbOH to reach, because of its complex hyperfine structures. Here I present our work on dealing with these hyperfine structures in a scalable method that can be replicated on all the vibration repumps. However, even without the vibration repumps, this method alone will be able to improve the signal of future nMQM measurements by an order of magnitude.

Recent advances in the cooling and trapping of increasingly complex molecules [43, 44] are enabling a multitude of applications that leverage molecular complexity for applications in quantum science and precision measurement [21, 27, 45–47]. One avenue for increased complexity is the use of molecules with a heavy nucleus and non-zero nuclear spin, I. Precision measurements with these molecules can probe new physics related to the nucleus, such as charge-parity (CP) violating nuclear moments [27], nuclear-spin-dependent parity violation (NSD-PV) [48, 49], and measurements of nuclear structure [50, 51].

One example is the odd isotopologues of the linear polyatomic molecule YbOH, which are promising candidates for probing symmetry-violating physics in the hadronic sector: ^{171}YbOH for parity violation [52], and ^{173}YbOH for the CP-violating nuclear magnetic quadrupole moment (NMQM) [19, 53]. Interactions of core-penetrating valence electrons with the heavy Yb nucleus enhance sensitivity to symmetry violation [54, 55], and the quadrupole shape deformation of the Yb

nucleus provides further collective enhancement of CP-violating moments [19]. Additionally, the vibrational bending mode of YbOH exhibits closely spaced, opposite parity levels. These parity doublets allow for control of molecular polarization in modest electric fields [30], suppression of systematic errors in precision measurements [53, 56, 57], and can be tuned even closer to degeneracy by modest magnetic fields, enhancing sensitivity to NSD-PV [52]. Bending modes are one example of parity doublet structures that are generic to polyatomic molecules, and which exist independently of the electronic structure, thereby enabling their combination with efficient optical cycling and laser cooling [21, 53, 58–60].

The additional complexity of polyatomic molecules presents both opportunities and challenges. In particular, the increased number of vibrationally excited states in the electronic ground state provides many pathways for spontaneous decay after optical excitation. Molecules that decay to "dark states" not addressed by repumping lasers are lost from the optical cycle [43, 61]. Addressing rotational and vibrational branching to dark states has enabled laser cooling and trapping of both diatomic and polyatomic molecules [28, 43]. However, eliminating dark states in species with large and complicated hyperfine structures, which is a byproduct of many molecules with spin on a heavy nucleus, poses additional challenges [62]. For example, in the same rotational manifold, ^{174}YbOH has 12 Zeeman sub-levels, and ^{173}YbOH has 72. In particular, hyperfine splittings will have a multiplicative effect on the number of existing rotational and vibrational dark states, with frequency splittings large enough such that bridging with acousto-optical or electro-optical modulators becomes a challenge.

In this manuscript, we report the design and experimental realization of a scheme for achieving rotationally closed cycling of ^{171}YbOH ($I_{\mathrm{Yb}} = 1/2$) and ^{173}YbOH ($I_{\mathrm{Yb}} = 5/2$). With only two modulation frequencies on a single laser, we achieve photon cycling with closure of rotational, spin-rotational, and hyperfine structures. Furthermore, such a scheme should be broadly applicable to other molecules with similar structures, especially with the implementation of additional techniques, such as computer-generated holography [63].

4.2 Branching ratio calculation

In this manuscript, we address the branching of spontaneous decays $\tilde{A}^2\Pi_{1/2}(0,0,0) \rightsquigarrow \tilde{X}^2\Sigma^+(0,0,0)$. Here $\tilde{A}^2\Pi_{1/2}(0,0,0)$ is the vibrational ground state of the excited electronic state $\tilde{A}^2\Pi_{1/2}$, and $\tilde{X}^2\Sigma^+(0,0,0)$ is the vibrational ground state of the ground

electronic state $\tilde{X}^2\Sigma$. We will often refer to the states as simply "A" and "X," respectively, and if the vibrational quantum numbers ($\nu_{\text{Yb–O stretch}}$, ν_{bend}, $\nu_{\text{O–H stretch}}$) are omitted, it is assumed that we mean the ground vibrational state $(0, 0, 0)$. The vibrational branching ratio of $A \rightsquigarrow X$ decay has been previously measured [60] to be 89.44(61)%. Here, we are primarily concerned with the rotational, spin-rotational, and hyperfine branching, which are significantly more complicated in laser-coolable species with non-zero nuclear spins on the metal and the ligand [62].

The branching ratios are calculated using effective Hamiltonians [31]. The energies and eigenvectors within the X and A states are obtained by diagonalizing Hamiltonian matrices in the Hund's case (a) basis, and then transition dipole moments (TDMs) are calculated between the eigenvectors of the two states. For simplicity, the hydrogen nuclear spin from -OH was not included in the basis set, as the hyperfine splitting is not optically resolved [64]. However, we must remember that it is present when calculating level degeneracies.

The effective Hamiltonians used for the two states are [18]:

$$H_X^{\text{eff}} = B\boldsymbol{N}^2 + \gamma \boldsymbol{N}\cdot\boldsymbol{S} + b_F \boldsymbol{I}\cdot\boldsymbol{S} + c(I_z S_z - \frac{1}{3}\boldsymbol{I}\cdot\boldsymbol{S}) + e^2 Q q_0 \frac{3I_z^2 - \boldsymbol{I}^2}{4\boldsymbol{I}(2\boldsymbol{I}-1)}, \quad (4.1)$$

$$\begin{aligned} H_A^{\text{eff}} = {} & AL_zS_z + B\boldsymbol{N}^2 + \frac{1}{2}(p+2q)(J_-S_-e^{+2i\phi} + J_+S_+e^{-2i\phi}) \\ & + h_{1/2}I_zL_z - \frac{1}{2}d(S_+I_+e^{-2i\phi} + S_-I_-e^{+2i\phi}) + e^2Qq_0\frac{3I_z^2 - \boldsymbol{I}^2}{4\boldsymbol{I}(2\boldsymbol{I}-1)}. \end{aligned} \quad (4.2)$$

Here, $\boldsymbol{S}$ is the Yb-centered electron spin, $\boldsymbol{I}$ is the Yb nuclear spin, and $\boldsymbol{N}$ is the total non-spin angular momentum. All angular momentum subscripts $(z, \pm)$ denote molecule frame components. Spin-orbit A, rotation B, spin-rotation γ, and Λ-doubling $(p + 2q)$ are present in all isotopologues. Both ^{171}Yb($I = 1/2$) and ^{173}Yb($I = 5/2$) have nuclear spins, which give rise to additional hyperfine parameters, namely orbital hyperfine a, Fermi contact b_F, spin-dipolar c, and parity-dependent dipolar d. In the excited state, the diagonal hyperfine shifts are determined by an effective parameter $h_{1/2}$, which can be written as $h_{1/2} = a - (\frac{b_F}{2} + \frac{c}{3})$ [18]. Further, ^{173}Yb also has an electric quadrupole moment, which gives rise to the term e^2Qq_0. The exact parameter values used are taken from ref. [18] and listed in table 4.1.

After diagonalizing the Hamiltonians, the eigenvectors are labeled according to the Hund's cases that best represent their structure: Hund's case ($b_{\beta S}$) for X, and Hund's case ($a_{\beta J}$) for A [18]. The labels are simplified to include only the quantum numbers relevant to this manuscript: $|NGF\rangle$ for the X state and $|J(P)F\rangle$ for the A state. Here, for the X state $\boldsymbol{G} = \boldsymbol{I} + \boldsymbol{S}$ results from the hyperfine interaction between $\boldsymbol{I}$ and $\boldsymbol{S}$, while for the A state $\boldsymbol{J}$ results from both molecule rotation and spin-orbit coupling, and (P) is the parity label for the parity doublets resulting from Λ-doubling. The total angular momentum $\boldsymbol{F}$ is given by $\boldsymbol{F} = \boldsymbol{G} + \boldsymbol{N}$ in the X state and $\boldsymbol{F} = \boldsymbol{J} + \boldsymbol{I}$ in the A state. We will use double primes to denote ground state quantum numbers (e.g. N'') and single primes to denote excited state quantum numbers (e.g. J').

TDMs are calculated between the eigenvectors by representing all states in the Hund's case (a) basis and performing computations only in this basis. Case (b) quantum numbers labels N'', G'' are assigned to the ground state eigenvectors by identifying patterns in the eigenvalues. To obtain branching ratios and account for the degeneracy of M_F sublevels, the TDMs are summed over light polarization p and ground state M_F'' levels and averaged over excited state M_F' levels. We obtain:

$$\frac{1}{2F'+1} \sum_{p, M_F'', M_F'} \langle N'' G'' F'' | \, T_p^1(d) \, | J'(P) F' \rangle \, . \tag{4.3}$$

This way, the branching ratio derived by squaring the TDM is naturally normalized, which means that the branching ratios originating from the same excited state add up to 1. Note that we use the same reduced matrix element convention as ref. [31].

State	Parameter	^{171}YbOH	^{173}YbOH
$\tilde{X}^2\Sigma^+(0,0,0)$	B	0.245	0.245
	γ	−0.00270	−0.00270
	b_F	0.228	−0.0628
	c	0.0078	−0.00273
	e^2Qq_0	N/A	−0.111
$\tilde{A}^2\Pi_{1/2}(0,0,0)$	A	1350	1350
	B	0.253	0.253
	$p + 2q$	−0.439	−0.438
	$h_{1/2}$	0.0148	−0.00422
	d	0.0320	−0.00873
	e^2Qq_0	N/A	−0.0642

Table 4.1: Relevant parameters, from [18], in wavenumbers (cm^{-1}) for the $\tilde{X}^2\Sigma^+(0,0,0)$ and $\tilde{A}^2\Pi_{1/2}(0,0,0)$ states of ^{171}YbOH and ^{173}YbOH.

The calculated branching ratios are shown in Figure 4.1. Note that these branching ratio numbers add up to 1 only within the same vibration level, and they will be referred to as rotational branching ratios. The total branching ratio of a transition can be derived by multiplying the rotational branching ratio by the vibrational branching ratio, which is known for ^{174}YbOH [60], and expected to be the same for ^{171,173}YbOH.

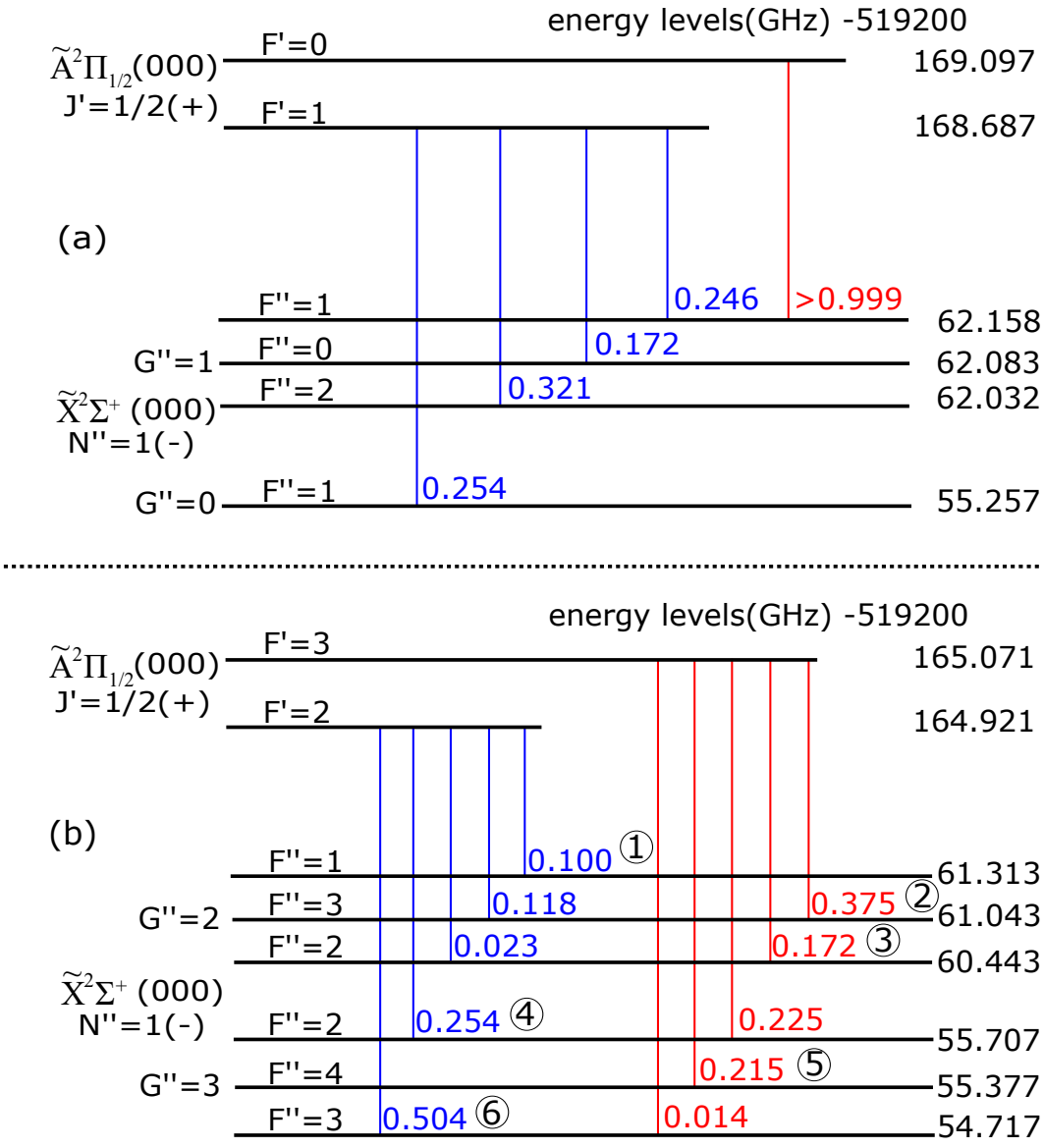

Figure 4.1: Calculated rotational branching ratios for (a) ^{171}YbOH and (b) ^{173}YbOH. Numbers 1-6 in circles label the transitions targeted for achieving rotationally closed cycling.

4.3 Method for achieving rotationally closed cycling

We achieve rotationally-closed optical cycling via $N'' = 1 \rightarrow N' = 0$ type transitions [65], specifically $N'' = 1 \rightarrow J' = 1/2(+)$ for YbOH (since N' is not well-defined in A, $J' = 1/2$ corresponds to the lowest rotational level in A). Based on our calculations, rotationally closed cycling is straightforward to achieve for ^{171}YbOH because there is a single transition, $F'' = 1 \rightarrow F' = 0$, with a calculated rotational branching ratio of > 0.999. The excited hyperfine splitting of ~400 MHz is sufficiently large, compared to the observed linewidths of ~50 MHz , such that off-resonant excitation to $F' = 1$ can be avoided, which is not the case in ^{173}YbOH. The experimental linewidth is larger than the radiative width of ~10 MHz mostly due to power broadening, and is beneficial for addressing all the sidebands for ^{173}YbOH.

In order to fully address rotational branching for ^{173}YbOH, we must address all 6 ground hyperfine levels, as the excited $F' = 2$ and $F' = 3$ states are separated by ~150 MHz, which can result in off-resonant excitation when slightly power-broadened. We address the ground levels by generating sidebands on a single laser using two fiber electro-optical modulators (EOM) used in series[1]. Fortunately, the transitions are spaced such that it is possible to use only two EOMs, each with a single sinusoidal drive, to address all of the transitions within the slightly power-broadened linewidth, as shown in Fig. 4.2.

The two EOMs are used sequentially with input from an 1154 nm seed laser, and the output is then amplified and doubled to produce the needed visible light at 577 nm. Extra, unwanted sidebands are produced from both the EOMs and the doubling crystal, and the latter also modifies the sidebands due to the non-linear nature of second harmonic generation. These sidebands can accidentally drive undesirable transitions that cause leakage by optically pumping $N'' = 1$ population into rotational dark states within the same vibrational manifold.

Here, we were able to avoid leakage-inducing transitions by using modulation frequencies set such that the three intense, unused sidebands, as well as smaller, higher-order sidebands, are sufficiently far away from unwanted transitions, as shown in Fig. 4.2. Specifically, one EOM is driven at 5.63 GHz and the other 495 MHz, with a modulation depth of around $0.5V_\pi$, chosen such that the end output matches the patterns shown in Fig. 4.2. Note, however, that the complex and congested spectrum [18] of these molecules means that off-resonant excitation of unwanted lines cannot be ignored, and our method takes them into account when calculating the number

[1] EOSPACE PM-0S5-10-PFA-PFA-1154-UL-SOP125mW

of scattered photons. These problems can be alleviated using other techniques, such as computer-generated holography [63].

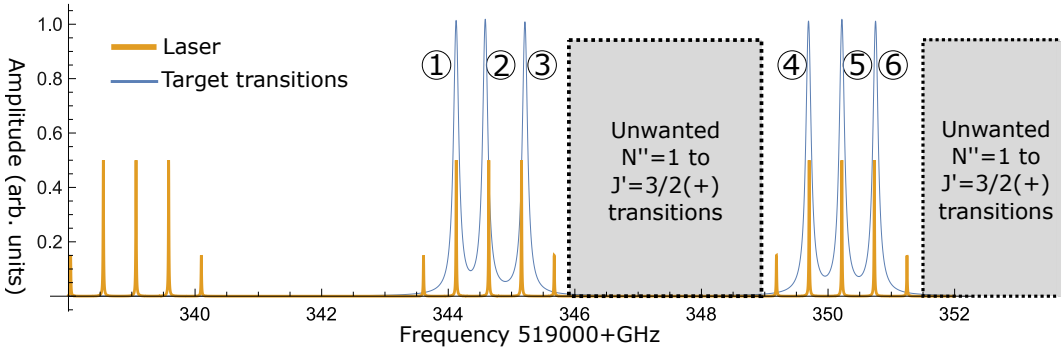

Figure 4.2: Scheme for EOMs to address ^{173}YbOH branching. Blue (thin) lines are the target transitions we want to address. From left to right they correspond to transitions in Fig. 4.1(b) labeled 1-6. Yellow (thick) lines are generated by the pump laser and EOMs, which reflect the frequency spacings and relative amplitudes of the sidebands generated EOMs as verified by using a Fabry-Perot cavity. As shown, the scheme used can address all the target transitions within their linewidths while avoiding the unwanted lines that can cause leakage to dark states.

4.4 Measuring the number of scattered photons

We experimentally study optical cycling using a cryogenic buffer gas beam (CBGB) [33] of YbOH. We create cold, slow beams of YbOH using methods similar to those described elsewhere [18, 30, 34]. We use a ~1.5 K cell with 2 SCCM flow of helium buffer gas and enhance the production of YbOH using optically-driven chemical reactions [34]. We use CW lasers to scatter photons, and the resulting laser-induced fluorescence is monitored with photo-multiplier tubes (PMTs).

To verify that we have achieved rotational closure, we optically cycle and measure the number of photons scattered per molecule. If we have addressed all branching within X, the molecules will cycle until they are optically pumped into a dark vibrational state. The majority of molecules are pumped into one of the hyperfine levels of the $\tilde{X}^2\Sigma^+(1,0,0)$ state with one quantum of Yb-O stretching motion ($v=1$), which has a branching ratio of 9.11(55)% from A. After cycling upstream in the molecular beam, we measure the population downstream in one of the hyperfine levels of the $v''=1$ state (see fig. 4.3).

The main benefit of such a population transfer measurement, compared to a direct fluorescence measurement of optical cycling, is the ability to reject accidental fluorescence from nearby transitions. There are 5 isotopes of Yb with significant

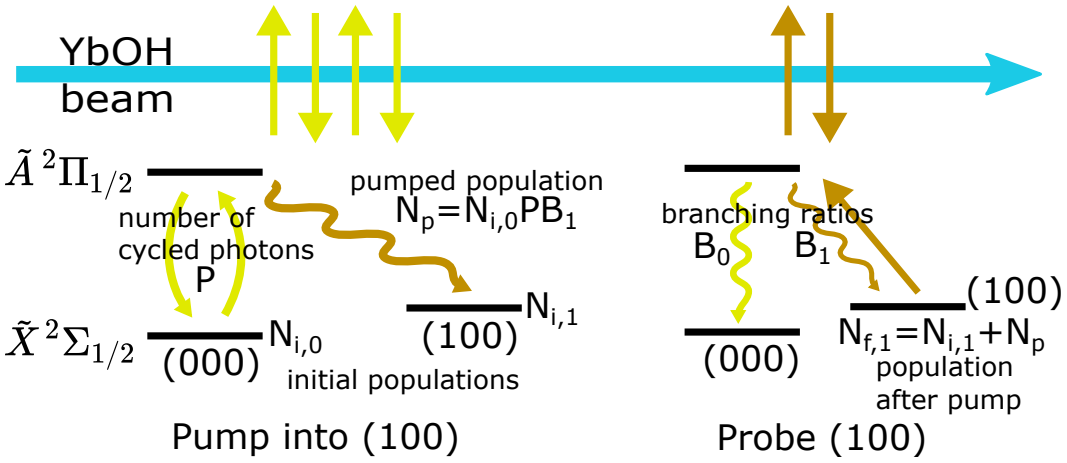

Figure 4.3: Schematic for measuring the number of photons cycled by measuring the population transfer into one of the hyperfine levels of the first excited vibration state (1,0,0), or alternatively labeled $v = 1$. We derive the number of cycled photons by comparing the probe fluorescence with the cycling pump and non-cycling pump.

abundance, and both ^{171,173}YbOH have extra complexity arising from their nuclear spins. As a result, the band head region where the cycling transitions are located is extremely congested with additional lines, and a direct fluorescence measurement would make it difficult to disentangle the effects of photon cycling versus merely addressing multiple lines in different states and isotopologues.

By using a pump-probe scheme to measure the population transfer, most of these unwanted transitions do not contribute to our results. The exception is when both pump and probe coincide with optical pumping of a different isotopologue or level that is unrelated to cycling. By using both resonant chemical enhancement [34] of a specific Yb isotope and intentional selection of the hyperfine level in $v'' = 1$ for the probe transition, contaminant contributions to optical pumping are relatively small, and can be estimated using detunings and branching ratios.

Our figure of merit is the quantity D, defined as the difference in $v'' = 1$ probe fluorescence caused by the cycling pump laser, normalized against probe that we use the same reduced matrixfluorescence without the pump. Because the $v'' = 1 \rightarrow v' = 0$ probe transition has a very small branching ratio of 0.0911, we operate with a low saturation parameter, and the measurement of fluorescence increase is equivalent to an increase in population. To extract the number of photons cycled from D, we use the following relationship:

$$D = \frac{\text{fluorescence}_{\text{pump}} - \text{fluorescence}_{\text{no pump}}}{\text{fluorescence}_{\text{no pump}}} \approx \frac{N_{f,1} - N_{i,1}}{N_{i,1}} = \frac{N_P}{N_{i,1}} \approx \frac{N_{i,0} \cdot P \cdot B_1}{N_{i,1}}, \tag{4.4}$$

where N_P is the population transferred into $v'' = 1$ from optical pumping, $N_{i,1}$ is the initial population of the $v'' = 1$ state being probed, $N_{i,0}$ is the initial population of the $v'' = 0$ states being pumped, $P \approx 1/(1 - B_0)$ is the number of photons cycled per pumped molecule, B_0 is the sum of total branching ratios of all the pumped states in $v'' = 0$, and B_1 is the branching ratio down to the specific hyperfine state probed in $v'' = 1$ probe state (see Fig. 4.3.)

The ratio $N_{i,0}/N_{i,1}$ can be calculated from measurements by making two assumptions about the initial populations of the relevant states: first, that the states within a vibrational manifold are well thermalized coming out of the cryogenic buffer gas beam source, and second, that the ratios of population between vibration ground and first excited vibration mode, $R = N_{total(v=1)}/N_{total(v=0)}$, is the same for different isotopologues of YbOH under the same source condition. These assumptions are supported by tests done with ^{174}YbOH and from behavior in other such molecular sources [33].

4.5 Calibration with ^{174}YbOH

We first made measurements with ^{174}YbOH to validate our method, since photon cycling in ^{174}YbOH has been carefully characterized elsewhere [60], as well as to derive the population ratio R between the vibrational modes in our molecular beam. Results are shown in Fig. 4.4, which gives two final D values for two different pumping laser configurations: D_{ro} for rotationally open (ro) pumping, and D_{rc} for rotationally closed (rc) pumping. For ^{174}YbOH, we only need one sideband to cover the spin-rotation splitting and achieve rotationally closed cycling [59], which gives a scattered photon number of about $P \approx 1/(1 - B_0) = 9.1$ per addressed molecule, limited only by the vibrational branching ratio $B_0 = 0.89$. In comparison, when only addressing the $J = 1/2$ state of the spin-rotation pair, which has a rotational branching of 0.67, the photon number expected is only $P = 2.5$, where $B_0 = 0.89 \times 0.67 = 0.60$.

With the assumption of thermalization, we can treat all rotational levels and M_F sublevels within a given vibronic manifold as having equal initial population since the level splittings are all far smaller than the thermal energy $k_B T \approx 30$ GHz, where k_B is Boltzmann's constant and our operating temperature is $T \approx 1.5$ K. Let

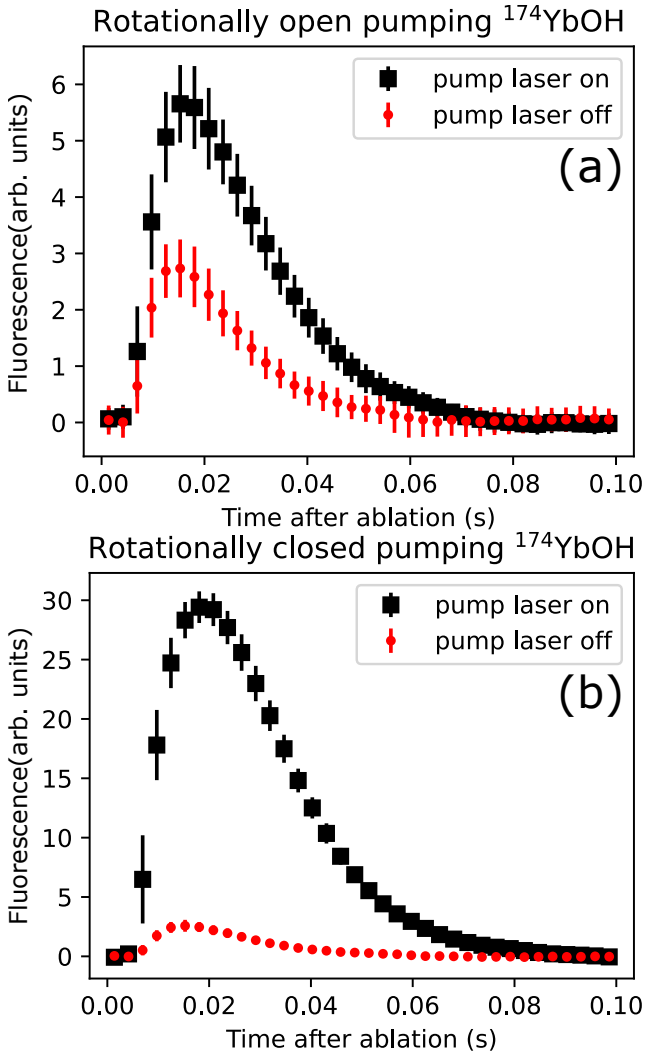

Figure 4.4: ^{174}YbOH fluorescence signals from a probe laser addressing the $v''=1$ $N''=1$ $J''=1/2$ state. Error bars represent 1-σ variation due to shot-to-shot fluctuations over 80 beam pulses. (a) The pump laser has no sidebands and only addresses the $J''=1/2$ state in the ground spin-rotation pair. The increase in fluorescence is a factor of $D_{ro}=1.38\pm0.23$, as described in the main text. (b) The pump laser addresses both $J''=1/2$ and $J''=3/2$, achieving rotationally closed cycling and increasing the fluorescence by $D_{rc}=15.0\pm1.6$.

the initial population of the pumped state be the degeneracy of the state times 1 (including hydrogen nuclear spin). For ^{174}YbOH, The initial population is $N_{i,0}=12$ for addressing both of the spin-rotation (SR) pair and $N_{i,0}=4$ for addressing only the $J''=1/2$ state of the pair. Then, using $R=N_{total(v=1)}/N_{total(v=0)}$ as an unknown variable, we have the initial population of the probed state as $N_{i,1}=4R$. Here the probe laser addresses the $v''=1, N''=1, J''=1/2$ state, which has a total branching

ratio of $B_1 = 0.06$ coming from $J' = 1/2(+)$ excited state.

As a result, when the pump addresses both components of the SR pair, we would expect the measurement to be $D_{rc} = N_{i,0} P B_1 / N_{i,1} = 1.64/R$. Similarly, when the pump addresses only the $J'' = 1/2$ state, we expect $D_{ro} = 0.15/R$. Experimentally, we measured D to be $D_{rc} = 15.0 \pm 1.6$, and $D_{ro} = 1.38 \pm 0.23$, which gives R values of 0.11 ± 0.01 and 0.11 ± 0.02. In other words, the $v'' = 1$ manifold has approximately 11% of the population of the v'' =0 manifold. The results are averaged from 40 data sets, where the statistical uncertainties mainly come from shot-to-shot variations of the molecule source. The two different pumping configurations give the same R value within our error, validating the measurement method. For the measurements on ^{171,173}YbOH, we will similarly perform both rotationally closed and open pumping but will use the $R = 0.11$ as a known parameter to derive the number of scattered photons per molecule.

4.6 Spectroscopy of ^{171,173}YbOH $\tilde{X}^2\Sigma^+(1,0,0)$

In order to measure the population transfer from optical pumping, it is important to establish the correct quantum numbers and energies for the $\tilde{X}^2\Sigma^+(1,0,0)$, or $v'' = 1$, states within the $N'' = 1$ manifold for ^{171,173}YbOH. Given the known odd and even isotopologue parameters for the $v'' = 0$ state [18, 64], and the even isotopologue parameters for the $v'' = 1$ state [36], we first predict the expected spectral region for the $\tilde{X}^2\Sigma^+(1,0,0) \rightarrow \tilde{A}^2\Pi_{1/2}(0,0,0)$ transition. We then measure spectra around the predicted region and look for splittings that match the known excited splittings between hyperfine levels of $\tilde{A}^2\Pi_{1/2}(0,0,0)$ $J = 1/2(+)$ and $J = 3/2(+)$. For transitions with a shared ground state and different excited states, the observed line splittings will match the known structure of the excited $\tilde{A}^2\Pi_{1/2}(0,0,0)$ state [18].

The spectral region is congested with overlapping transitions from multiple rotational and hyperfine states, as well as from other isotopologues. Furthermore, the $v = 1$ states have an order of magnitude smaller population coming out of the cryogenic buffer gas source compared to $v = 0$, as we learned from the ^{174}YbOH measurements in the previous section. In order to differentiate the multiple transitions, we used chemical enhancement [34] and population pumping from $v = 0$.

As an example, fig. 4.5 shows four transitions from the $X, v'' = 1, N'' = 1, G'' = 1, F'' = 1$ ground state to four hyperfine levels in the excited $A, v' = 0, J' = 1/2$ and $J' = 3/2$ states. The spectrum in Fig. 4.5(b) is taken downstream of a power-broadened pumping laser with EOM-generated sidebands that roughly addresses all the $v'' = 0$, $N'' = 1$

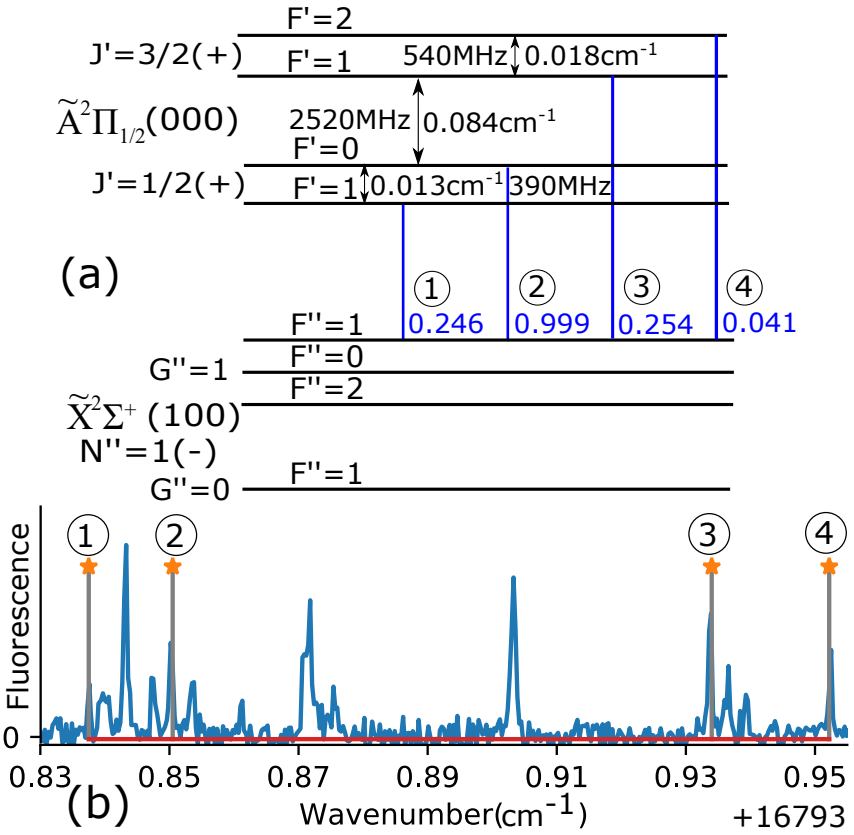

Figure 4.5: Example of $v'' = 1$ spectroscopy for ^{171}YbOH. Transitions are identified by matching spectral splittings to known excited state splittings [18]. (a) is the level diagram of the involved ground and excited states, with calculated branching ratios for the target transitions. (b) is the measured fluorescence spectrum with the same four transitions marked in (a). Some of the unmarked peaks nearby are transitions from $F'' = 0, 2$ ground hyperfine levels to the same excited states, identifiable via the common splittings.

ground states connected to the $J' = 1/2(+)$, $F' = 1$ excited state. The EOM sideband scheme is not optimized here because we need initial spectroscopy to confirm our probe state selection. After the prerequisite spectroscopy, we are able to optimize the sideband scheme to achieve rotationally closed photon cycling.

A full spectroscopic analysis and parameter fit for all the $v = 1$ states is beyond the scope of this work. However, we were able to identify all of the relevant hyperfine levels within the $v'' = 1$, $N'' = 1$ manifold for ^{171,173}YbOH (see supplement). We are confident in our state identification based on the matching splittings in both ground and excited states, and based on the observation of expected population transfers.

4.7 Photon cycling in ^{171,173}YbOH

After identifying all of the $v''=1$, $N''=1$ states for both ^{171,173}YbOH, we decided to use the $\tilde{X}^2\Sigma^+(1,0,0)\,|N''=1, G''=1, F''=1\rangle \rightarrow \tilde{A}^2\Pi_{1/2}(0,0,0)\,|J'=1/2(+), F'=0\rangle$ transition for the ^{171}YbOH probe, since it is the rotationally-closed analogue of the corresponding $(0,0,0) \rightarrow (0,0,0)$ transition, and relatively well separated from other hyperfine levels. For ^{173}YbOH, we decided to use the $\tilde{X}^2\Sigma^+(1,0,0)\,|1,3,2\rangle \rightarrow \tilde{A}^2\Pi_{1/2}(0,0,0)\,|1/2(+),2\rangle$ transition, as it minimized accidental pump/probe signal contaminants from unwanted states, and since it has very similar branching from both excited F' hyperfine levels, simplifying data analysis and modeling. With the probe transitions identified, we were able to optimize the cycling schemes and lower the pump laser power required to less than 25 mW per sideband in a 5 mm diameter beam.

Following the same procedure used for ^{174}YbOH laid out in the previous section, we measured the scattered photon number per molecule for ^{171}YbOH and ^{173}YbOH to confirm that our cycling schemes work as expected. Fig. 4.6 shows the results for ^{171}YbOH. The rotationally closed cycling transition is from $F''=1$ to $F'=0$, which gives an initial population, including unresolved -OH hyperfine degeneracy, of $N_{i,0}=6$. The pump transition for the rotationally open comparison is from the same ground state, hence the same initial population, but a different excited state, $F'=1$, which gives a calculated branching ratio of $B_0=0.22$. The probe transition addresses the equivalent ground state in $v''=1$, so $N_{i,1}=6R$, and the total branching ratio from A to $v''=1$ is $B_1=0.09$ from $F'=0$ and $B_1=0.02$ from $F'=1$.

Fig. 4.6(a) shows results from pumping on the rotationally open transition, which gives an increase in fluorescence of $D_{ro}=0.48\pm0.17$. Using the value $R=0.11\pm0.01$ from ^{174}YbOH, we obtain a photon number of 2.4 ± 0.8, which is larger than the 1.3 expected from a branching ratio of 0.22. The reason for the discrepancy is the contribution from nearby $v''=1$ ground state hyperfine levels which are 80 and 150 MHz away. The nearby levels contribute both to the initial population $N_{i,0}$ and to the branching ratio B_0. By calculating and including the effect of photon scattering from these nearby states, we actually expect a fluorescence increase of $D_{ro}=0.45$, which fits the data well and thus confirms that the assumption holds that the vibrational population ratio R is isotope independent. For the rotationally closed transition, we measured a fluorescence increase $D_{rc}=7.4\pm1.3$, which gives a scattered photon number of 8.9 ± 1.5, which matches the expectation of 9.1 from the vibrational branching ratio of 0.89.

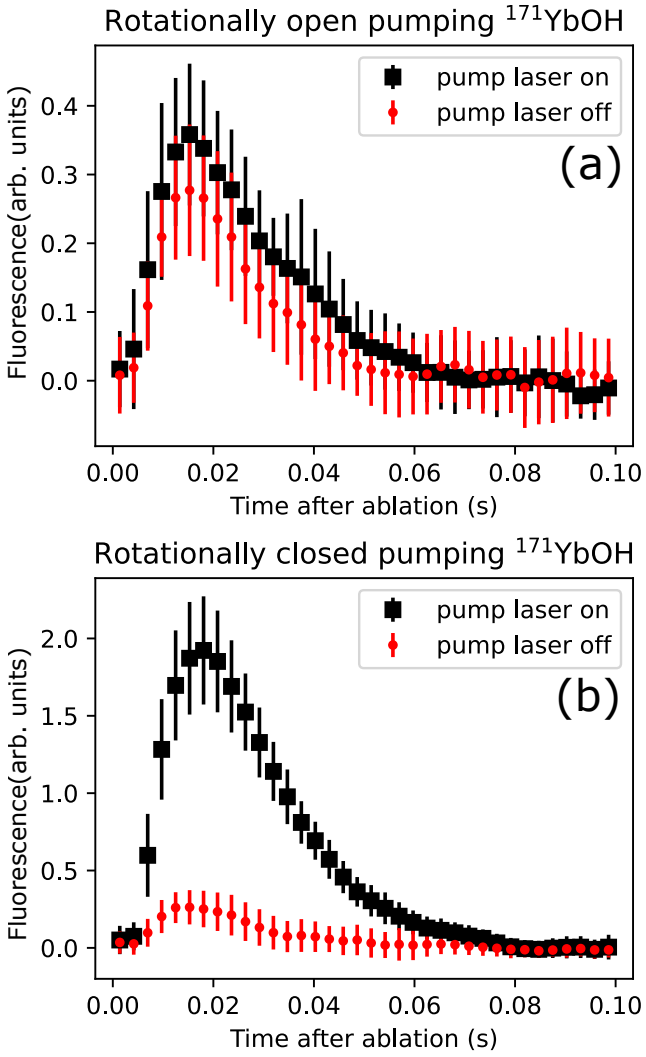

Figure 4.6: ^{171}YbOH fluorescence signals from the probe laser addressing $v''=1$ $|N''=1, G''=1, F''=1\rangle$. Error bars represent 1σ spreads due to shot-to-shot fluctuations over 80 beam pulses. (a) Pump laser addressing the $F''=1 \rightarrow F'=1$ rotationally open transition. The increase in fluorescence is $D_{ro}=0.48\pm0.17$. (b) Pump laser addressing the $F''=1 \rightarrow F'=0$ rotationally closed cycling transition. The fluorescence increase is $D_{rc}=7.4\pm1.3$.

Fig. 4.7 shows results for ^{173}YbOH. The reference pump transition addressing $F''=3$ has $N_{i,0}=14$, and a branching ratio of $B_1=0.02$ to the probe state in $v''=1$. The cycling pump addresses all 6 ground hyperfine levels, giving $N_{i,0}=72$, and the same branching ratio to the probe state. The probe laser addresses $F''=2$, giving $N_{i,1}=10R$. With the same $R=0.11$ value as before, the measured normalized difference in fluorescence, $D_{ro}=0.40\pm0.14$, means that the reference pump scattered $P=1.4\pm0.5$ photons per molecule, matching the expectation of 1.5 for the

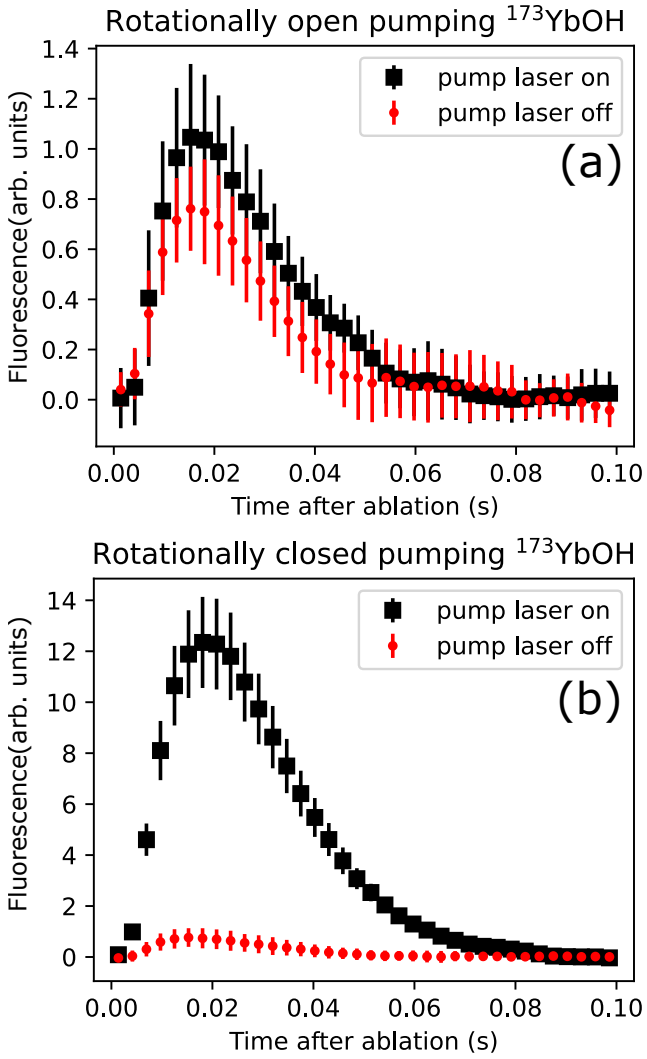

Figure 4.7: ^{173}YbOH fluorescence signals from probe laser addressing $v''=1$ $|N''=1, G''=3, F''=2\rangle$. Error bars represent 1σ spreads due to shot-to-shot fluctuations over 80 beam pulses. (a) Pump laser with no sidebands, addressing only the $|1,2,3\rangle \rightarrow F'=3$ transition. The change in integrated fluorescence is $D_{ro}=0.40\pm0.14$. (b) The pump laser addresses all the $v''=0, N''=1$ hyperfine levels using the optimized EOM scheme, and thus achieves rotationally closed cycling. The increase in fluorescence is $D_{rc}=13.0\pm1.9$.

branching ratio of $B_0=0.33$ on the open transition. For rotationally closed cycling, the result of $D_{rc}=13.0\pm1.9$ would indicate a photon number of 9.1 ± 1.3, matching the expected 9.1 from purely vibrational branching. Note that there is an expected rotational leakage of 0.5% due to hyperfine-induced transitions [18], which is below our resolution to observe; however, this could be addressed by adding additional sidebands to address the relevant $N''=3$ levels.

Table 4.2 summarizes the result of our photon cycling measurements. Our measured results for the number of photons scattered per molecule, P, are in good agreement with the expectation from our calculated branching ratios. In particular, once rotational branching is addressed, the value of P is limited by vibrational branching, which is independent of isotopologue. This is also reflected in our data, with each isotopologue having the same value of P for rotationally closed pumping.

Molecule	RO/RC	Expected P	Measured P
^{174}YbOH	RO	2.5	
	RC	9.1	
^{171}YbOH	RO	1.3	2.4 ± 0.8
	RC	9.1	8.9 ± 1.5
^{173}YbOH	RO	1.5	1.4 ± 0.5
	RC	9.1	9.1 ± 1.3

Table 4.2: A comparison of expected and measured numbers of photons scattered per molecule, denoted as P. Here, RO refers to rotationally open pumping, and RC refers to rotationally closed pumping. Measurements of P in ^{174}YbOH are used, along with the theoretical prediction, to derive the vibration population ratio R. Both RO and RC for ^{174}YbOH yielded the same resulting R. The high P measured in RO ^{171}YbOH is caused by nearby ground hyperfine levels contributing.

4.8 Conclusion

We have demonstrated a scheme that achieves rotationally closed photon cycling of ^{171}YbOH and ^{173}YbOH, both of which have complicated hyperfine structures. The method is technically straightforward and can be easily extended to higher-order vibrational repumps to enable larger numbers of scattered photons. Since molecule-based studies of the nuclear weak force and the search for CP-violating nuclear magnetic quadrupole moments require species with significant electron density at a heavy, spinful nucleus, the ability to address the resulting complicated hyperfine structure will be important for future experimental searches. Photon cycling will enable significant increases in efficiency of state preparation and detection [66, 67] for ongoing experiments using ^{173}YbOH [18, 57], and will be a critical ingredient of future improvements involving laser cooling to perform next-generation beam [68] or trap [53] measurements of this or other laser-coolable molecular species with complex hyperfine structure due to large nuclear spins.

Acknowledgments

We acknowledge helpful discussions with Nickolas Pilgram. This work was supported by the Gordon and Betty Moore Foundation (GBMF7947), the Alfred P. Sloan Foundation (G-2019-12502), the Heising-Simons Foundation (2019-1193 and 2022-3361), and an NSF CAREER award (PHY-1847550).

Chapter 5

NON-RESONANT CAVITY FOR INTENSITY BUILDUP OF MULTIPLE LASERS

Most of this chapter is adapted from a paper I authored and published in Applied Optics [69].
Y. Zeng and N. R. Hutzler, "Nonresonant cavity for multipass laser intensity buildup", Appl. Opt. 62, 3574–3580 (2023) 10.1364/AO.487531

5.1 Introduction

While we have a road map towards laser cooling and trapping of complex molecules, it is still a huge technical challenge involving the use and maintenance of high performance lasers numbered in tens or even twenties, depending on the molecule. Most of these lasers are repump lasers. When molecules decay from excited states, they will end up in many different rotational and vibrational states. Repump lasers make sure that most molecules will return to one singular ground state such that photons can be continuously cycled. Many of these transitions are separated far apart enough, such that they can not be bridged using modulators, like acousto-optical modulators or electro-optical modulators.

These repump lasers usually must be co-located with the main cycling laser, whether for cooling or trapping. Most of them are $0.1 - 5$ W in power, continuous wave, and narrow linewidth ($\lesssim$MHz), with fine control over time-varying frequency, sidebands, and polarizations. The number of these lasers required for molecule experiments will increase as the structure complexity increases. For example, in order to trap CaOH molecules in a magneto-optical trap, 11 vibrational repump lasers were used [28]. The technical challenges of running a large number of high power lasers will soon become hard to manage as we pursue heavier molecules like YbOH or more complex molecules like $YbOCH_3$.

One way to ease such difficulty is to use low power lasers and build up the intensity with a power build-up cavity [70–72], where resonance is used to increase the laser power circulating in the cavity. While this technique has excellent performance, it usually requires active stabilization and can only work with a small number of lasers due to the required resonant condition. Implementing this approach with ~ 10 lasers

would be very challenging, especially since laser cooling experiments typically require multiple wavelengths, sidebands, frequency changes, multiple polarizations, etc.

We are therefore interested in non-resonant methods of building up intensity. Typically, one can use a multi-pass setup bouncing the laser beams between two or more mirrors. Such a method is generally useful if the goal is to amplify power in an extended interaction region, for example with a molecule beam [73, 74]. However, the performance is limited if high intensity and uniformity are needed in a confined region, for example, the few-mm cross-sectional area of a magneto-optical trap (MOT) [43]. In practice, it is generally difficult to have intensity increases of more than a factor of a few in such a small region.

In this chapter, we present the design and prototyping of a multipass, non-resonant, and intensity-building cavity modified from the Herriott cell [75]. Using mostly off-the-shelf parts, our test setup can achieve over an order of magnitude amplification in intensity while maintaining a uniformity comparable to that of a Gaussian beam. It is also easy to set up and tune, flexible in the size of the illumination region, and robust against perturbations. We have used the prototype cavity for enhancing fluorescence signals and for two-photon excitation of Rydberg Yb atoms.

5.2 The Herriott cell and modification

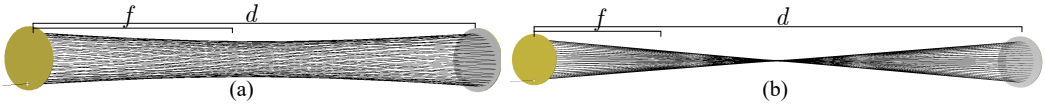

Figure 5.1: (a) Typical Herriott cell setup in a near-confocal configuration used for multi-pass absorption spectroscopy. d is the spacing between the mirrors, and f is their focal length. Figure generated using LightTools. (b) Herriott cell in a near-concentric configuration.

A Herriott cell is commonly used for multipass absorption spectroscopy [76, 77], where the cell increases the interaction path length by factors of few tens or even hundreds, as shown in Fig. 5.1(a). The only components required are two concave mirrors, with one of them having an entry hole drilled through the face, usually near the edge. For multipass absorption, the Herriott cells are usually in a configuration where the cavity length d is just slightly longer than two times the focal length $f = R/2$ of the mirrors with a radius of curvature R, that is, nearly confocal, and the laser beam will bounce back and forth tracing out a circle of dots on the mirrors

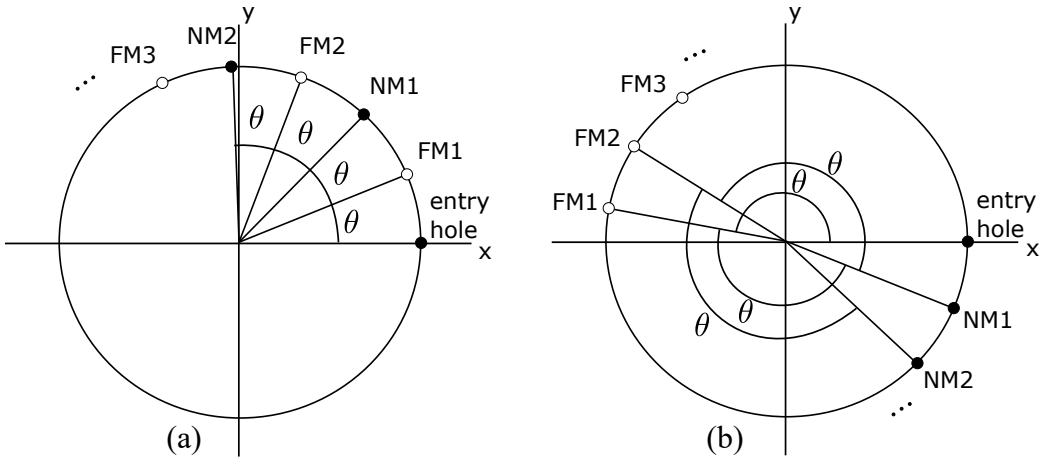

Figure 5.2: (a) Pattern of spots traced out by the reflecting laser beam on the mirrors. The solid dots are spots on the near mirror (NM), which is the one with the entry hole, and the circles are spots on the far mirror (FM). Figure adapted from ref. [76]. (b) Pattern when the cavity is at a near-concentric configuration, and the angle θ between consecutive spots is close to 180°

before exiting through the entrance hole. In such a configuration the laser beams form a near-cylindrical shape with little overlap, which is ideal for extending optical path lengths but not for building up intensity, which we aim to achieve by modifying the design. An easy first step would be to narrow the waist down by increasing the cavity length, as shown in Fig. 5.1. The angle between two consecutive reflecting points on the mirrors dictates the waist size, and its relationship to the cavity length is given by [75]

$$\cos(\theta) = 1 - \frac{d}{2f}, \tag{5.1}$$

where d is the cavity length, f is the focal length of the two mirrors, and θ is the angle between two spots on the mirrors, projected on the same plane, as shown in Fig. 5.2. As the cavity approaches the concentric configuration, d/f approaches 4 and the angle approaches 180° meaning that consecutive reflection points are on opposite sides so that the laser beams are always near the center at the middle of the cavity, as shown in Fig. 5.1(b) and Fig. 5.2(b). The intensity distribution will look like Fig. 5.3, which shows calculated cross sections of laser beam sizes and positions, on the near mirror and at the middle of the cavity. The input laser beam has to be focused at around the middle of the cavity to achieve such a "collimated" configuration, where the laser beam sizes on the same cross section appear similar to the naked eye, although in reality the beam sizes still change due to the concave

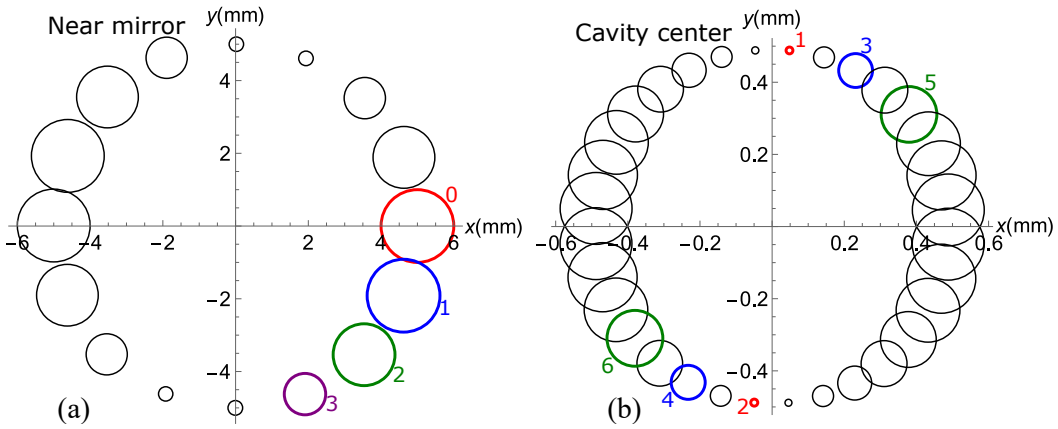

Figure 5.3: Cross sections of laser beams in a $d = 3.96f$ Herriott cell, where the spot sizes are roughly uniform, hence the "collimated" configuration. Here the circles indicate the size and position of the reflecting beam. The pattern is generated using a simple model based on ray transfer matrix analysis. (a) Intensity distribution on the near mirror. The entry spot 0, and the first three reflecting spots are labeled. (b) Intensity distribution at the middle of the cavity; note that the size scale is 10 times smaller. The first six passes are labeled.

mirrors. Note that the laser beam diameter at the cavity center is about 10 times smaller than that at the cavity mirrors.

This near-concentric configuration does not give the desired intensity buildup with uniform distribution, but we can make two further modifications to realize this goal. First, we will move the position of the entry hole closer to the mirror center compared to the typical Herriott cell; second, we will change the divergence of the input beam. As discussed in the following sections, these changes realize the goal of a fairly uniform intensity buildup.

5.3 Modeling

In order to achieve a more uniform intensity distribution, we must change the input beam divergence to increase the spot sizes. However, the stock Herriott cell mirrors used in spectroscopy usually have the entry hole very close to the mirror's edge, and we find that making the input beam more diverging results in the reflected beams leaking off the mirror edges, leading to power loss. Thus, we would like to push the holes further in. However, we also do not want the entry hole to be too close to the center because then it will limit the number of passes the cavity can accommodate. In order to determine where the entry hole should be positioned on the near mirror and in general to better understand how the laser beam behaves when bouncing

between the two concave mirrors, we implemented a simple model based on ray transfer matrix analysis [78].

From Eq. (1), we know where the laser beam landed on both the near and far mirrors for each pass, so the beam positions between the two mirrors can be calculated using simple geometry. Ray transfer matrix analysis is used for tracking the beam diameter of the Gaussian laser beam, which will change due to both free-space propagation and reflection from the curved mirror surfaces. The input laser beam diameter is represented by the input ray position and the focusing of the input laser is represented by the input ray angle.

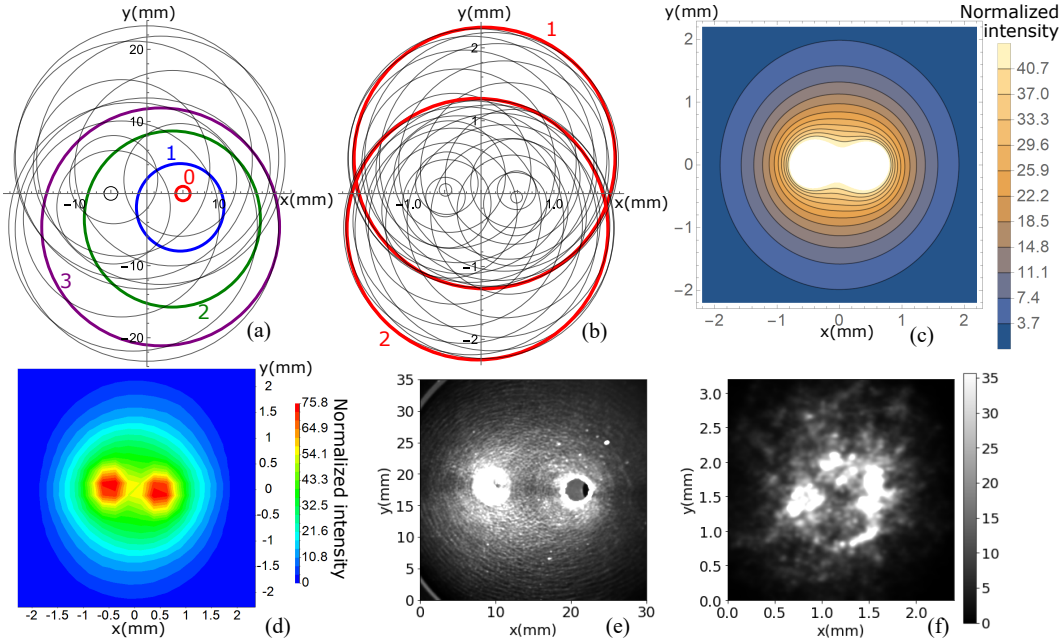

Figure 5.4: Example of a diverging configuration. Calculated cross section patterns of laser beam sizes and positions, contour plot of intensity distribution, and photos of the same configuration in a prototype setup. (a) The pattern on the near mirror. The entry spot 0, and the first three spots are labeled. (b) Pattern at the center of the cavity (size scale is 10 times smaller). The first two passes are labeled. (c) Calculated contour plot at cavity center, intensity normalized against input Gaussian beam. (d) Simulated contour plot generated from LightTools, normalized against uniform input beam. (e) Photo of the near mirror, where the bright circle on the right side is the entry hole. (f) Photo of scattered light on an AR coated window placed at cavity center, with intensity normalized against a single pass.

Combining both the location and size information, we now have a full understanding of the laser beam inside the cavity. We can make figures like fig. 5.3(a) for any cross section along the length of the cavity, and combining with a Gaussian power

distribution, we can make contour plots for intensity like fig. 5.4(c). One interesting observation worth noting is that, for passes traveling towards the same mirror, their combined shapes in cross sections are the same along the length of the cavity, just rotated and resized. We were able to generate similar plots, such as fig. 5.4(d), from ray tracing simulations performed with LightTools 9.0 by Synopsys. Discrepancies between the calculated model and the simulation come from the fact that the simulation uses an input light beam of uniform intensity instead of a Gaussian beam, but it simulates light rays until they exit through either the entry hole or the mirror's edge, while the calculation only uses the first orbit, 32 passes, and does not consider any leakage.

5.4 Prototyping

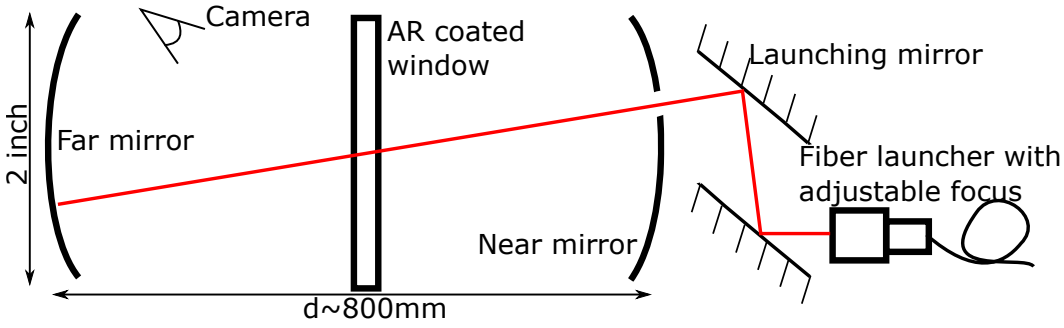

Figure 5.5: Test setup for measuring the performance of the prototype, not to scale.

Based on the information learned from the model, we built a prototype for testing using mostly off-the-shelf 2-inch optics. A focal length of 200 mm was chosen so that the cavity length of 792 mm, 1% less than $4f$ = 800 mm, would fit outside of a vacuum chamber containing atomic and molecular beams for testing. The near mirror is a custom part with a 4 mm diameter hole drilled 5 mm away from the center of the mirror (We used a Thorlabs CM508-200-E02 with the hole added by Advanced Optics, Pewaukee, WI). We have the two cavity mirrors, and the two launching mirrors on kinematic mounts (Thorlabs KC2) while the laser light comes out of a fiber launcher with adjustable focus (Thorlabs C240TMD-A and PM460-HP) close to the entry hole, as shown in Fig. 5.5. The lasers used are single mode ECDLs locked to a wavemeter. We also insert an anti-reflection(AR)-coated window (Thorlabs WG12012-A) into the cavity to image the beams while minimally perturbing the paths and intensities. The AR coated window can slide along the length of the cavity, for measuring longitudinal intensity distribution.

According to simulations and our model, a wide range of parameters are allowed, and

we made choices that strike a good compromise between performance, flexibility, and ease of setting up and aligning. The position and size of the entry hole limit how close the first spot back on the near mirror can be to the entry spot. For us, the largest θ possible is about 169°, which allows for about 32 passes per orbit, so even assuming the entire beam exits through the entry hole after an orbit, there is a 32-fold increase of total power. Of course, our goal is not only higher power but also higher intensity with relatively uniform distribution. In that case, a configuration like the one shown in Fig. 5.4 will be used. The input beam is diverged slightly, such that the first spot back on the near mirror is much larger than the entry hole. While some of the light will exit through the hole, it is small enough to be justifiable by the gain in uniformity, as shown in later sections.

From the prototyping experience, we learned that the procedure for setting up this Herriott cell multi-pass is straightforward. Put the two mirrors on kinematic mounts spaced one cavity-length apart, which is typically just short of four times the focal length, about 792 mm for our prototype. Send in the collimated laser beam, sized just under the entry hole, and land it roughly 169 degrees away from the entry hole projection at the far mirror. Adjust the far mirror orientation so that the first bounce-back to the near mirror almost touches the entry hole, like in Fig. 5.3(a). Finally, adjust the near mirror so that the circular patterns of dots appear. In the process, some adjustment of the focusing of the laser beam might be needed to achieve the "collimated" configuration, just so that we have a clear pattern of dots as indicators. Also, if the cavity length is longer than four times the focal length, the final step of forming the circular pattern will fail, since the spots will always move towards the mirror's edge and never curve back. The solution is simply to push the mirrors closer so that they can curve back to form a circle. The process is fairly robust, without needing any precise placement.

After achieving the "collimated" configuration, diverge the input beam to get a configuration like that in Fig. 5.4. The fact that the cross section at the middle of the cavity has the same shape as that on the mirrors is a very beneficial trait for setting up and optimizing because we can reliably infer the spot characteristics inside the cavity easily just by looking at the mirrors. For optimization, the main concerns are the total power and its distribution. By using a camera or simply by looking at the mirrors, we can optimize by tuning the parameters like cavity length, entry beam focus, or mirror orientations. The total spot size at the illumination region can be changed by changing the longitudinal distance of that region from the middle of the

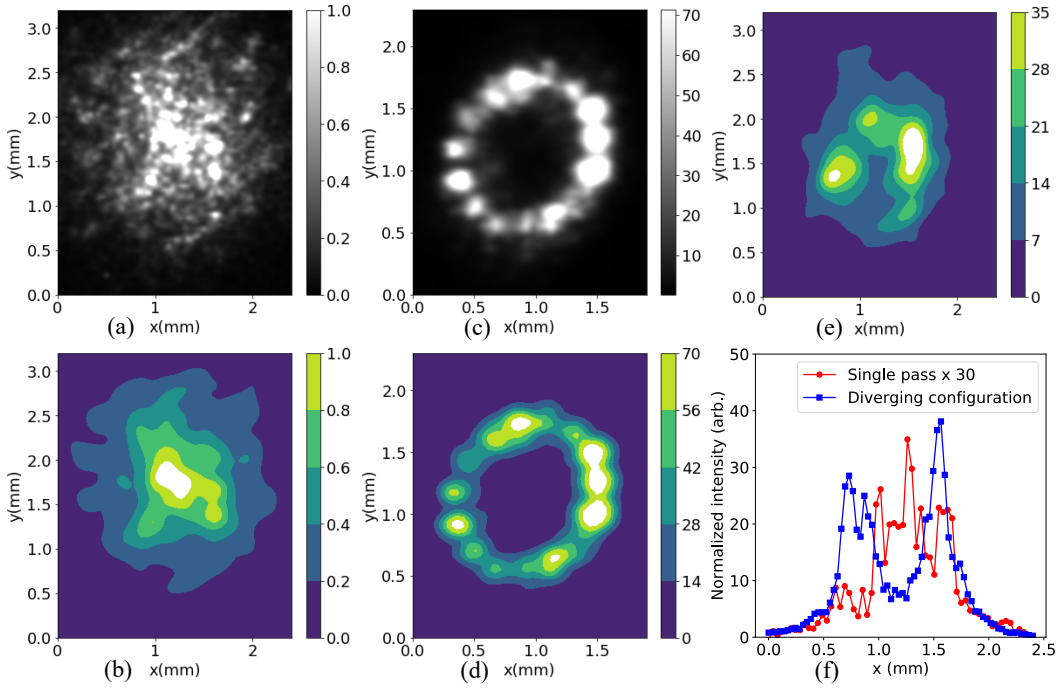

Figure 5.6: Measurement of intensity amplification and distribution. Photos of the scattered light on the AR coated window at the center of the cavity were taken for different configurations using a CMOS camera. (a) is from a single pass of the laser beam and (b) is the contour plot of the same photo. (c) and (d) are photos for the "collimated" configuration. (e) is the contour plot of Fig. 5.4(f). All intensities are normalized against (a). (f) is a uniformity comparison between center slices of (b) and (e) in the x direction, showing that for a range of about 1.2 mm the minimum intensity of the multi-pass is more than 5 times the maximum of the single pass.

cavity. Further discussion is in the later flexibility discussion.

5.5 Performance discussion

To quantify the performance of the setup, we inserted an AR coated window in the middle of the cavity and measured the light scatter using a camera, as shown in Fig. 5.5. We normalized the signal by comparing it to the scattered light from a single pass of the laser beam expanded to a similar size. The results are in good agreement with our simple model and ray tracing simulations, both for the spot shape as well as total power. The results are shown in Fig. 5.4(e,f) and Fig. 5.6. The shape of the spot patterns matches the prediction for all the configurations we tested. We also confirmed our understanding of the intensity distribution along the length of the cavity. While the intensity results are about 10% lower than simulations, it can be improved using higher-grade optics and coatings. Despite the losses, we still

see that on average the intensity is amplified by a factor of about 30, with a fairly uniform distribution.

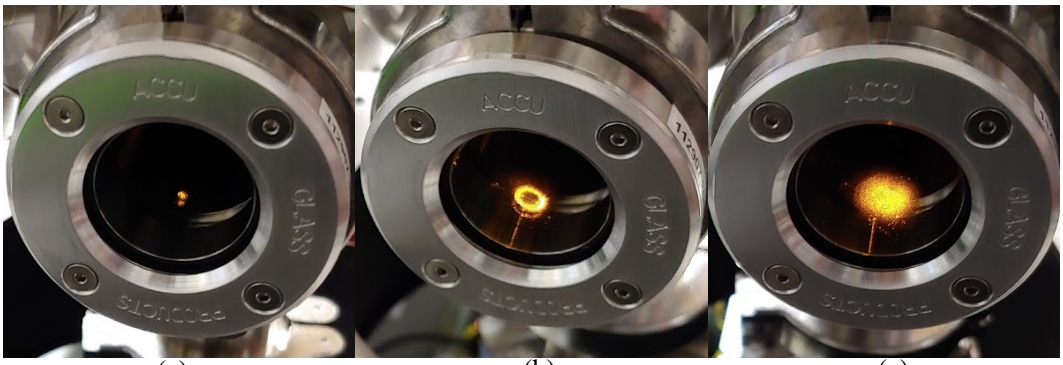

(a) (b) (c)

Figure 5.7: (a) Photo of single-pass light scattered off vacuum chamber window. (b) Photo for the "collimated" Herriott cell setup. (c) Photo for a Herriott cell setup optimized for even intensity distribution. Note that these spots look different in size because the vacuum window is closer to the cavity mirror than the interaction region. The actual size of the interaction region is similar between (a) and (c) like the ones shown in Fig. 5.6.

Another test was to set up the cavity at our cryogenic atomic and molecular beam source [33], and measure the fluorescence of sodium beams using a laser on the D1 transition. Comparing the results from three configurations: 1. a single pass, as shown in Fig. 5.7(a); 2. the Herriott cell multi-pass in the "collimated" configuration, as shown in Fig. 5.7(b); 3. a diverging configuration optimized for even intensity distribution, as shown in Fig. 5.7(c). Using the diverging Herriott cell as a non-resonant power buildup cavity results in an increase in atomic fluorescence by a factor of around 25, as shown in Fig. 5.8. This is less than the factor of 30 that might be expected from the intensity increase, mostly due to saturation of the atomic transition, geometry change of the fluorescing atom cloud, and power loss on the vacuum chamber windows. Otherwise, it shows that we can easily get more than one order of magnitude improvement of the fluorescence signal using the prototype cavity.

5.6 Flexibility and robustness

One of our main goals with the cavity is the ability to build up intensity for multiple lasers of different wavelengths at the same place. Fortunately, since reflective elements naturally have no chromatic aberration, we do not have to worry about the cavity itself. Inevitably, however, the full setup will require some chromatic

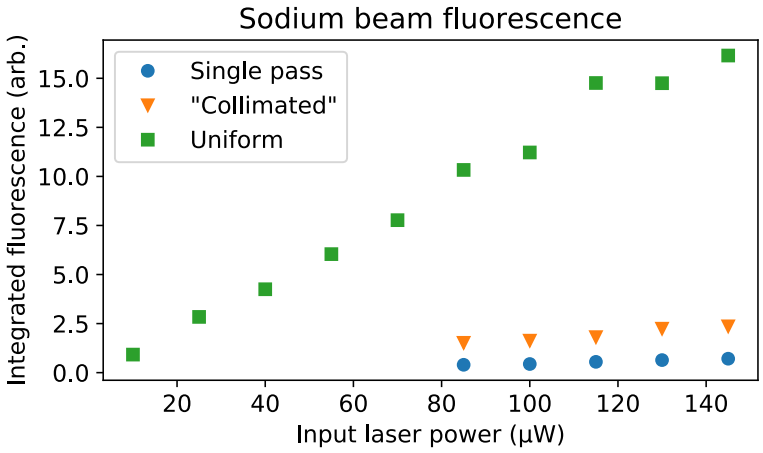

Figure 5.8: Integrated fluorescence of a sodium beam probed on the D1 transition, comparing results from three different configurations: single pass, "collimated" Herriott cell, and diverging configuration like fig. 5.4.

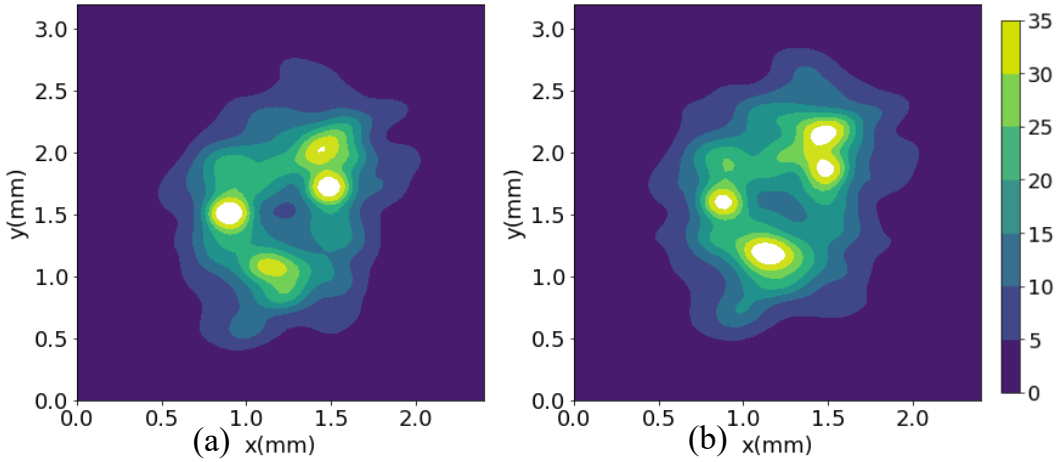

Figure 5.9: (a) Photos of the AR coated window placed at the center of the cavity. Camera is shooting at an angle of about 45°, such that the scattered light from two sides of the window are sufficiently separated. (b) Same as (a) but the laser used is changed from 650 nm to 577 nm.

element in the beam path. To test if chromatic aberration or other wavelength dependent phenomena are of concern, we tried different lasers launched using the same fiber and aspheric lens. As shown in Fig. 5.9, the intensity distributions are very similar between scattered light from a 650 nm laser and a 577 nm laser. This is expected since the setup is very robust against small perturbations as we will discuss, especially if the perturbation is on the input laser, and not on the cavity itself. Therefore, one way to input multiple lasers into the non-resonant cavity is by

combining them into a single fiber, using a combination of dichroic mirrors, beam-splitters, and acousto-optical modulators, as is done with several current molecule MOT experiments [79], or using commercial solutions like fiber clusters [80].

Another very important aspect of our goal is to have an illumination region of adjustable size. The simplest way to change the size of the illuminated spot at the interaction region is by moving the entire cavity lengthwise such that the interaction region is offset away from the middle of the cavity. As mentioned in the previous section, the cross-sectional shape at the center of the cavity is the same as the pattern on the mirrors, just rotated and of different sizes. It is the case for everywhere in between as well, with the size scaled with the position. We can estimate the size of the illuminated region by noticing that the shape of the ray density roughly looks like a cone (see Fig. 5.1(b)) and should therefore be linear in displacement along the cavity:

$$D(z) \approx 4x_0 \left(a + 2z \frac{1-a}{d} \right), \tag{5.2}$$

where z is the longitudinal distance of the illumination region from the middle of the cavity, x_0 is the offset of the entry hole from the center of the mirror, and $a = \pi - \cos^{-1}(1 - d/2f)$ is the angle between two consecutive laser spots on the same mirror. The estimated diameter D of the sphere being covered is twice the diameter of the circle traced out by the beam locations, which is the minimum for diverging configurations. Hence, the estimation is a conservative one. Further increasing the divergence of the input beams will increase the spot size and make the intensity distribution more uniform, though depending on the cavity geometry it might lead to more power loss over the edge of the mirrors.

To test the formula, we measured the size of the illuminated region at different locations along the cavity length. The same measurement setup was used, except the camera is imaging the window with a 25° angle while moving along with the window such that the distance and angle to the window are fixed. Fig. 5.10 shows good agreement between the measured sizes and the ones calculated from Eq. (2).

Finally, we measured the robustness of the cavity against misalignment. In general, the cavity is very robust against small misalignments that might be caused by thermal drifts, vibrations, or even accidental bumps. For the configuration with a more uniform intensity distribution, it is even less prone to misalignment, because in such a configuration the laser beams are expanded to be significantly larger than

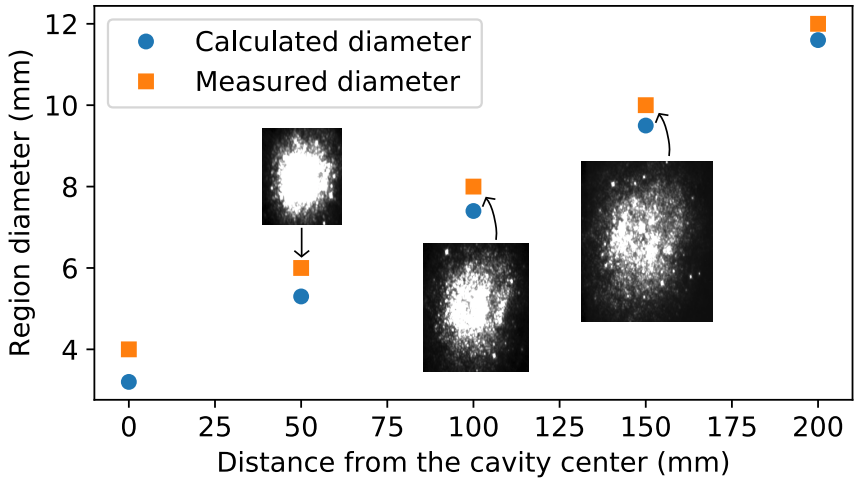

Figure 5.10: Plot showing how the illumination region size changes with the longitudinal distance from the middle of the cavity. The measured size is characterized by the diameter of the cross section where the laser light intensity is higher than the single-pass intensity. The calculated diameter is from Eq. (2). The three inserts show intensity distributions at the corresponding distance, with the same size scale and intensity scale, confirming the uniformity along the cavity length.

the entry hole when they arrive at the mirrors, as shown in Fig. 5.4, such that when they leak out of the mirror due to misalignment, there is little loss of power.

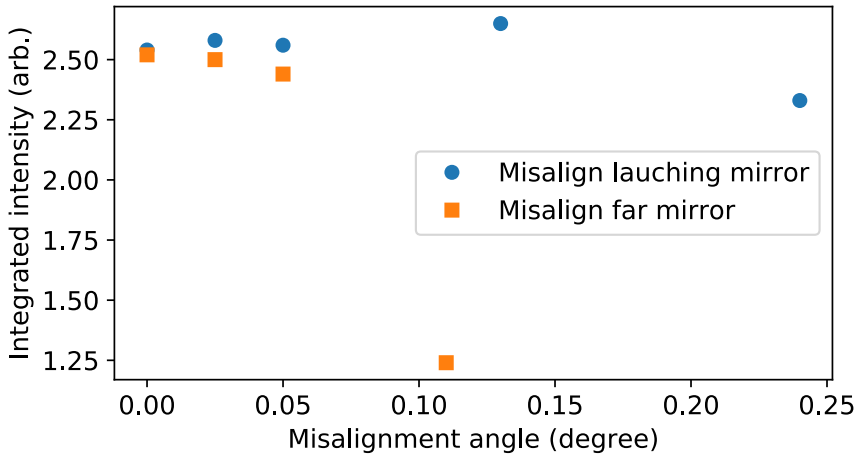

Figure 5.11: Plot showing how misalignment in the launching mirror and far mirror affect the total power inside the illumination region. Significant power loss starts to occur when the launching mirror is misaligned by 0.24°, and when the far mirror is misaligned by 0.05°. Both are larger than typical drifts seen in the lab for common optics elements.

To quantify the sensitivity to misalignment, we measured how the scattered light on the AR coated window changes depending on the misalignment angles of the

mirrors. As expected, turning the cavity mirrors has a much more significant effect than the launching mirror as it changes the cavity condition and deviations accumulate as the laser beam bounces between them. Fig. 5.11 shows how the total power changes with the misalignment angles.

The launching mirror misalignment angles reflect how the input beam is misaligned. When it is misaligned by more than $0.24°$ the total power within the cavity starts to decrease. The far mirror misalignment has the same effect as the near mirror, both misaligning the cavity. Beyond a limit of $0.05°$, the power loss starts to become significant. Clearly, the cavity itself is more susceptible to misalignment than the input laser. Still, both misalignment limits are larger than the typical drifts commonly encountered in the lab; for example, the $0.24°$ misalignment required a half turn of the steering knob on the launching mirror.

This robustness against misalignment is advantageous not just for practical reasons, but also means that applications sensitive to interference can mitigate negative effects by modulating the cavity length. For example, magneto-optical traps often use lasers with long coherence lengths, which means that there can be interference in the retro-reflected beams resulting in non-uniform and varying intensity distributions. A typical solution to this is to add a small oscillating displacement to one of the mirrors [81] which averages over the interference pattern. Given the robustness of the cavity presented here, such a solution could also be implemented if needed.

5.7 Conclusion

We designed and tested a non-resonant cavity for building up laser intensity by over an order of magnitude in a confined region. It is capable of accommodating multiple lasers of different wavelengths and polarizations at the same time and at the same location and is flexible in the size and shape of the illumination region. Furthermore, it is easy to set up and tune and is robust against perturbations without active stabilization. These properties make it a very useful and versatile tool for laser intensity buildup, or even as an alternative to common multi-pass setup, especially when multiple laser wavelengths are required.

Funding

This work was supported by the Heising-Simons Foundation (2022-3361), the Gordon and Betty Moore Foundation (GBMF7947), and the Alfred P. Sloan Foundation (G-2019-12502).

Acknowledgements

We thank Tim Steimle for suggesting that we look into the Herriott cell. We also thank our lab members Arian Jadbabaie and Phelan Yu for fruitful discussions.

Chapter 6

CONCLUSION AND OUTLOOK

As mentioned in Chapter 3, when I joined the lab, there was not much in it, and I had no expectation other than that I would be able to learn and do a wide range of new things. That expectation is thoroughly met. Even better, after years of building, we were able to use what we constructed to do new physics, including the quantum control and measurements of polyatomic molecules. There are plenty of challenges and setbacks along the way, including the non-performing cryogenic system that required a thorough re-engineering, the defective modular vacuum chamber that we had to replace with a custom-designed custom-machined new chamber, and of course, the existence of the f-orbital hole dark states that have branching ratios just a little too high for us to ignore in the YbOH. Despite all that, we are now almost ready to perform our first, and the first, precision measurement of nuclear magnetic quadrupole moment in molecules.

In order to perform the nMQM measurement of ^{173}YbOH in a beam experiment, the main apparatuses we need to have in place and optimized are the CBGB source and the science chamber. I've discussed in some detail about the CBGB in Chapter 3. The science chamber is equally important since it provides highly precise control over the electromagnetic fields and optical access engineered to enhance light collection while minimizing stray scattering at the region where we will perform the spin-precession and measure the nMQM. I participated in the construction and testing of the science chamber, specifically, the magnetic shielding, the degaussing electronics, and the vacuum chamber. However, since I wasn't the main project lead, I didn't discuss many details about most of the science chamber. For detailed information, I would recommend ref. [29, 82].

Aside from the main physical apparatuses, there is a lot of infrastructure that has to be built and there are many experimental schemes to be devised and tested. Among this infrastructure, I built the experiment control, data-taking, and laser locking systems, which are discussed in the Appendix. Among the experiments in preparation for the final nMQM experiments, I participated in the spectroscopy of YbOH, including the hyperfine structure and the bending mode as discussed in Chapter 3.3, I conducted the photon cycling test of ^{173}YbOH, which is discussed in detail in Chapter 4, and

I participated in spin-precession test done with ^{174}YbOH as an analog as discussed in Chapter 3.6.

The actually nMQM experiments will be spin-precession done on ^{173}YbOH, with much better field control afforded by the new science chamber, and with optimized specific state and process selection that maximize the nMQM enhancement and systematic error suppression. We now have most of the components ready.

The other main experiment, eEDM measurements with trapped molecules, is hit particularly hard by the realization that YbOH possesses some f-orbital hole states with high enough branching ratios to become significant dark states. The initial study of the f-orbital hole states was done on YbF by Chi Zhang when he was in Mike Tarbutt's group [83]. Later it was observed in YbOH by the Doyle group at Harvard. Combined with the calculation done by Lan Cheng, it is determined that YbOH trapping will require extra repump lasers and extra spectroscopy work. These are most likely doable, but the time horizon of achieving the eventual goal will be much longer than expected. As a result, the PolyEDM collaboration has pivoted to SrOH instead. While it is less sensitive to the CPV physics, we are likely to have it trapped with much higher density relatively easily. Currently, our 1 K CBGB source is used for SrOH bending mode spectroscopy.

As mentioned in Chapter 3.7, I did the initial tests for Chi's proposal of sympathetic cooling and slowing of molecules with Rydberg atoms. It would be exciting to see if we can demonstrate some observable effect to prove that the idea is worth pursuing. If it works, then we might soon have a universal molecule trap that can trap molecules regardless of its photon cycling capability. It will open up many new avenues for the study of not only precision measurements but also for fields like quantum chemistry.

BIBLIOGRAPHY

[1]T. Chen, W. Bu, and B. Yan, "Structure, branching ratios, and a laser-cooling scheme for the ^{138}BaF molecule", Phys. Rev. A **94**, 063415 (2016) 10.1103/PhysRevA.94.063415.

[2]C. Li, Y. Li, Z. Ji, X. Qiu, Y. Lai, J. Wei, Y. Zhao, L. Deng, Y. Chen, and J. Liu, "Candidates for direct laser cooling of diatomic molecules with the simplest sigma to sigma electronic system", Physical Review A **97**, 10.1103/physreva.97.062501 (2018) 10.1103/physreva.97.062501.

[3]M. V. Ramanaiah and S. V. J. Lakshman, "True potential energy curves, r-centroids and franck-condon factors of a few transition metal diatomic molecules", Pramana **22**, 11–16 (1984) 10.1007/bf02875582.

[4]M.-j. Wan, J.-x. Shao, D.-h. Huang, C.-g. Jin, Y. Yu, and F.-h. Wang, "Laser cooling of becl and bebr molecules in an ab initio method", Physical Chemistry Chemical Physics **17**, 26731–26739 (2015) 10.1039/c5cp03677a.

[5]X. Yuan, H.-J. Guo, Y.-M. Wang, J.-L. Xue, H.-F. Xu, and B. Yan, "Laser-cooling with an intermediate electronic state: theoretical prediction on bismuth hydride", The Journal of Chemical Physics **150**, 10.1063/1.5094367 (2019) 10.1063/1.5094367.

[6]M. S. Sozzi, *Discrete symmetries and cp violation: from experiment to theory* (Oxford University Press, 2012).

[7]Y. Ema, T. Gao, and M. Pospelov, "Standard model prediction for paramagnetic electric dipole moments", Phys. Rev. Lett. **129**, 231801 (2022) 10.1103/PhysRevLett.129.231801.

[8]G. Kane, *Modern elementary particle physics* (Addison-Wesley, 1987).

[9]P. Huet and E. Sather, "Electroweak baryogenesis and standard model cp violation", Phys. Rev. D **51**, 379–394 (1995) 10.1103/PhysRevD.51.379.

[10]M. Dine and A. Kusenko, "Origin of the matter-antimatter asymmetry", Rev. Mod. Phys. **76**, 1–30 (2003) 10.1103/RevModPhys.76.1.

[11]N. R. Hutzler, "A new limit on the electron electric dipole moment: beam production, data interpretation, and systematics", PhD thesis (Cambridge, Massachusetts, 2014).

[12]M. Pospelov and A. Ritz, "Ckm benchmarks for electron electric dipole moment experiments", Phys. Rev. D **89**, 056006 (2014) 10.1103/PhysRevD.89.056006.

[13]I. Esteban, M. C. Gonzalez-Garcia, M. Maltoni, T. Schwetz, and A. Zhou, "The fate of hints: updated global analysis of three-flavor neutrino oscillations", 10.48550/ARXIV.2007.14792 (2020) 10.48550/ARXIV.2007.14792.

[14]C. Abel, S. Afach, N. J. Ayres, C. A. Baker, G. Ban, G. Bison, K. Bodek, V. Bondar, M. Burghoff, E. Chanel, Z. Chowdhuri, P.-J. Chiu, B. Clement, C. B. Crawford, M. Daum, S. Emmenegger, L. Ferraris-Bouchez, M. Fertl, P. Flaux, B. Franke, A. Fratangelo, P. Geltenbort, K. Green, W. C. Griffith, M. van der Grinten, Z. D. Gruji ć, P. G. Harris, L. Hayen, W. Heil, R. Henneck, V. Hélaine, N. Hild, Z. Hodge, M. Horras, P. Iaydjiev, S. N. Ivanov, M. Kasprzak, Y. Kermaidic, K. Kirch, A. Knecht, P. Knowles, H.-C. Koch, P. A. Koss, S. Komposch, A. Kozela, A. Kraft, J. Krempel, M. Ku źniak, B. Lauss, T. Lefort, Y. Lemière, A. Leredde, P. Mohanmurthy, A. Mtchedlishvili, M. Musgrave, O. Naviliat-Cuncic, D. Pais, F. M. Piegsa, E. Pierre, G. Pignol, C. Plonka-Spehr, P. N. Prashanth, G. Quéméner, M. Rawlik, D. Rebreyend, I. Rienäcker, D. Ries, S. Roccia, G. Rogel, D. Rozpedzik, A. Schnabel, P. Schmidt-Wellenburg, N. Severijns, D. Shiers, R. Tavakoli Dinani, J. A. Thorne, R. Virot, J. Voigt, A. Weis, E. Wursten, G. Wyszynski, J. Zejma, J. Zenner, and G. Zsigmond, "Measurement of the permanent electric dipole moment of the neutron", Phys. Rev. Lett. **124**, 081803 (2020) 10.1103/PhysRevLett.124.081803.

[15]ACME Collaboration, "Improved limit on the electric dipole moment of the electron", en, Nature **562**, 355–360 (2018).

[16]T. S. Roussy, L. Caldwell, T. Wright, W. B. Cairncross, Y. Shagam, K. B. Ng, N. Schlossberger, S. Y. Park, A. Wang, J. Ye, and E. A. Cornell, "An improved bound on the electron's electric dipole moment", Science **381**, 46–50 (2023) 10.1126/science.adg4084.

[17]J. Baron, W. C. Campbell, D. DeMille, J. M. Doyle, G. Gabrielse, Y. V. Gurevich, P. W. Hess, N. R. Hutzler, E. Kirilov, I. Kozyryev, B. R. O'Leary, C. D. Panda, M. F. Parsons, B. Spaun, A. C. Vutha, A. D. West, E. P. West, and A. Collaboration, "Methods, analysis, and the treatment of systematic errors for the electron electric dipole moment search in thorium monoxide", New Journal of Physics **19**, 073029 (2017) 10.1088/1367-2630/aa708e.

[18]N. H. Pilgram, A. Jadbabaie, Y. Zeng, N. R. Hutzler, and T. C. Steimle, "Fine and hyperfine interactions in ^{171}YbOH and ^{173}YbOH", J. Chem. Phys. **154**, 244309 (2021) 10.1063/5.0055293.

[19]V. V. Flambaum, D. DeMille, and M. G. Kozlov, "Time-Reversal Symmetry Violation in Molecules Induced by Nuclear Magnetic Quadrupole Moments", Phys. Rev. Lett. **113**, 103003 (2014) 10.1103/PhysRevLett.113.103003.

[20]C. J. Ho, J. Lim, B. E. Sauer, and M. R. Tarbutt, "Measuring the nuclear magnetic quadrupole moment in heavy polar molecules", Frontiers in Physics **11**, 10.3389/fphy.2023.1086980 (2023) 10.3389/fphy.2023.1086980.

[21]N. R. Hutzler, "Polyatomic molecules as quantum sensors for fundamental physics", Quantum Science and Technology **5**, 044011 (2020) 10.1088/2058-9565/abb9c5.

[22]N. Auerbach, V. V. Flambaum, and V. Spevak, "Collective t- and p-odd electromagnetic moments in nuclei with octupole deformations", Phys. Rev. Lett. **76**, 4316–4319 (1996) 10.1103/PhysRevLett.76.4316.

[23]V. Flambaum and J. Ginges, "Nuclear Schiff moment and time-invariance violation in atoms", Phys. Rev. A **65**, 1–9 (2002) 10.1103/PhysRevA.65.032113.

[24]S. A. Murthy, D. Krause, Z. L. Li, and L. R. Hunter, "New limits on the electron electric dipole moment from cesium", Phys. Rev. Lett. **63**, 965–968 (1989) 10.1103/PhysRevLett.63.965.

[25]B. Graner, Y. Chen, E. G. Lindahl, and B. R. Heckel, "Reduced limit on the permanent electric dipole moment of ^{199}Hg", Phys. Rev. Lett. **116**, 161601 (2016) 10.1103/PhysRevLett.116.161601.

[26]E. D. Commins, J. D. Jackson, and D. P. DeMille, "The electric dipole moment of the electron: an intuitive explanation for the evasion of schiff's theorem", American Journal of Physics **75**, 532–536 (2007) 10.1119/1.2710486.

[27]M. Safronova, D. Budker, D. DeMille, D. F. J. Kimball, A. Derevianko, and C. W. Clark, "Search for new physics with atoms and molecules", Reviews of Modern Physics **90**, 10.1103/revmodphys.90.025008 (2018) 10.1103/revmodphys.90.025008.

[28]N. B. Vilas, C. Hallas, L. Anderegg, P. Robichaud, A. Winnicki, D. Mitra, and J. M. Doyle, "Magneto-optical trapping and sub-Doppler cooling of a polyatomic molecule", Nature **606**, 70–74 (2022) 10.1038/s41586-022-04620-5.

[29]A. Jadbabaie, "Measuring fundamental symmetry violation in polyatomic molecules", PhD thesis (Pasadena, California, 2023).

[30]A. Jadbabaie, Y. Takahashi, N. H. Pilgram, C. J. Conn, Y. Zeng, C. Zhang, and N. R. Hutzler, "Characterizing the fundamental bending vibration of a linear polyatomic molecule for symmetry violation searches", New Journal of Physics **25**, 073014 (2023) 10.1088/1367-2630/ace471,

[31]J. Brown and A. Carrington, *Rotational Spectroscopy of Diatomic Molecules* (Cambridge University Press, 2003).

[32]J. M. Brown, I. Kopp, C. Malmberg, and B. Rydh, "An analysis of hyperfine interactions in the electronic spectrum of aif", Physica Scripta **17**, 55–67 (1978) 10.1088/0031-8949/17/2/003.

[33]N. R. Hutzler, H.-I. Lu, and J. M. Doyle, "The buffer gas beam: an intense, cold, and slow source for atoms and molecules.", Chem. Rev. **112**, 4803–27 (2012) 10.1021/cr200362u.

[34]A. Jadbabaie, N. H. Pilgram, J. Kłos, S. Kotochigova, and N. R. Hutzler, "Enhanced molecular yield from a cryogenic buffer gas beam source via excited state chemistry", New Journal of Physics **22**, 022002 (2020) 10.1088/1367-2630/ab6eae.

[35]B. L. Augenbraun, "Methods for direct laser cooling of polyatomic molecules", PhD thesis (Cambridge, Massachusetts, 2021).

[36]T. C. Steimle, C. Linton, E. T. Mengesha, X. Bai, and A. T. Le, "Field-free, Stark, and Zeeman spectroscopy of the $\tilde{A}^2\Pi_{1/2} - \tilde{X}^2\Sigma^+$ transition of ytterbium monohydroxide", Physical Review A **100**, 052509 (2019).

[37]Y. Zeng, A. Jadbabaie, A. N. Patel, P. Yu, T. C. Steimle, and N. R. Hutzler, "Optical cycling in polyatomic molecules with complex hyperfine structure", Phys. Rev. A **108**, 012813 (2023) 10.1103/PhysRevA.108.012813,

[38]R. Chang, J. He, and J. Wang, "Interference filter based external-cavity diode laser with combined dual interference filters and largely adjustable feedback range", Physica Scripta **98**, 125111 (2023) 10.1088/1402-4896/ad0943.

[39]C. J. Hawthorn, K. P. Weber, and R. E. Scholten, "Littrow configuration tunable external cavity diode laser with fixed direction output beam", Review of Scientific Instruments **72**, 4477–4479 (2001) 10.1063/1.1419217.

[40]E. A. Donley, T. P. Heavner, F. Levi, M. O. Tataw, and S. R. Jefferts, "Double-pass acousto-optic modulator system", Review of Scientific Instruments **76**, 063112 (2005) 10.1063/1.1930095.

[41]I. Dotsenko, W. Alt, S. Kuhr, D. Schrader, M. Müller, Y. Miroshnychenko, V. Gomer, A. Rauschenbeutel, and D. Meschede, "Application of electro-optically generated light fields for raman spectroscopy of trapped cesium atoms", Applied Physics B **78**, 711–717 (2004) 10.1007/s00340-004-1467-9.

[42]C. Zhang, S. T. Rittenhouse, T. V. Tscherbul, H. R. Sadeghpour, and N. R. Hutzler, "Sympathetic cooling and slowing of molecules with rydberg atoms", Phys. Rev. Lett. **132**, 033001 (2024) 10.1103/PhysRevLett.132.033001.

[43]N. Fitch and M. Tarbutt, "Laser-cooled molecules", Adv. At. Mol. Opt. Phys. **70**, 157–262 (2021) 10.1016/bs.aamop.2021.04.003.

[44]B. L. Augenbraun, L. Anderegg, C. Hallas, Z. D. Lasner, N. B. Vilas, and J. M. Doyle, "Direct Laser Cooling of Polyatomic Molecules", arXiv:2302.10161 (2023).

[45]L. D. Carr, D. DeMille, R. V. Krems, and J. Ye, "Cold and ultracold molecules: science, technology and applications", New J. Phys. **11**, 55049 (2009) 10.1088/1367-2630/11/5/055049.

[46]J. L. Bohn, A. M. Rey, and J. Ye, "Cold molecules: Progress in quantum engineering of chemistry and quantum matter", Science **357**, 1002–1010 (2017) 10.1126/science.aam6299.

[47]D. DeMille, J. M. Doyle, and A. O. Sushkov, "Probing the frontiers of particle physics with tabletop-scale experiments", Science **357**, 990–994 (2017) 10.1126/science.aal3003.

[48]C. S. Wood, S. C. Bennett, D. Cho, B. P. Masterson, J. L. Roberts, C. E. Tanner, and C. E. Wieman, "Measurement of parity nonconservation and an anapole moment in cesium", Science **275**, 1759–1763 (1997) 10.1126/science.275.5307.1759.

[49]E. Altunta ş, J. Ammon, S. B. Cahn, and D. DeMille, "Demonstration of a sensitive method to measure nuclear-spin-dependent parity violation", Phys. Rev. Lett. **120**, 142501 (2018) 10.1103/PhysRevLett.120.142501.

[50]S. M. Udrescu, A. J. Brinson, R. F. G. Ruiz, K. Gaul, R. Berger, J. Billowes, C. L. Binnersley, M. L. Bissell, A. A. Breier, K. Chrysalidis, T. E. Cocolios, B. S. Cooper, K. T. Flanagan, T. F. Giesen, R. P. de Groote, S. Franchoo, F. P. Gustafsson, T. A. Isaev, A. Koszorús, G. Neyens, H. A. Perrett, C. M. Ricketts, S. Rothe, A. R. Vernon, K. D. A. Wendt, F. Wienholtz, S. G. Wilkins, and X. F. Yang, "Isotope Shifts of Radium Monofluoride Molecules", Phys. Rev. Lett. **127**, 033001 (2021) 10.1103/PhysRevLett.127.033001.

[51]G. Arrowsmith-Kron, M. Athanasakis-Kaklamanakis, M. Au, J. Ballof, R. Berger, A. Borschevsky, A. A. Breier, F. Buchinger, D. Budker, L. Caldwell, C. Charles, N. Dattani, R. P. de Groote, D. DeMille, T. Dickel, J. Dobaczewski, C. E. Düllmann, E. Eliav, J. Engel, M. Fan, V. Flambaum, K. T. Flanagan, A. Gaiser, R. G. Ruiz, K. Gaul, T. F. Giesen, J. Ginges, A. Gottberg, G. Gwinner, R. Heinke, S. Hoekstra, J. D. Holt, N. R. Hutzler, A. Jayich, J. Karthein, K. G. Leach, K. Madison, S. Malbrunot-Ettenauer, T. Miyagi, I. D. Moore, S. Moroch, P. Navrátil, W. Nazarewicz, G. Neyens, E. Norrgard, N. Nusgart, L. F. Pašteka, A. N. Petrov, W. Plass, R. A. Ready, M. P. Reiter, M. Reponen, S. Rothe, M. Safronova, C. Scheidenberger, A. Shindler, J. T. Singh, L. V. Skripnikov, A. V. Titov, S.-M. Udrescu, S. G. Wilkins, and X. Yang, "Opportunities for Fundamental Physics Research with Radioactive Molecules", arXiv:2302.02165 (2023).

[52]E. B. Norrgard, D. S. Barker, S. Eckel, J. A. Fedchak, N. N. Klimov, and J. Scherschligt, "Nuclear-spin dependent parity violation in optically trapped polyatomic molecules", Commun. Phys. **2**, 77 (2019) 10.1038/s42005-019-0181-1.

[53]I. Kozyryev and N. R. Hutzler, Phys. Rev. Lett. **119**, 133002 (2017) 10.1103/PhysRevLett.119.133002.

[54]D. E. Maison, L. V. Skripnikov, and V. V. Flambaum, "Theoretical study of ^{173}YbOH to search for the nuclear magnetic quadrupole moment", Phys. Rev. A **100**, 032514 (2019) 10.1103/PhysRevA.100.032514.

[55]M. Denis, Y. Hao, E. Eliav, N. R. Hutzler, M. K. Nayak, R. G. E. Timmermans, and A. Borschesvky, "Enhanced p, t-violating nuclear magnetic quadrupole moment effects in laser-coolable molecules", The Journal of Chemical Physics **152**, 084303 (2020) 10.1063/1.5141065.

[56]L. Anderegg, N. B. Vilas, C. Hallas, P. Robichaud, A. Jadbabaie, J. M. Doyle, and N. R. Hutzler, "Quantum Control of Trapped Polyatomic Molecules for eEDM Searches", arXiv:2301.08656 (2023).

[57]Y. Takahashi, C. Zhang, A. Jadbabaie, and N. R. Hutzler, *Engineering field-insensitive molecular clock transitions for symmetry violation searches*, 2023.

[58]E. T. Mengesha, A. T. Le, T. C. Steimle, L. Cheng, C. Zhang, B. L. Augenbraun, Z. Lasner, and J. Doyle, "Branching Ratios, Radiative Lifetimes, and Transition Dipole Moments for YbOH", J. Phys. Chem. A **124**, 3135–3148 (2020) 10.1021/acs.jpca.0c00850.

[59]B. L. Augenbraun, Z. D. Lasner, A. Frenett, H. Sawaoka, C. Miller, T. C. Steimle, and J. M. Doyle, "Laser-cooled polyatomic molecules for improved electron electric dipole moment searches", New J. Phys. **22**, 022003 (2020) 10.1088/1367-2630/ab687b.

[60]C. Zhang, B. L. Augenbraun, Z. D. Lasner, N. B. Vilas, J. M. Doyle, and L. Cheng, "Accurate prediction and measurement of vibronic branching ratios for laser cooling linear polyatomic molecules", J. Chem. Phys. **155**, 091101 (2021) 10.1063/5.0063611.

[61]M. D. Di Rosa, "Laser-cooling molecules", Eur. Phys. J. D **31**, 395–402 (2004) 10.1140/epjd/e2004-00167-2.

[62]F. Kogel, M. Rockenhäuser, R. Albrecht, and T. Langen, "A laser cooling scheme for precision measurements using fermionic barium monofluoride (^{137}Ba^{19}F) molecules", New J. Phys. **23**, 095003 (2021) 10.1088/1367-2630/ac1df2.

[63]C. M. Holland, Y. Lu, and L. W. Cheuk, "Synthesizing optical spectra using computer-generated holography techniques", New Journal of Physics **23**, 033028 (2021) 10.1088/1367-2630/abe973.

[64]S. Nakhate, T. C. Steimle, N. H. Pilgram, and N. R. Hutzler, "The pure rotational spectrum of YbOH", Chemical Physics Letters **715**, 105–108 (2019).

[65]B. K. Stuhl, B. C. Sawyer, D. Wang, and J. Ye, "Magneto-optical trap for polar molecules", Physical review letters **101**, 243002 (2008).

[66]Z. Lasner and D. DeMille, "Statistical sensitivity of phase measurements via laser-induced fluorescence with optical cycling detection", Physical Review A **98**, 10.1103/physreva.98.053823 (2018) 10.1103/physreva.98.053823.

[67]J. C. Shaw, J. C. Schnaubelt, and D. J. McCarron, "Resonance raman optical cycling for high-fidelity fluorescence detection of molecules", Phys. Rev. Res. **3**, L042041 (2021) 10.1103/PhysRevResearch.3.L042041.

[68]X. Alauze, J. Lim, M. A. Trigatzis, S. Swarbrick, F. J. Collings, N. J. Fitch, B. E. Sauer, and M. R. Tarbutt, "An ultracold molecular beam for testing fundamental physics", Quantum Sci. Technol. **6**, 044005 (2021) 10.1088/2058-9565/ac107e.

[69]Y. Zeng and N. R. Hutzler, "Nonresonant cavity for multipass laser intensity buildup", Appl. Opt. **62**, 3574–3580 (2023) 10.1364/AO.487531,

[70]J. A. Barnes, T. E. Gough, and M. Stoer, "Laser power build-up cavity for high-resolution laser spectroscopy", Review of Scientific Instruments **70**, 3515–3518 (1999) 10.1063/1.1149952.

[71]D. A. King and R. J. Pittaro, "Simple diode pumping of a power-buildup cavity", Optics Letters **23**, 774 (1998) 10.1364/ol.23.000774.

[72]S. Ohara, S. Yamaguchi, M. Endo, K. Nanri, and T. Fujioka, "Performance characteristics of power build-up cavity for raman spectroscopic measurement", Optical Review **10**, 342–345 (2003) 10.1007/s10043-003-0342-y.

[73]I. Kozyryev, L. Baum, K. Matsuda, B. L. Augenbraun, L. Anderegg, A. P. Sedlack, and J. M. Doyle, "Sisyphus laser cooling of a polyatomic molecule", Physical Review Letters **118**, 10.1103/physrevlett.118.173201 (2017) 10.1103/physrevlett.118.173201.

[74]E. S. Shuman, J. F. Barry, and D. DeMille, "Laser cooling of a diatomic molecule", Nature **467**, 820–823 (2010) 10.1038/nature09443.

[75]D. R. Herriott and H. J. Schulte, "Folded optical delay lines", Applied Optics **4**, 883 (1965) 10.1364/ao.4.000883.

[76]C. G. Tarsitano and C. R. Webster, "Multilaser herriott cell for planetary tunable laser spectrometers", Applied Optics **46**, 6923 (2007) 10.1364/ao.46.006923.

[77]C. Robert, "Simple, stable, and compact multiple-reflection optical cell for very long optical paths", Applied Optics **46**, 5408 (2007) 10.1364/ao.46.005408.

[78]B. E. Saleh and M. C. Teich, *Fundamentals of photonics* (John Wiley & sons, 2019).

[79]J. F. Barry, "Laser cooling and slowing of a diatomic molecule", PhD thesis (New Haven, Connecticut, 2013).

[80]H. J. Williams, S. Truppe, M. Hambach, L. Caldwell, N. J. Fitch, E. A. Hinds, B. E. Sauer, and M. R. Tarbutt, "Characteristics of a magneto-optical trap of molecules", New Journal of Physics **19**, 113035 (2017) 10.1088/1367-2630/aa8e52.

[81]L. R. Liu, "Building single molecules - reactions, collisions, and spectroscopy of two atoms", PhD thesis (Cambridge, Massachusetts, 2019).

[82]A. C. Vutha, "A search for the electric dipole moment of the electron using thorium monoxide", PhD thesis (New Haven, Connecticut, 2011).

[83]C. Zhang, C. Zhang, L. Cheng, T. C. Steimle, and M. R. Tarbutt, "Inner-shell excitation in the ybf molecule and its impact on laser cooling", Journal of Molecular Spectroscopy **386**, 111625 (2022) 10.1016/j.jms.2022.111625.

[84]Y. V. Gurevich, "Preliminary measurements for an electron edm experiment in tho", PhD thesis (Cambridge, Massachusetts, 2012).

[85]B. L. Augenbraun, A. Frenett, H. Sawaoka, C. Hallas, N. B. Vilas, A. Nasir, Z. D. Lasner, and J. M. Doyle, "Zeeman-sisyphus deceleration of molecular beams", Phys. Rev. Lett. **127**, 263002 (2021) 10.1103/PhysRevLett.127.263002.

[86]W. Demtroder, *Molecular physics* (Wiley Vch, 2017).

[87]W. C. Stwalley, W. T. Zemke, and S. C. Yang, "Spectroscopy and structure of the alkali hydride diatomic molecules and their ions", Journal of Physical and Chemical Reference Data **20**, 153–187 (1991) 10.1063/1.555906.

[88]W. C. Stwalley and W. T. Zemke, "Spectroscopy and structure of the lithium hydride diatomic molecules and ions", Journal of Physical and Chemical Reference Data **22**, 87–112 (1993) 10.1063/1.555936.

Appendix A

APPENDIX

A.1 DAQ: experiment control and data taking

I'll share what I built for experiment control and data taking here. Hopefully, it can help future lab members figure out how things work and avoid some of my folly. The System is built for both the nMQM beam measurement experiment (4 K) and the eEDM trap measurement experiment (1 K). Arian Jadbabaie made some additions and small modifications to the 4 K system, mostly for scanning E and B fields, as well as controlling some RF electronics. Here, I will only show the current state of the DAQ for the 1 K system.

An important note before I proceed. I've never received any systematic training in Labview, control systems, or even programming. Everything was built alongside me learning things as needed. As a result, while everything worked as intended, there are no doubt obvious rookie mistakes everywhere. Currently, there's a known bug where, when running the repetition rate above $\sim$ 15 Hz, the whole system could stutter. Fortunately, we don't currently need to run our experiment that fast, and anything above 10 Hz could introduce excess heat load and raise the CBGB source temperature.

The hardware we used is a National Instruments PXIe system. It consists of a PXIe-1073 chassis, a multifunction PXIe-6361 card for experiment control and data taking, and an analog output PXIe-6738 card mostly for laser locking. The system is connected digitally to the control computer with a PCIe card integrated into the chassis, and the two function cards are connected with shielded analog cables to either a shielded BNC terminal or a shielded screw terminal block, which the instruments and lasers connected to.

The Labview code used for controlling the experiments and taking data was built from scratch. The goal is to make it modular and easily expandable, since as a new lab, we are constantly evolving and running different types of experiments over time. Also, we want to make sure that all the instrument is synced correctly and that the data saving won't skip files due to any temporary resource bottleneck on the computer end. To achieve that, we used an architecture called the state machine for the experiment control, and we used queue operations to parallelize the data taking

and saving.

The state machine is a common architecture where a case structure is used within a loop, each case would change the case parameter at the end of its run, possibly based on conditions. Even for simple sequentially executed cases like ours, it is a good way to make the block diagram easy to read and edit. Plus, it provides modularity and flexibility for the scenario where we want to run some special cases only when certain conditions are met. As for the timing, we mostly used a mixture of internal timing in the PXIe system, external digital triggers, and a jump wire sending trigger syncing the digital output sending out control signals, and the data-taking loop.

The master control is a digital output task (multiple lines), which is initiated upon receiving a trigger pulse from an external source, like a function generator, that determines the overall repetition rate of the whole system. One of the channels of that master control task will send out a pulse at the desired time to trigger the start of an analog input task for data taking. The trigger is sent and taken by the same BNC terminal block for the PXIe-6361 through a short jump wire. I suspect there's a better way to conduct timing sync of different tasks on the same PXIe card. The master control task takes in a single .txt file we call the command file. It's a matrix of 0s and 1s that's created and edited using Microsoft Excel. The columns are the digital output channels, rows are separated by a set time interval, 0 is low and 1 is high. For example, if the first channel is the one sending the trigger to start the data taking, we want to start data taking at 20 ms, and the time interval is set at 10 ms, then we will have the first column be 0010000...

The following figures are screenshots of the experiment control and data taking VIs. Information worth noting will be in the captions.

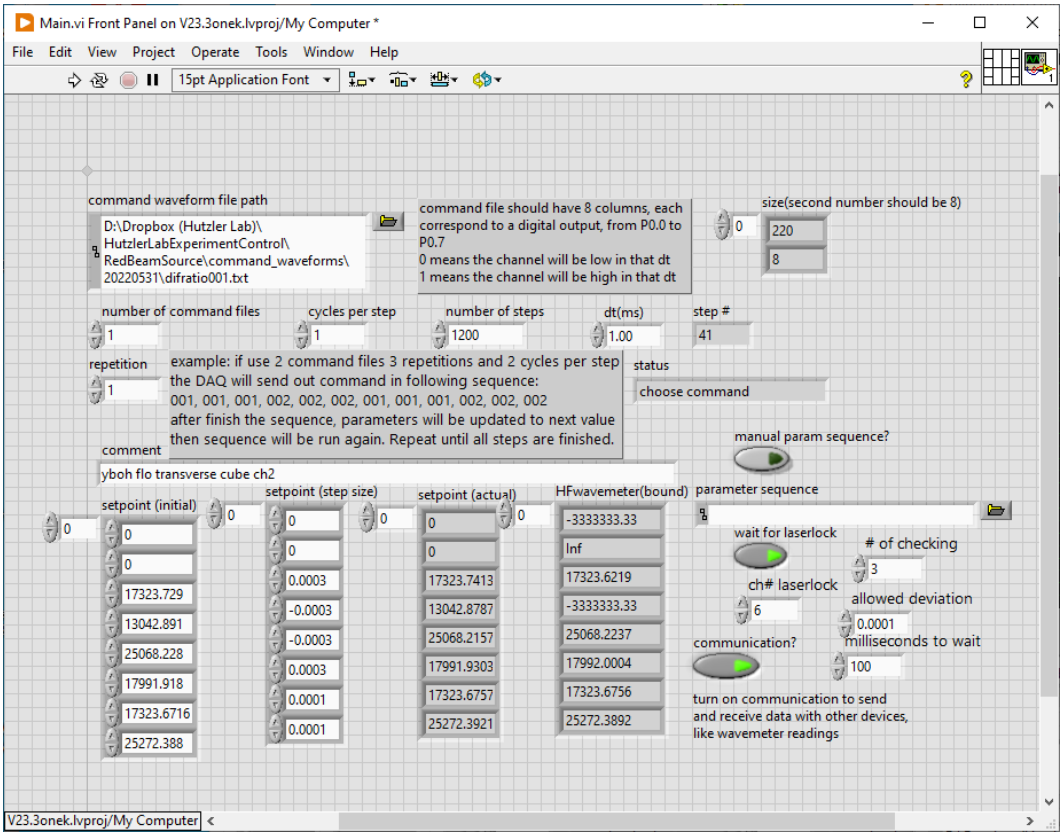

Figure A.1: The front panel of the experiment control VI.

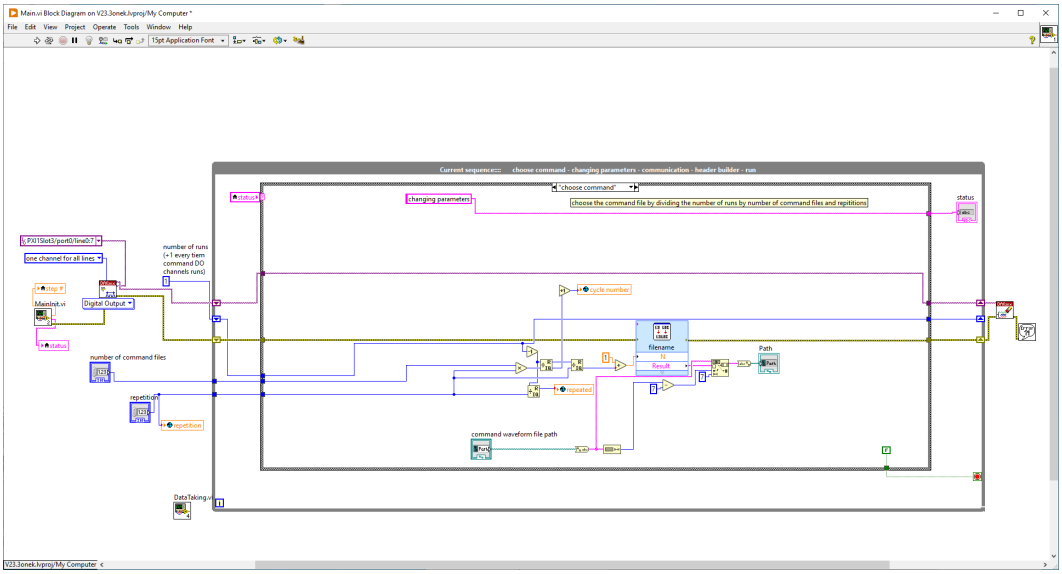

Figure A.2: Block diagram of the experiment control VI, "choose command" state of the state machine. This is the first state to run, choosing the command file based on the number of runs in each step. See Figure A.1 for how cycle, step, repetition, and number of command files work. Command files are named XXX001, XXX002, XXX003, etc.

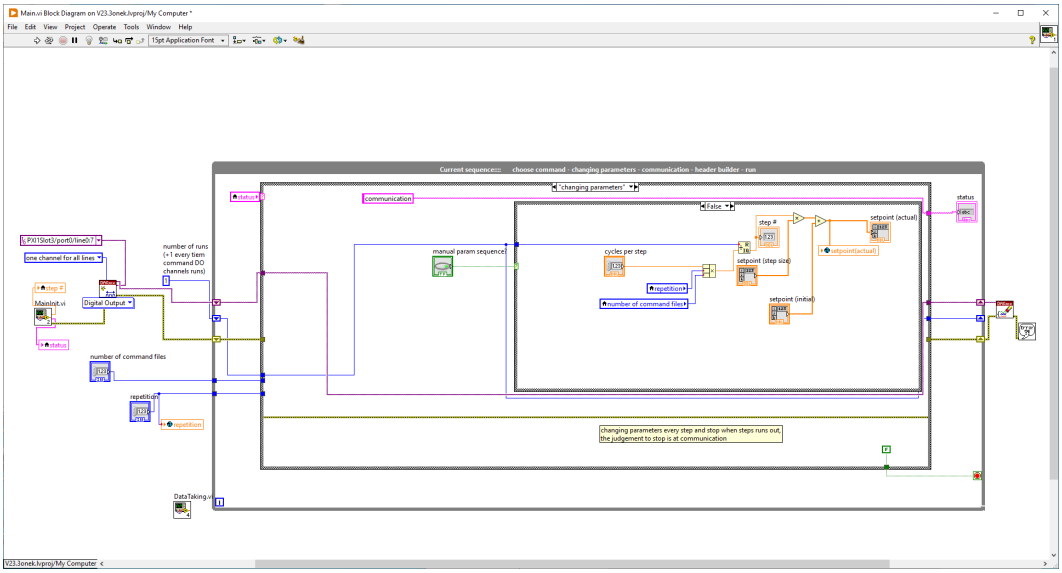

Figure A.3: Block diagram of the experiment control VI, "changing parameters" state of the state machine. This is the second state to run. Here we are changing the wavelength setpoints of our lasers automatically based on step numbers, basically scanning the lasers. We can also manually input arbitrary parameters for each step, like jumping the laser wavelengths around arbitrarily.

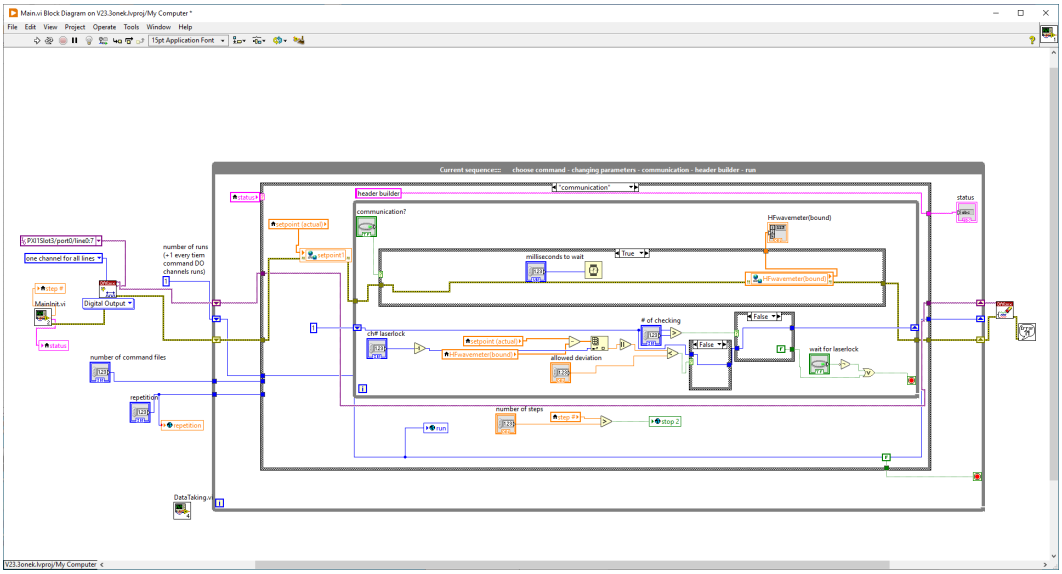

Figure A.4: Block diagram of the experiment control VI, "communication" state of the state machine. This is the third state to run. Here we send out and receive parameters like the laser wavelengths via shared variables. We also have a condition check we can turn on to wait until the laser lock has moved the lasers to the correct wavelength before moving on to the next state.

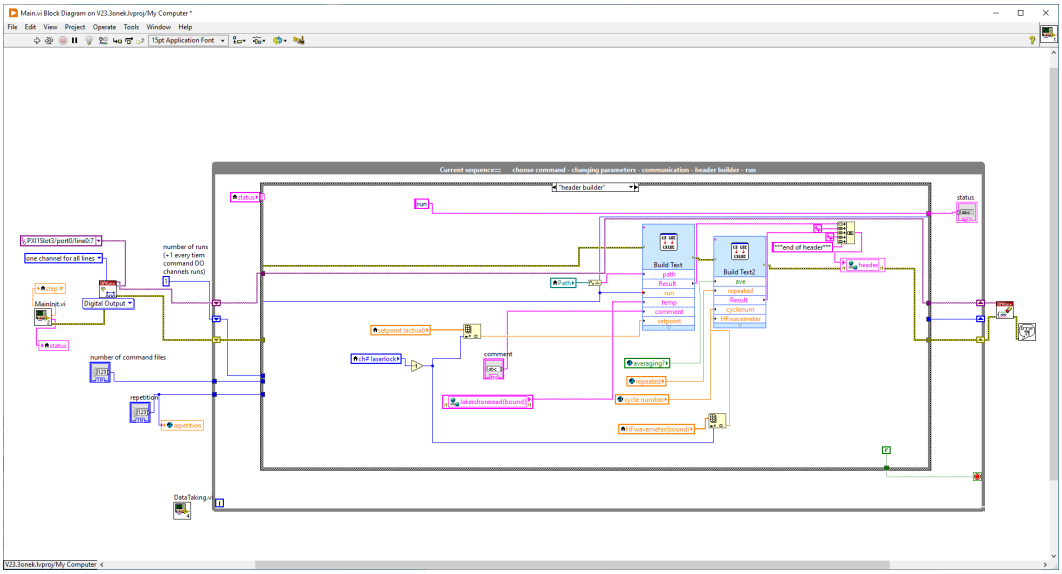

Figure A.5: Block diagram of the experiment control VI, "header builder" state of the state machine. This is the fourth state to run. Here we are gathering all the parameters and information and putting them into the header of the data file that will be saved for this run.

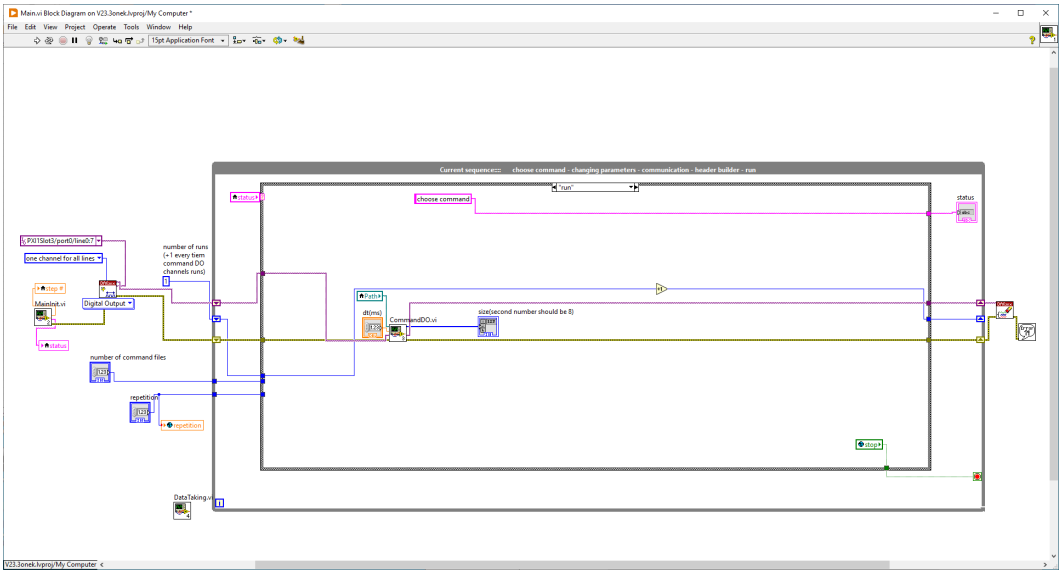

Figure A.6: Block diagram of the experiment control VI, "run" state of the state machine. This is the fifth state to run, and it mostly just runs the subVI commandDO.

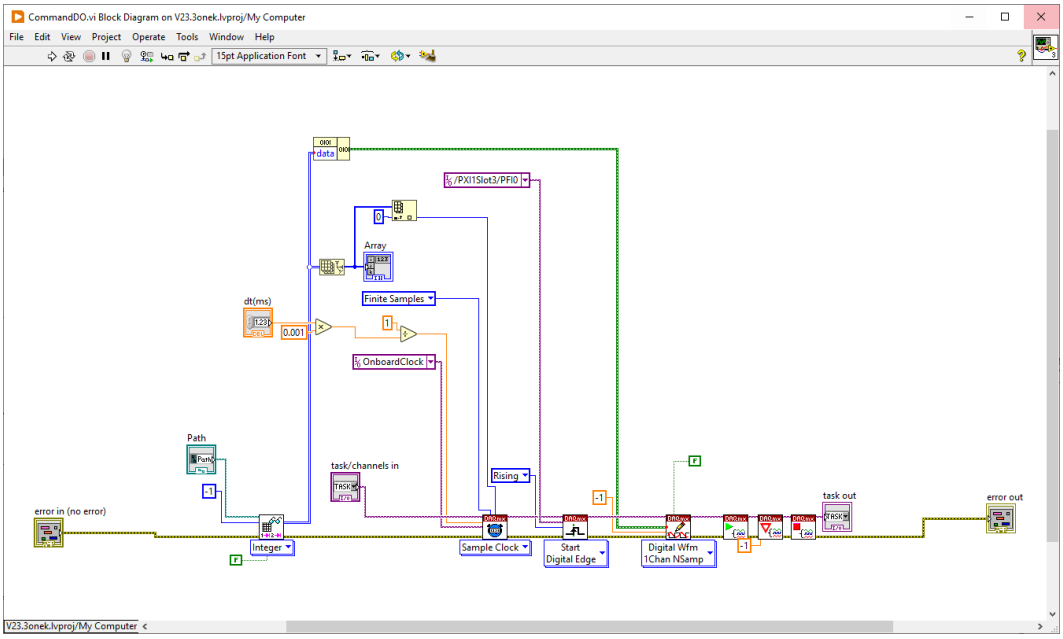

Figure A.7: Block diagram of the command digital output subVI commandDO.vi. It primes the channel to wait for a trigger pulse and once triggered sends out the digital signals according to the command file.

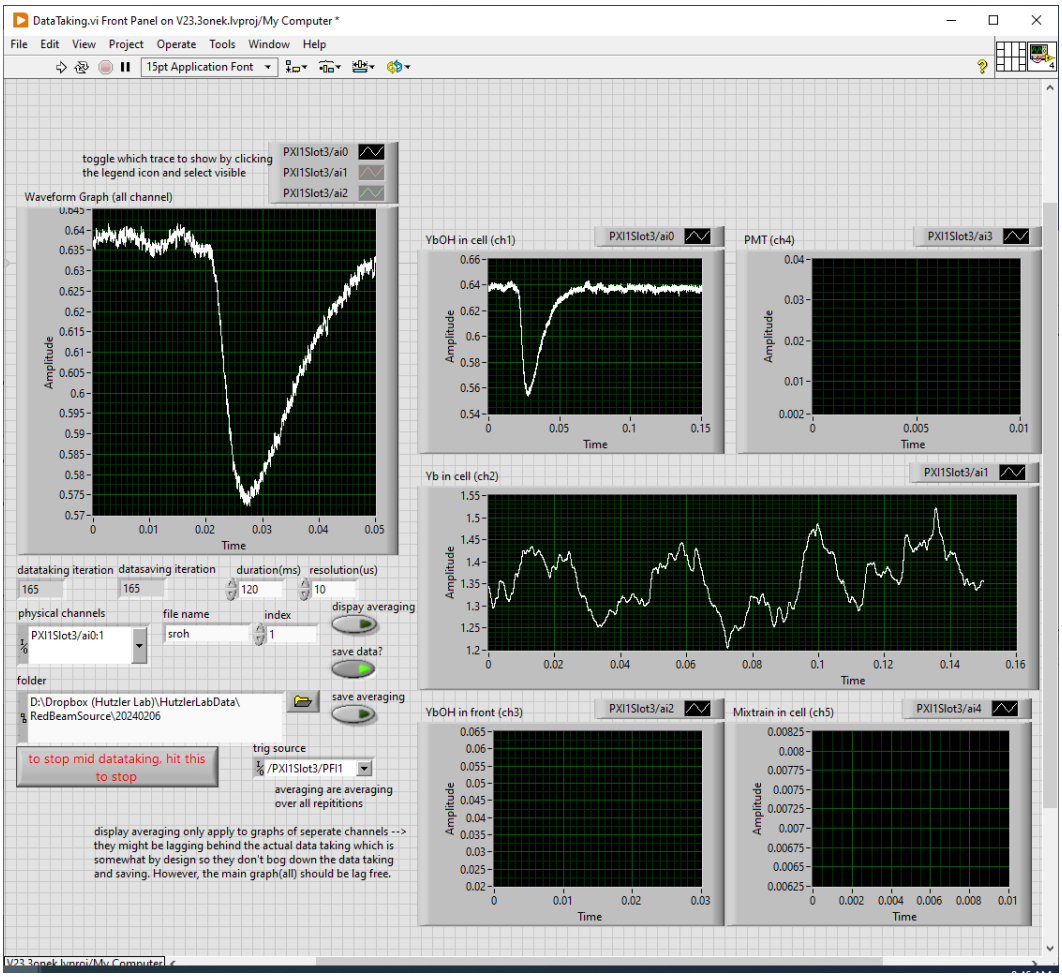

Figure A.8: The front panel of the data taking subVI. the data taking subVI will start to run as the experiment control main.vi start to run. The front panel is currently configured to display the waveform on each active channel, with options to display the average or save the average as data. The analog input channels will be immediately primed to wait for a trigger and once triggered start to take data.

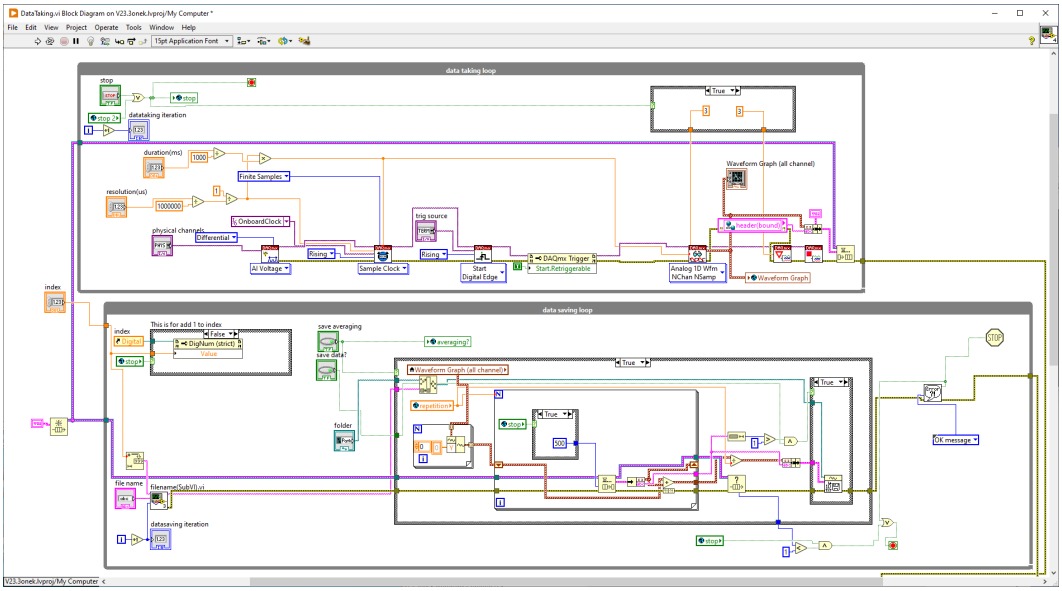

Figure A.9: Block diagram of the data taking subVI, top portion. The data taking loop on top primes the analog input channels to wait for a trigger and once triggered, starts to take data. The data is placed in a queue and retrieved sequentially by the data saving loop.

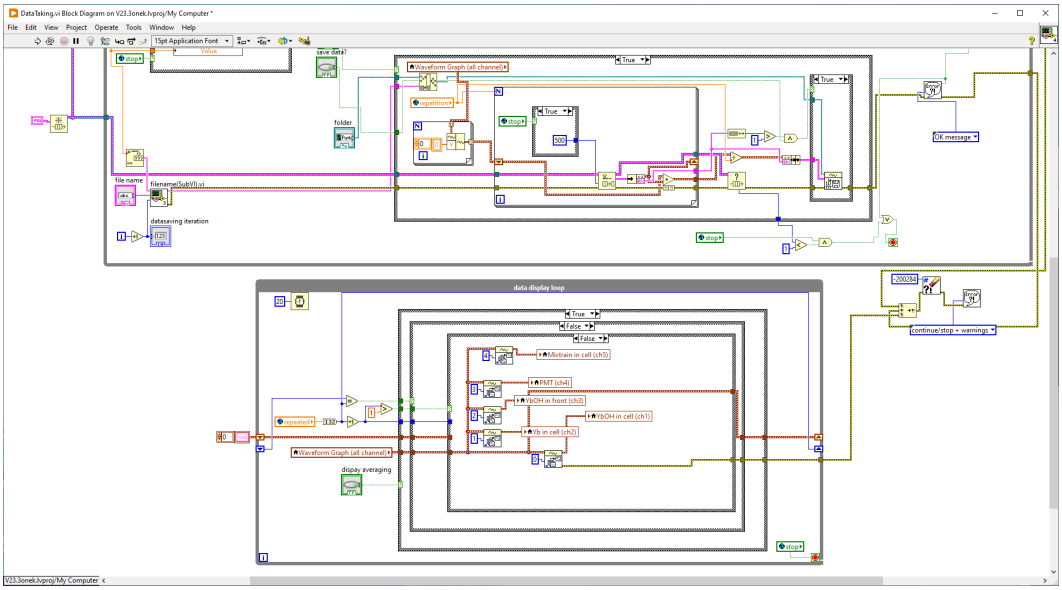

Figure A.10: Block diagram of the data taking subVI, bottom portion. The data display loop will grab the local variable from the data taking loop, and either directly display it or average over all the repeated runs under the same experiment parameter and then display the averaged waveform after all the repetitions are done.

A.2 Laser locks: cavity and wavemeter locks

One of the first laser-related projects I did here was to set up a transfer cavity lock for an ECDL, and throughout the years, I've built multiple versions of it, including one with homemade cavities and one for locking multiple lasers at the same time. The concept and various implementations of the transfer cavity lock are very well known. Basically, a free laser and a stabilized laser are sent into the same scanning Fabry-Perot, and then we can stabilize the free laser, by keeping the transmission peaks of the two lasers at a constant distance. We typically have the photodiode monitoring the cavity transmission sending the signal to a computer, which then curve fit the transmission peaks to calculate the distance between the free and stabilized peaks. Then a PID algorithm uses the distance as the error signal and calculates the control signal which is used to servo the free laser, typically as a voltage value on a piezoelectric drive. We generally followed the approach of Ref. [84].

At the time of the writing, only one laser is left that is still locked using the transfer cavity, as most of the lasers are now locked using the wavemeter and fiber switch combo, and I wouldn't be surprised if we soon even get that last laser off of transfer cavity lock. Hence I will focus on the wavemeter laser lock setup here. The concept of it is even simpler than that of the transfer cavity lock: we directly read the wavelength of lasers and use the difference between the read and the setpoint as the error signal for the PID servo.

The theoretical maximum performance of the wavemeter laser lock is much lower than that of the transfer cavity laser lock. A stock Fabery-Perot cavity from Thorlabs can have sub-MHz level resolution and can run at a repetition rate of 100 Hz, while the first wavemeter we use, HighFinesse WS7-30, only read down to 0.0001 cm^{-1} in wavenumber, which is around 3 MHz and can hardly do a repetition rate of 10 Hz depending on the number of channels used in the fiber switch. However, the benefits are obvious. The laser lock is absolute in wavelength instead of relative and it's easily expanded to multiple lasers with the fiber switch. Since we generally deal with Doppler-broadened lines which are around ~100 MHz wide, we only need to stabilize the lasers to a few MHz level, for which this solution is more than sufficient.

Our first wavemeter laser locking setup is somewhat tricky because the HighFinesse wavemeter is supposed to run with their proprietary fiber switch, which we couldn't get for a reasonable price. Hence, we set up our own Leoni eol 1x8 8-channel fiber switch. The software that comes with the HighFinesse will switch channels

automatically based on the parameters we put in the software. We read the currently active channel number using their provided Labview library, then tell the Leoni fiber switch to switch to the corresponding physical channel via serial communication. After that, we grab the wavemeter reading and assign it to the correct channel in our laser locking VI, to be used for PID servo. There are some complications as one would imagine, since the time sync won't be perfect, and sometimes channel skipping can occur. That is why we had to implement some extra features, like single channel operation, and typically have to operate with longer switch time than necessary. Still, we can operate at the limit of the fiber switch, 5 ms of switch time, if we want.

At the time of writing, we are setting up a new laser lock system with a new wavemeter, Bristol Instruments 871, and another Leoni eol 1x8 fiber switch. Because the new wavemeter can read much faster, up to 1kHz, and it doesn't expect to operate with any specific fiber switch, it is much easier to set up. All we need is to switch channels, wait for enough time to at least have two readings, and then grab the latest reading. Because of the fast read time, we can guarantee not grabbing the wavelength for the wrong channel, even if we operate at the limit of the switch, 5 ms per channel.

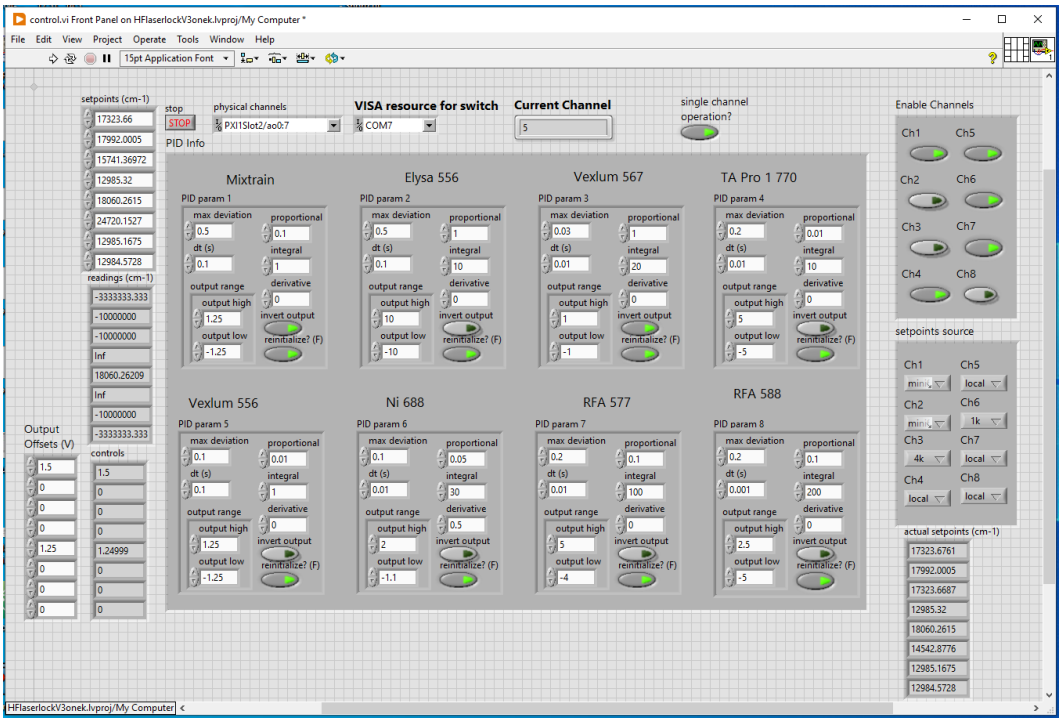

Figure A.11: The front panel of the wavemeter laser lock VI. It has to operate alongside the HighFinesse wavemeter software. It can be remotely operated by multiple experiments using Labview shared variables.

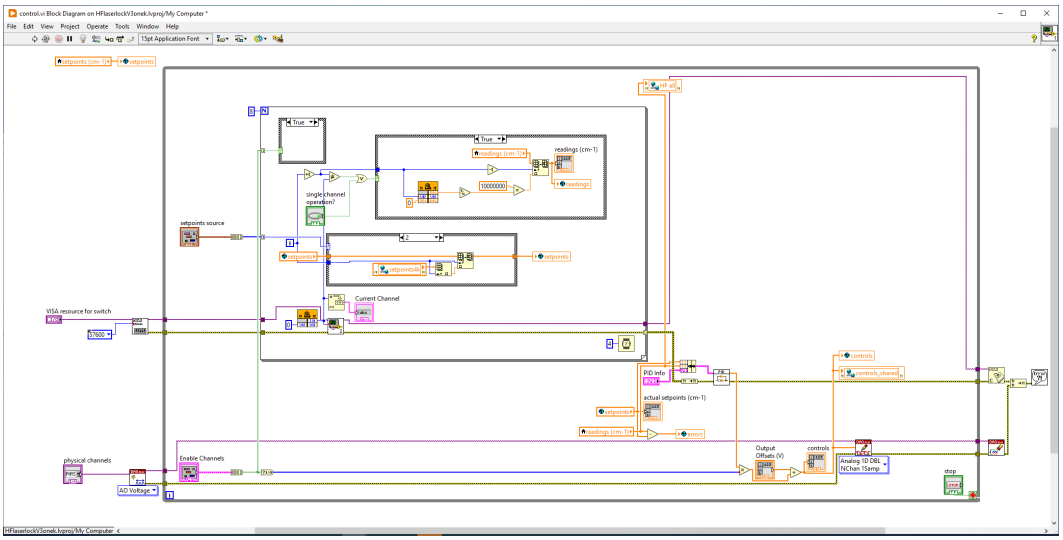

Figure A.12: The block diagram for the wavemeter laser lock VI. The code in the for loop reads the channel number from the HighFinesse software, switches the fiber switch channel accordingly, and then grabs the reading from the HighFinesse. The error signals (differences between readings and setpoints) are then sent into a PID subVI using Labview's built-in PID algorithm. Finally, the control signals are sent out via the analog output task.

A.3 ECDL details

Continuing from Chapter 3.4, I will share more details about the ECDL design and operation. We sent parts out to websites like 3D Hubs and Xometry to machine, especially for small and somewhat complicated parts like these ECDL parts. On average, it can cost less than 500 USD per ECDL when ordering just 3 sets of them, and they have very aggressive bulk pricing.

The original design adapted from the Kang-Kuen Ni lab prioritized air-tightness and preferred a grating angle of 45 degrees. It is supposed to be used as a set-up-and-forget long-term laser. See Figure A.13. We found its stability and air-tightness great for making it into a deep-cooled laser. However, for most use case scenarios, we found it too hard to work with, since we mostly use it for testing out new wavelengths and have to swap laser diodes and gratings quite frequently. The main annoyance with swapping diodes is the wiring, previously, the wiring goes through a hole in the middle of the outer housing, so every time you want to take out the inner housing, you have to disconnect all the wires. Due to how compact it is, very often we have to cut the wires and re-solder them.

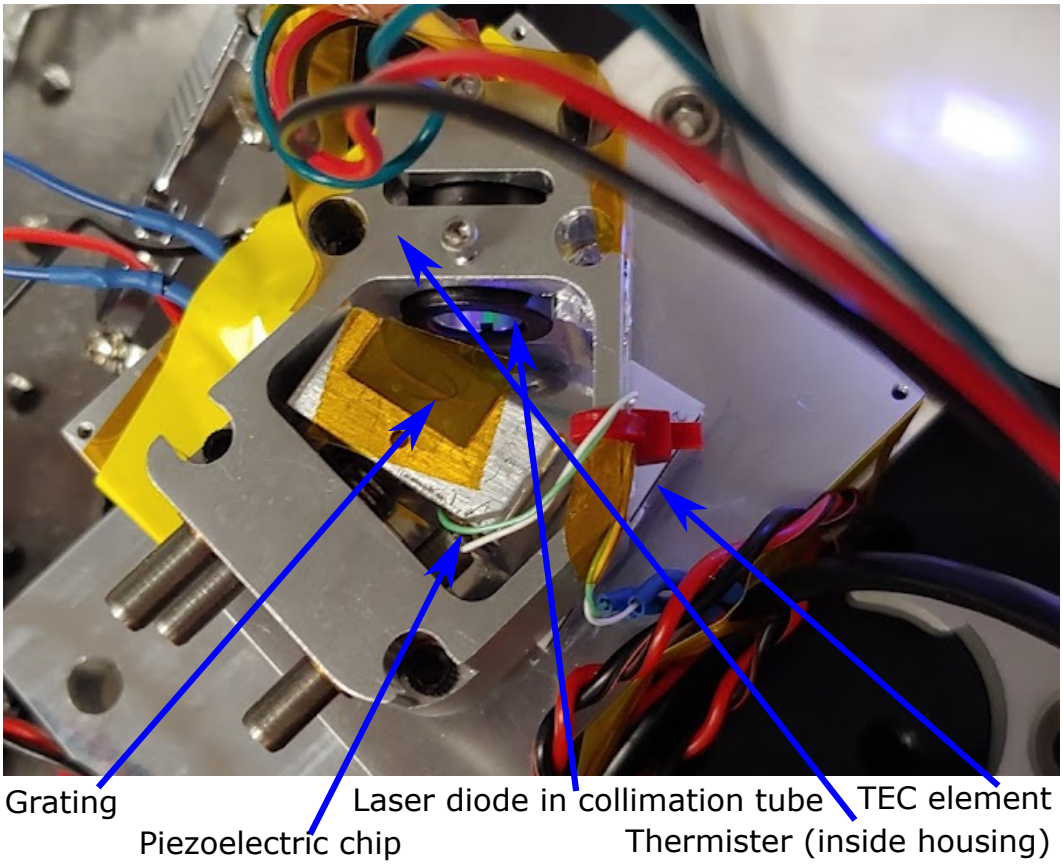

Figure A.13: Same figure as the one in Chapter 3.4. It is a photo taken when prototyping an older version of the design. You can see some rough machining to the right of the collimation tube, as a result of trying to increase the range of possible laser exit angle. Also, the grating is butting against the inner wall on the left, limiting possible grating angles.

The new design, as shown in Figure A.14 and A.15, significantly increases the possible range of grating angles by cutting out parts of the housing blocking the laser output, and by cutting out parts of the grating mounts that previously would butt against the housing, limiting its range of motion, as shown in Figure A.13. The outer housing has openings cut completely to the bottom. It allows for easy disassembly. We can just lift the outer housing and the lid straight up without having to worry about wires. The similar cutout at the back also allows for longer precision set screws for adjusting the grating mount more easily. The grating mount works like how most kinematic optics mounts, with two tension springs pulling it towards the housing and three precision set screws pushing the mount on three corners. The precision set screws use the bushings that are glued into the holes in the inner housing. At one corner of the grating mount, a special recess is drilled to fit the

piezoelectric disc and its wires.

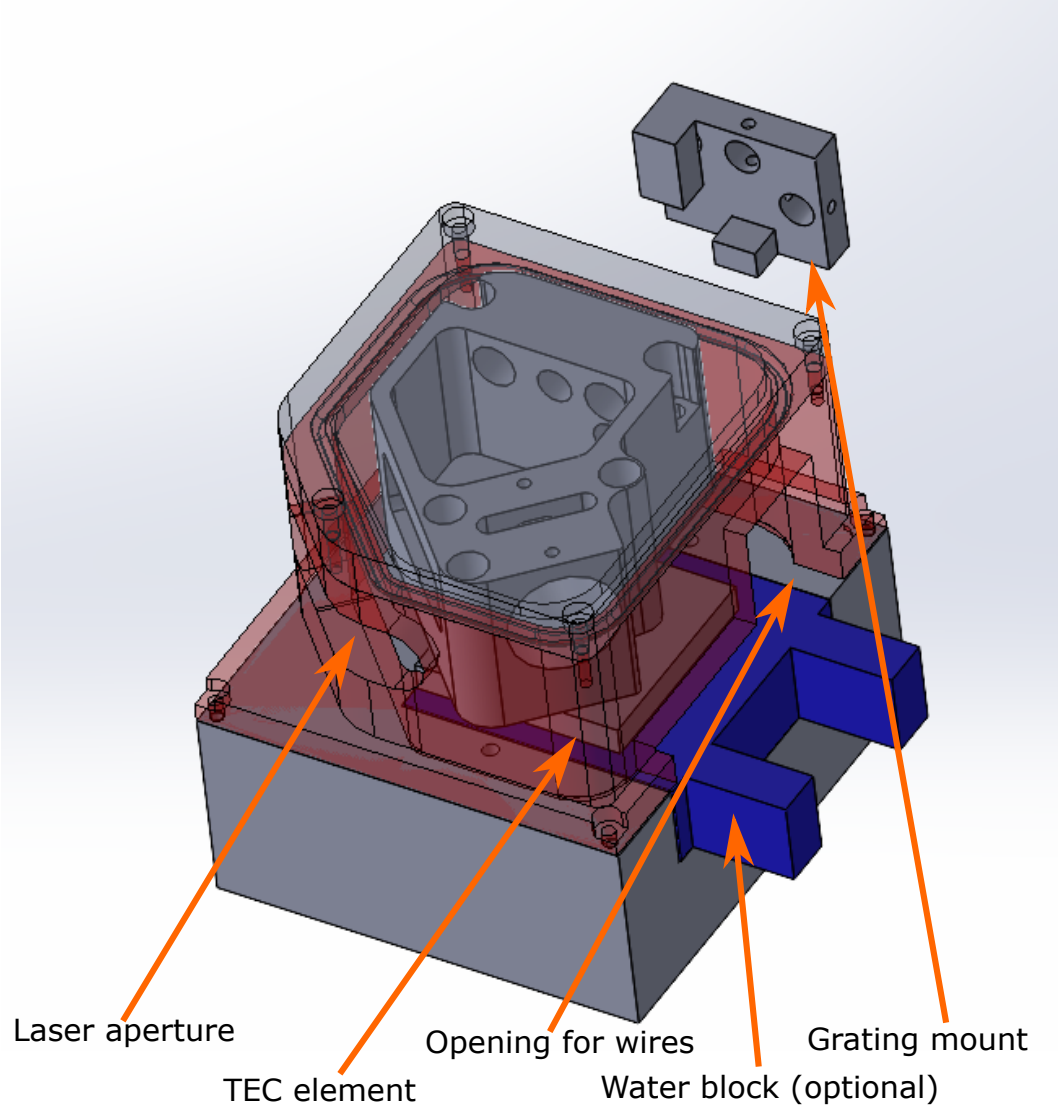

Figure A.14: Screenshot of the newest ECDL design. The grating mount is taken outside for clarity. This iteration of the design prioritizes the flexibility of the grating angle and ease of use. The water block is a standard 1 by 1 inch water block. The inner housing sitting on top of the TEC does not touch the lid or the outer housing, and it's screwed down to the base block with plastic screws for thermal isolation.

Chapter 3.4 mentioned how to improve feedback of the grating back to the diode by lowering the diode lasing threshold. Once that's done, the output light can be coupled into a fiber to be measured by a wavemeter. It is important to have a compensation mirror right in front of the ECDL aperture, as close as possible. With it, when coarse tuning of the grating is required and destroys the fiber coupling, you can quickly use the compensation mirror to manually get the fiber coupling back.

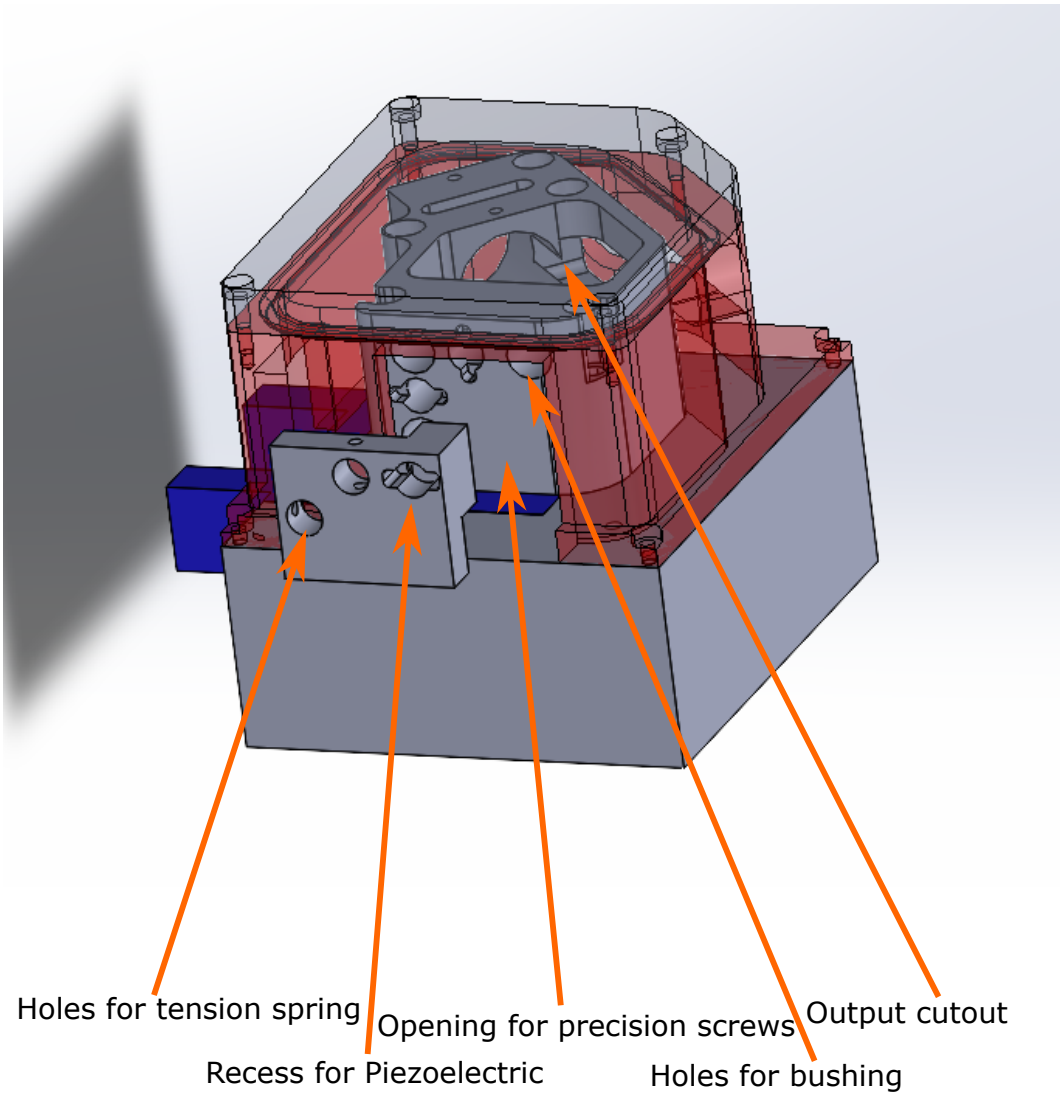

Figure A.15: Screenshot of the newest ECDL design. The grating mount is taken outside for clarity. The output cutout looks broken because the corner is cut for better optical access when the grating angle is small. The recess for Piezoelectric is designed such that the wires can better fit on the sides.

This compensation can also be done automatically with a folding mirror design. I've never tested it myself, since I find compensating by hand is easy and only rarely needed, while the folding mirror increases the complexity of the ECDL design and decreases the compactness, which is crucial for stability.

With the HighFinesse wavemeter, we not only see the wavelength of the laser but also see the interference patterns that can tell us if the laser is in single mode. Typically, when feedback is good and the lasing threshold is lowered significantly, the laser is always in single mode. However, some diodes, like the 399 nm ones from Nichia we

used as the Yb probe, can be hard to deal with. Even with good feedback, they can be in "fake" single mode, where they would have a small sideband. Fortunately, we can see it on the HighFinesse and just have to do more fine tuning with temperature and piezo to get rid of it.

In the general case, with good feedback, the horizontal grating angle can be coarsely tuned with the corresponding precision set screw to change the laser frequency by $\gtrsim$ 5 GHz. Remember that it can lower the fiber coupling efficiency due to the change in output angle, so do it in small steps, and compensate by adjusting the compensation mirror horizontally to keep the power reading on the wavemeter somewhat constant. Once the laser frequency is within $\sim$ 5 GHz away from the target frequency, it can be then fine tuned with piezo and temperature.

For me, the most ideal result coming out of these homemade ECDLs is a laser linewidth of about 5 MHz, passively stable within GHz and not mode hoping for hours, and it can be smoothly tuned in a range of GHz level, even without any current feedforward. We used a current controller, temperature controller, and piezo driver from Thorlabs, so there's no built-in current feedforward. It's something we can set up with electronics, or just do it by hand. Just by doing current feedforward by hand, we can extend the smooth tuning range to a 10 GHz level.

A.4 Zeeman-Sisyphus slowing

Zeeman-Sisyphus (ZS) slowing is a method of laser slowing paramagnetic atoms or molecules that is efficient in terms of scattered photons. It is a proven technique first tested with molecules by our collaborator Doyle group at Harvard [85]. As mentioned in Chapter 2, one of the difficulties of dealing with molecules, is that they tend to stop photon cycling by going into various kinds of dark states. We typically talk about photon budgets with regard to laser manipulation of molecules. By having repump lasers addressing these dark states, we can continue to cycle photons on that molecule, but eventually, it will decay into a dark state that is not addressed by any laser. We call the average number of photons a molecule will cycle, before decaying into a dark state, the photon budget. Clearly, it depends on the branching structure of the molecule and the number of repump lasers. For polyatomic molecules, even the species that are favorable to laser cooling will have limited photon budgets. For example, more than 10 repump lasers are needed for CaOH, in order to have a photon budget of $\sim 10^4$ [28].

Hence it is clearly desirable to have any laser manipulation of molecules to use as little amount of photons as possible. Traditional laser slowing of atoms or molecules is extremely inefficient since it relies on the momentum transfer of each photon, which is minuscule compared to the heavy molecules. Zeeman-Sisyphus slowing promises to lower the required number of photons for slowing molecules down to trappable speed by several orders of magnitudes. The reason is that ZS slowing removes kinetic energy from molecules by letting them continuously climb up magnetic potential hills, which can correspond to hundreds of photons worth of kinetic energy each hill. For example, in the case of CaOH, they used two sets of superconducting magnets with a maximum magnetic field of $\sim$ 2.8 T. With just 7 photons, they were able to slow down CaOH with an initial speed of $\sim$ 60 m/s by $\sim$ 35 m/s. The same 7 photons will only be able to slow down a CaOH by $\sim$ 0.1 m/s if only radiative force is used, like typical laser slowing [85].

The downside is that superconducting magnets are very bulky and require a lot of surrounding infrastructure. Many molecules could be lost due to beam divergence if the slowing region is too long. If we want to implement a slower of similar performance for YbOH, we might need more than 5 stages of magnets instead of the 2 used for CaOH, because YbOH is much heavier. Also, most likely we won't be

able to use a magnetic field that high for YbOH since there might be level crossing at magnetic fields above $\sim$ 1 T, which can lead to significant loss of population. Hence, we are trying to develop a ZS slower using permanent magnet arrays.

The project is led by Ashay Patel, with the goal of building a multi-stage ZS slower that is small and modular. Potentially, it can be used in combination with magnetic lens arrays to solve the molecule beam divergence problem. We have conducted some initial tests using permanent magnets in 5 stages with potassium atoms. Each stage is a simple configuration of a pair of rare-earth magnets vertically separated by a few mm, such that they create a maximum magnetic field of around $\sim$ 1 T. At the time of writing, the project is on hold due to a pivot towards trapping SrOH, and the 1 K CBGB source is prioritized to conduct SrOH bending mode spectroscopy.

A.5 Measured lines for ^{171,173}YbOH photon cycling

The following transitions were measured in spectroscopic studies performed for the photon cycling experiments presented in Chapter 4.

Appendix A: tables of measured transitions

See Table A.1 and A.2.

G''	F''	$J'(P)$	F'	Wavenumber/cm^{-1}
1	1	0.5+	1	16793.8375
1	0	0.5+	1	16793.8400
1	2	0.5+	1	16793.8433
1	1	0.5+	0	16793.8505
1	0	0.5+	0	16793.8530
1	2	0.5+	0	16793.8563
1	1	1.5+	1	16793.9340
1	0	1.5+	1	16793.9365
1	2	1.5+	1	16793.9398
1	1	1.5+	2	16793.9522
1	0	1.5+	2	16793.9547
1	2	1.5+	2	16793.9580
0	1	0.5+	1	16794.0698
0	1	0.5+	0	16794.0828
0	1	1.5+	1	16794.1663
0	1	1.5+	2	16794.1845

Table A.1: Measured transitions between $X''(100)N'' = 1$ and $A(000)$ in ^{171}YbOH. Uncertainties are estimated to be 0.0005 cm^{-1} due to wavemeter drift and uncertainty

G''	F''	$J'(P)$	F'	Wavenumber/cm^{-1}
2	1	0.5+	2	16794.0030
2	3	0.5+	2	16794.0100
2	3	0.5+	3	16794.0151
2	2	0.5+	2	16794.0312
2	2	0.5+	3	16794.0363
2	3	1.5+	4	16794.1098
2	1	1.5+	2	16794.1183
2	2	1.5+	3	16794.1353
2	2	1.5+	1	16794.1623
3	2	0.5+	2	16794.1891
3	2	0.5+	3	16794.1942
3	4	0.5+	3	16794.2068
3	3	0.5+	2	16794.2230
3	3	0.5+	3	16794.2281
3	4	1.5+	4	16794.3010
3	2	1.5+	2	16794.3043
3	4	1.5+	3	16794.3061
3	2	1.5+	1	16794.3204
3	3	1.5+	3	16794.3274
3	3	1.5+	2	16794.3383

Table A.2: Measured transitions between $X''(100)N'' = 1$ and $A(000)$ in ^{173}YbOH. Uncertainties are estimated to be 0.0005 cm^{-1} due to wavemeter drift and uncertainty

Appendix B: tables of Calculated $X(100)$ energy levels

From the measured transitions, and energy levels from previous spectroscopy studies [18], we calculated energy levels relevant to the photon cycling, as shown in Table A.3 and A.4.

N	G	F	Wavenumber/cm^{-1}
1	0	1	529.2047
1	1	2	529.4370
1	1	0	529.4345
1	1	1	529.4312

Table A.3: Energies of levels in ^{171}YbOH $X(100)$ determined by this work. Uncertainties are estimated to be 0.0005 cm^{-1} due to wavemeter drift and uncertainty, and excited state energy uncertainty.

N	G	F	Wavenumber/cm^{-1}
1	2	1	530.146
1	2	3	530.139
1	2	2	530.118
1	3	2	529.960
1	3	4	529.947
1	3	3	529.926

Table A.4: Energies of levels in ^{173}YbOH $X(100)$ determined by this work. Uncertainties are estimated to be 0.001 cm^{-1} due to wavemeter drift and uncertainty, and excited state energy uncertainty.

A.6 Fluorescence model for laser beam smaller than molecule beam

Continuing from Chapter 3.3. As mentioned, I developed a model for characterizing the fluorescence lineshape for the case of a laser beam smaller than the molecule beam, and the transition has dark states, i.e. the branching ratio is smaller than 0.99.

The study was conducted by doing a Monte Carlo simulation of uniform 3-D arrays of molecules going through a perpendicular laser beam with intensity in Gaussian distribution, at a constant forward velocity and normal distribution of velocity in the direction of the laser, which causes Doppler detuning. As the molecules go through the laser beam, the absorption rate and stimulated emission rate are determined by the spontaneous decay rate, detuning, and laser intensity. Every time step, the molecule position is updated on a discrete grid of 2-D space. A molecule is initially in the ground state, as it goes into the laser beam, every time step, a dice is rolled to determine if it is excited based on the absorption rate. When in the excited state,

at every time step, a dice is rolled to determine if it spontaneously decayed. If so, a fluorescence photon is counted, and another dice roll determines if it goes into the dark state based on the branching ratio. If not spontaneously decayed, another dice roll determines the stimulated emission rate.

The simulation was able to capture all the expected behavior, such as Rabi oscillations when the branching ratio is 1 and Doppler broadening. Also, as shown in Figure A.16, the line shapes are as expected. What I then tried to model, is the lineshape of Figure A.16 (C). My attempts were trying to integrate the typical Lorentian lineshape over the effective laser beam shape, where the dark state is taken into account, as shown in Figure A.17. As the molecules travel across the laser beam, most of them will decay into dark states long before exiting the laser beam, if the laser power is above saturation. Hence, only a vertical strip of the laser cross section actually contributes to the fluorescence. The resulting lineshape is:

$$\int \frac{S_0(r)}{1+S_0(r)} \frac{A/2}{1+(2\Delta/A)^2(1+S_0(r))} e^{ax^2} dx \tag{A.1}$$

A is the Einstein A coefficient, Δ is the detuning, $S_0(r)$ is the saturation parameter depending on the laser intensity distribution, and a is the extra free parameter introduced for this model to account for the proportion of the laser area contributing to the fluorescence.

Using this lineshape formula derived from my model, I compared it to the simulation. The result is shown in Figure A.18. By introducing one extra free parameter, the model worked great, much better than the normal Lorentzian, and the fitted free parameter a stays constant as the maximum laser intensity changes in different simulations.

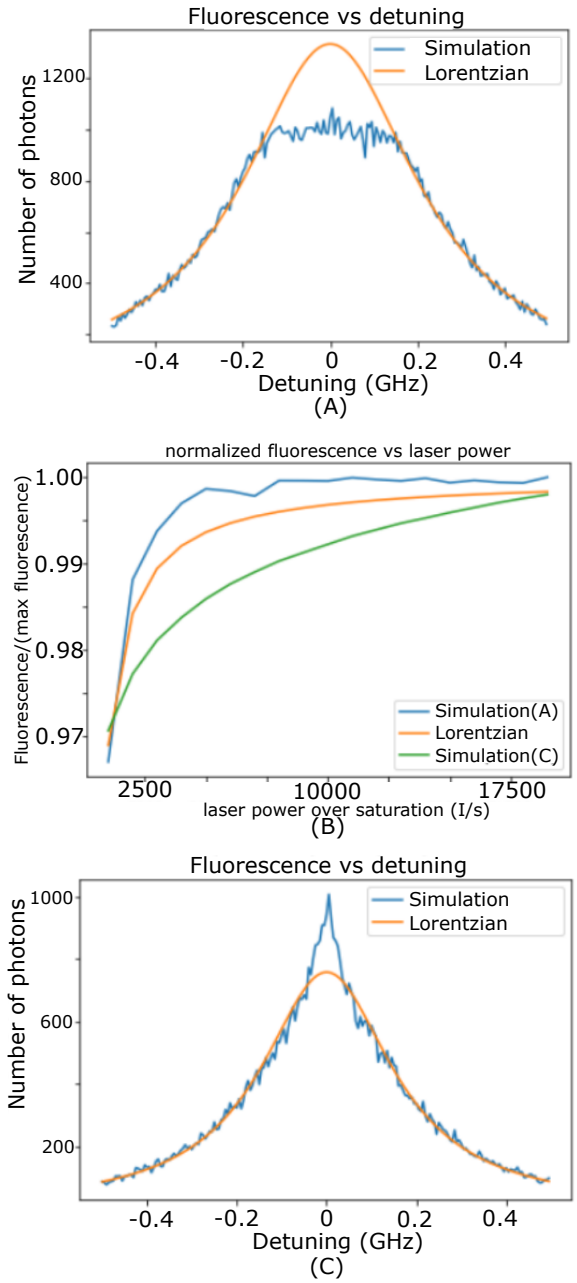

Figure A.16: Figures for the study of saturation caused by dark state. (A) Simulated lineshape of saturation caused by dark state in blue. The molecule beam is much smaller than the laser beam in the simulation. Lorentzian lineshape of normal saturation under similar conditions in orange. (B) Normalized fluorescence amplitude vs laser power in saturation parameter. Blue is the simulation in (A), Orange is from the typical Lorentzian calculation, and Green is the simulation in (C). (C) Similar to (A), except the blue line is from a simulation where the molecule beam is much wider than the laser beam.

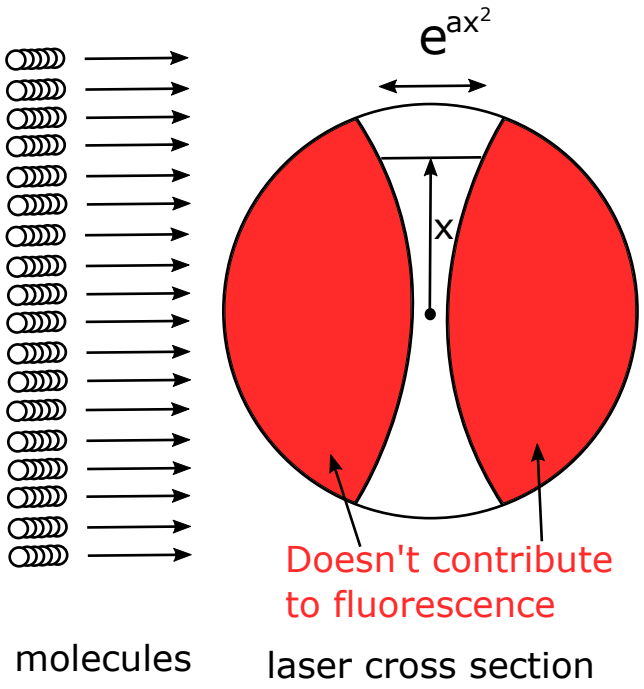

Figure A.17: The model I came up with to describe the fluorescence lineshape for the scenarios where the laser beam is smaller than the molecule beam, which also has a dark state for the transition. It takes into account the fact that only a part of the laser beam contributes to the fluorescence because of the dark states.

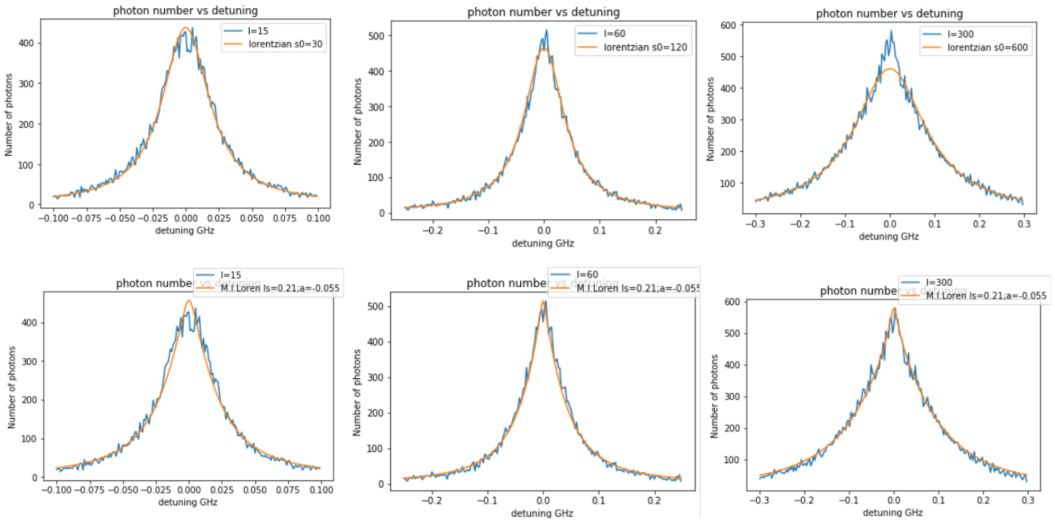

Figure A.18: The top plots are the typical Lorentzian lineshape fitted to the simulation results, and the bottom plots are my integrated model fitted to the same results, getting the same number for the free parameter a. The different simulation results have different maximum laser intensities.

A.7 Diatomic molecule FCF method and data list

I undertook a project to calculate and compile the laser coolability data on diatomic molecules using spectroscopic databases. Nick did most of the data collection work by scraping data from the NIST Webbook, and we also looked for data from newer sources like spectroscopy papers for other molecules. In the end, we have collected data on 1487 electronic states, though some of them don't have sufficient information that we can use for calculating FCF, which is Franck-Condon factors, effectively vibrational branching ratios. As mentioned in Chapter 2, the main challenge of laser cooling molecules is their vibrational branching ratio leading to large numbers of dark states. In most cases, a molecule is only technically laser-coolable, when the vibration branching ratio is highly concentrated on returning the molecule to its original ground state, with only a few dark states that receive some meaningful but small branching.

Among the parameters for each molecule's electronic state, we use ω_e, r_e, and $\omega_e\chi_e$, to calculate the vibrational potential curves. From that, we can use time-independent Schrodinger's equation to calculate the 1-dimensional wavefunctions of vibrational states of the molecules, because of the Born-Oppenheimer approximation and the fact that electronic transitions happen much faster than nuclear motions.

One of the easiest ways to derive Franck Condon factors is to use the harmonic oscillator approximation[86]. Using ω_e and r_e, which are available for most of the electronic states of the molecules, we can calculate the vibrational wavefunctions for each state in the harmonic approximation. The only other parameter needed is μ, the reduced mass of the molecules.

We express the wavefunctions from the analytical solution of the quantum harmonic oscillator. To calculate the FCFs, we simply square the overlap integral.

$$F_{nn'} = \left| \int_0^\infty \psi_n^* \psi_{n'} \, dr \right|^2 \tag{A.2}$$

$$\psi_n(r) = \frac{1}{2^n n!} \left(\frac{\mu\omega_e}{\pi\hbar} \right)^{1/4} e^{-\frac{\mu\omega_e (r-r_e)^2}{2\hbar}} H_n\left(\sqrt{\frac{\mu\omega_e}{\hbar}} r \right) \tag{A.3}$$

H_n is the Hermite polynomials. The results from these simple calculations are quite good for transitions with $F_{00} > 95\%$, the FCF of the vibrational ground-to-ground transition. For highly diagonal molecules, when compared to measured data, these estimates are often accurate to within measurement uncertainties (when available).

For better results, we use a Morse potential to calculate the vibrational wavefunctions for states where the constant $\omega_e\chi_e$ is available and positive. Compared to the

harmonic oscillator approximation, the Morse potential provides a better representation of the actual potential curve in terms of the disassociation energy, and the fact that the equilibrium distance moves outwards in higher vibrational states. The form of the Morse potential we used is

$$U(r) = -D_e \left(1 - e^{-a(r-re)}\right)^2 \tag{A.4}$$

We can estimate the parameters from the vibrational constants using the formula[86]:

$$D_e = \frac{\omega_e^2 hc}{4\omega_e \chi_e} \tag{A.5}$$

$$a = \sqrt{\frac{8\omega_e \chi_e \mu}{h}} \tag{A.6}$$

Note that these relations require $\omega_e \chi_e > 0$, which is not the case for all molecules, such as the $A^1\Sigma^+$ states of alkali hydrides [87, 88]. Unlike the harmonic oscillator case, we did not use the analytical solution of Morse potential for calculating FCF, even though it is one of the few potentials with analytical solutions. The reason is that the analytical form is more cumbersome than a simple method to numerically calculate the eigenvectors.

Instead, we use a numerical calculation based on a discrete *sinc* function basis. The i-th basis wavefunction is defined as:

$$\psi_i(r) = \frac{sinc[\pi(r - r_i)/\Delta r]}{\sqrt{\Delta r}} \tag{A.7}$$

with Δr being the step size. From it, the discretized Hamiltonian takes the form of:

$$H = T + U(r) \tag{A.8}$$

$$T_{ij} = \begin{cases} \frac{\hbar^2(-1)^{i-j}}{(i-j)^2 \mu \Delta r^2} & i \neq j \\ \frac{\pi^2 \hbar^2 (-1)^{i-j}}{6\mu \Delta r^2} & i = j \end{cases} \tag{A.9}$$

and $U(r)$ is the Morse potential which is already diagonal in the position basis. This algorithm converges quickly. We use $\Delta r = 0.1$ nm, which yields convergent results for all molecules and is reasonably fast.

We use a figure of merit defined as $FOM = log_{10}(1 - f_{00} - f_{01} - f_{02} - f_{03})$, which translates approximately to meaning that the transition can cycle 10^{FOM} photons before leaking into dark vibrational states when using 3 vibrational repumps. Setting $FOM > 4$ as standard for selecting transitions as photon cycling candidates. Note that this ignores other potentially important effects, such as decay to other electronic states, hyperfine states, spin-orbit states, etc. to be discussed later on. We found 317 candidates from the Harmonic Oscillator calculation and 187 from the Morse potential calculation.

In general, the Morse potential calculation gives a larger FOM and thus should generate more candidates. For example, the AlO $B^2\Sigma - X^2\Sigma$ transition has a FOM of 2.78 in harmonic, and 4.69 in the Morse potential, as shown in table A.5. Unfortunately, more than half of the states in the NIST WebBook data don't have a reported $\omega_e\chi_e > 0$.

Methods	F00	F01	F02	F03
Harmonic	0.7170	0.2233	0.049	0.0089
Morse	0.7306	0.2369	0.0309	0.0016

Table A.5: For AlO $B^2\Sigma - X^2\Sigma$ transition, the calculations from Morse potential give more diagonal results.

Harmonic oscillator calculation gives very good results for lower vibrational states in highly diagonal molecules. As an example A.6 is a table showing FCFs for BaH $A^2\Pi - A^2\Sigma$ transition resulting from the harmonic oscillator approximation, Morse potential, and RKR potential. As you can see, they are very close, even though the Harmonic oscillator approximation only uses two vibrational constants.

methods	F00	F01	F02
Harmonic	0.954	0.042	0.003
Morse	0.953	0.045	0.002
RKR	0.951	0.048	0.002

Table A.6: a comparison of FCFs from different methods for BaH $A^2\Pi - A^2\Sigma$ transition. The RKR results are from [1].

Since there are analytical solutions, we can expand the FCF solution with respect to $\alpha = \frac{r_{e2}}{r_{e1}}$ the ratio of internuclear distances, and $\beta = \frac{\omega_{e2}}{\omega_{e1}}$ the ratio of harmonic constants to get some rough idea about dependencies. For vibrational 0-0 transitions,

we have:

$$f_{00} = 1 + A(\alpha - 1)^2 + B(\beta - 1)^2 + O((\beta - 1)(\alpha - 1)^2) + O((\beta - 1)^3) \tag{A.10}$$

$$A = -c\pi \left(\frac{r_{e1}}{r_c^2}\right)^2, B = 1/8 \tag{A.11}$$

where $r_c = \sqrt{\frac{\hbar}{\mu\omega_{e1}}}$ is the characteristic length of the harmonic oscillator. The first order terms must be zero by a symmetry argument. In second order terms, the numerical value of A is given by $0.015(r_{e1}/\text{Å})^2(\mu/amu)(\omega_{e1}/cm^{-1})$. Thus with typical values of $r_{e1} = 1$, $\mu = 5$, and $\omega_{e1} = 500$, we find $|A| \gg |B|$, that is, the internuclear distance term dominates for most molecules. For 0-1, the FCF can be expanded to:

$$f_{01} = C(\alpha - 1) + D(\alpha - 1)(\beta - 1) + O((\beta - 1)^2(\alpha - 1)) + O((\beta - 1)(\alpha - 1)^2) \tag{A.12}$$

$$C = \sqrt{c\pi}\frac{r_{e1}}{r_c^2}, D = C/2 \tag{A.13}$$

As expected, there's no leading 1 term, and there is a first order term for the ratio of internuclear distances. All these features are consistent with calculations done with perturbation theory, where we fix one of the ratios and treat the other ratio as perturbations.

For less diagonal transitions (FCF of vibrational ground to ground smaller than 95%), The correction from Morse potential becomes more significant, on the order of 1%. For example, table A.7 shows the difference between the two methods as well as the measured data and calculations using RKR potential.

methods	F00	F01	F02	F03
Harmonic	0.9135	0.0805	0.0056	0.003
Morse	0.9208	0.0735	0.0053	0.003
RKR	0.9200	0.0740	0.0050	0
measured	0.920	0.074	0.005	0

Table A.7: Comparison of FCFs resulting from different methods for CN $B^2\Sigma - X^1\Sigma$ transition.

As an example of how we can further study a laser-coolable molecule, here's a case study on LuF. After identifying a transition with good vibrational properties, and

	F00			F01			F02		
	harm.	Morse	ab ini.	harm.	morse	ab ini.	harm.	morse	ab ini.
AgH									
X-A	0.945	0.903	0.995	0.046	0.090	0.001	0.008	0.006	0.016
CuO									
X-E	0.998	0.998	0.998	0.000	0.000	0.000	0.002	0.002	0.002
BeCl									
X-A	0.950	0.949	0.947	0.048	0.051	0.052	0.002	0.000	0.000
BiH									
X-B	0.984	0.990	0.907	0.016	0.009	0.007	0.000	0.000	0.000

Table A.8: More comparisons. Harm. is short for harmonic and ab ini. is short for ab initio. AgH [2], CuO[3], BeCl[4], BiH[5].

high FOM, we can then look into the following properties to determine whether it is amenable for fast photon cycling or not: 1. Is there an intermediate electronic state with a significant branching ratio? 2. What is the radiative lifetime of the transition? 3. Is there a rotational transition we can use that does not decay into dark rotational states? 4. What is the hyperfine splitting of the ground state, and is it small enough to cover with a single laser or EOM? These are not everything we need to know but are the important ones and are relatively easy to find.

Here, we present a quick case study for LuF $A^1\Sigma - X^1\Sigma$, at a wavelength of 618.6 nm. This transition has no intermediate state and has a small radiative lifetime of about 20 ns. From Morse potential calculation, the FCF of the ground vibrational state to the first 4 states are 0.9665, 0.0330, 0.0004, and 0, so only two repumps are needed for photon cycling above 10000 photons. The rotational transition of $J'' = 1 \leftrightarrow J' = 0$ is closed because there's no angular momentum other than rotation, see the level diagram in Figure A.19. The hyperfine splitting is dominated by the quadrupole interaction of the Lu nucleus, which gives rise to three hyperfine levels for the $J'' = 1$ ground states with splittings of about 100 MHz.

I made periodic tables for diatomic molecules with H, D, F, and O as one of the atoms. The sum of the first two numbers of the FCF, F00+F01, is indicated by how red it is.

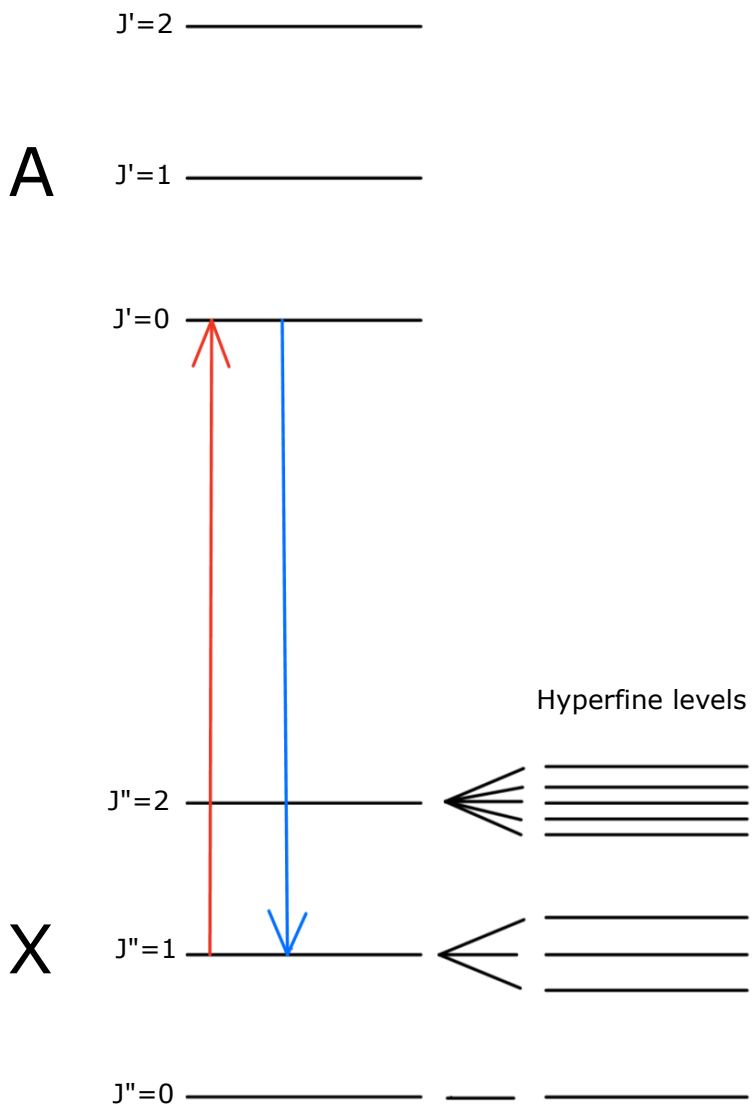

Figure A.19: Level diagram of LuF $A^1\Sigma - X^1\Sigma$ transition, with hyperfine levels shown for ground state (spacings not to scale). The arrows show a closed rotational transition that can be potentially used for photon cycling.

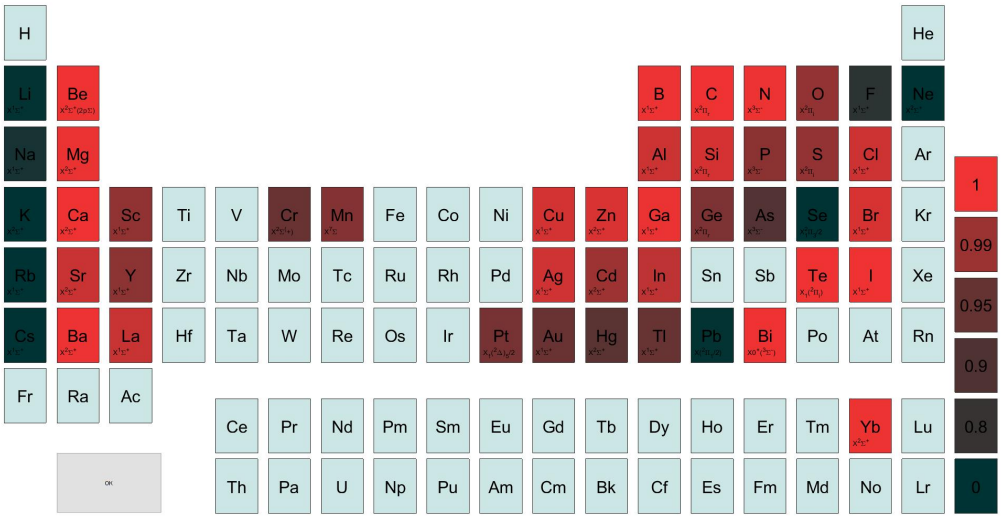

Figure A.20: Diatomic molecules with H as one of the atoms. Color in redness for F00+F01 in log scale. Only transitions from X to non-X are used. Theory is labeled with (th). Ions are also included, but not differentiated.

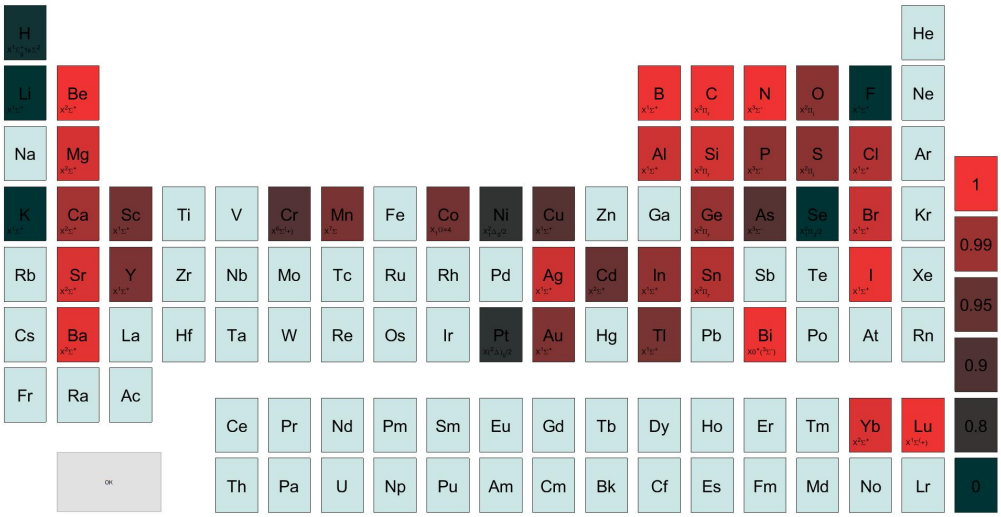

Figure A.21: Diatomic molecules with D as one of the atoms. Color in redness for F00+F01 in log scale. Only transitions from X to non-X are used. Theory is labeled with (th). Ions are also included, but not differentiated.

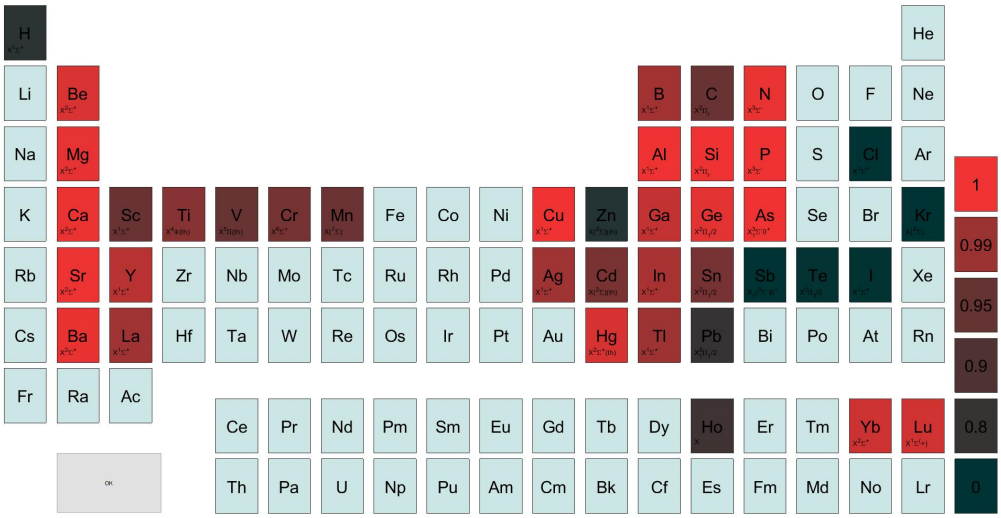

Figure A.22: Diatomic molecules with F as one of the atoms. Color in redness for F00+F01 in log scale. Only transitions from X to non-X are used. Theory is labeled with (th). Ions are also included, but not differentiated.

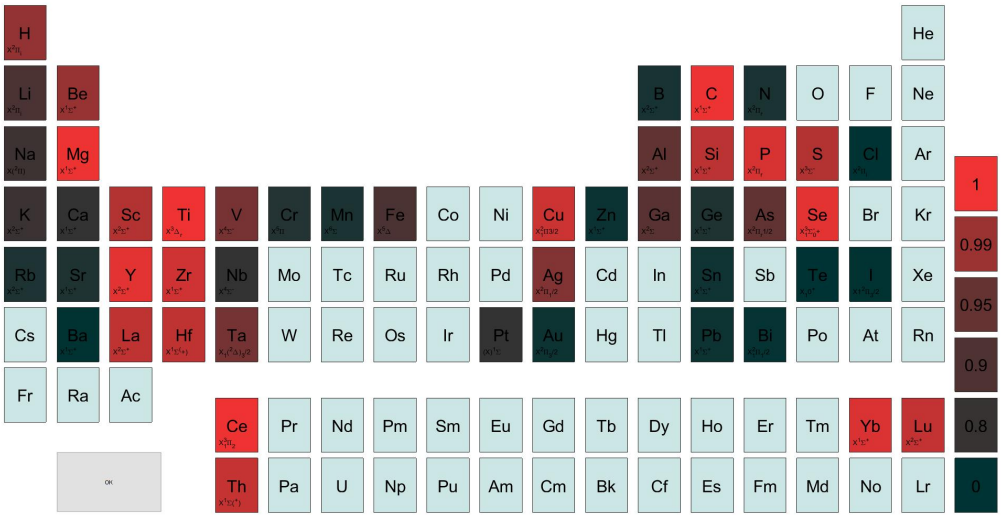

Figure A.23: Diatomic molecules with O as one of the atoms. Color in redness for F00+F01 in log scale. Only transitions from X to non-X are used. Theory is labeled with (th). Ions are also included, but not differentiated.